

Measurement of the CKM angle γ using $B_s^0 \rightarrow D_s K \pi\pi$ decays

P. d'Argent¹, E. Gersabeck², M. Kecke¹, M. Schiller³

¹*Physikalisches Institut, Ruprecht-Karls-Universität Heidelberg, Heidelberg, Germany*

²*School of Physics and Astronomy, University of Manchester, Manchester, United Kingdom*

³*School of Physics and Astronomy, University of Glasgow, Glasgow, United Kingdom*

Abstract

We present the first measurement of the weak phase $\gamma - 2\beta_s$ obtained from a time-dependent (amplitude) analysis of $B_s^0 \rightarrow D_s K \pi\pi$ decays using proton-proton collision data corresponding to an integrated luminosity of 7 fb^{-1} recorded by the LHCb detector.

Change-log

- Version 1.0: First note draft circulated to the WG
- Version 2.0: Implemented first round of comments from Mark, Alessandro, Agnieszka
 - Changed D^0 bkg vetoes (Sec. 4.2.2)
 - Revisited some systematics
 - * Use uncertainty from fake rate instead of fixing misID yield to 0 or twice the value (Sec. 12.2)
 - * Use GLASS model instead of RBW as alternative to LASS model for $K\pi$ S-wave (Sec. 12.9)
 - * Instead of assuming pure phase space, recalculate running width of three-body resonances taking only the dominant $K\pi\pi$ decay mode into account (Sec. 12.9)
 - * Calculate RMS of lineshape variations instead of summing them up in quadrature (Sec. 12.9)
 - * Bug fix in evaluation of fixed lineshape parameters (mass, width, form-factor) systematic (Sec. 12.9)
 - Added tables with alternative amplitude models (Sec. 12.10)
 - Added comparison plots of 16 vs 17 data (Sec. M)
- Version 3.0:
 - Changed D^0 bkg vetoes back to the ones from v1.0 to account for additional Kaon misID (Fig. 4.3)
 - Updated analysis with new MC samples (Sec. 4.3)
 - Studied time resolution separately for 16 and 17 data (Sec. 6.2)
 - Changed phasespace acceptance method from BDT to MC integration (Sec. 7.3)
 - Updated analysis with latest OS Tagger tuning (Sec. 8.1)
- Version 3.1: Minor changes, approved by Mark and Alessandro
- Version 3.2: Updated fit validation of phasespace-integrated and full fit using the same data set (Sec. 2.4)
- Version 4.0: Implemented first round of comments from Marta and Rafael
 - Added a small section summarizing the main analysis steps (Sec. 3)
 - Small improvements to the formalism (Sec. 2) and additional information on used lineshapes (Sec. A)
 - Additional information on fit stability and interference fractions (Sec. K)
 - Added additional systematic studies for the phase-space acceptance (Sec. 12.8)
 - Added rough estimate of sensitivity to physical observables from phase-space integrated fit (Sec. 10.2)
 - Added comparison of phase-space integrated and full time-dependent amplitude fit (Sec. 13)

- Version 4.1: Implemented second round of comments from Marta and Rafael
 - Added systematics for fit fractions (Table 11.3)
 - Added additional information to tagging calibration (Sec. 8.1) and detection asymmetry sections (Sec. 9.2)
- Version 5.0: Unblinded results
- Version 6.0:
 - Added studies of the decay-time bias (Sec. 6.3) and related systematic (Sec. 12.4)
 - Added stat. and syst. correlation matrix for CP coefficients (Tables 10.3,10.4)
 - New closure test for Δm_s (Sec. 12.1)
 - Added systematic study for ignoring correlation between reconstructed mass and decay-time (Sec. 12.2)
 - The assumption that time- and phasespace acceptance factorize is tested (Sec. 12.8)

Contents

1	Introduction	1
2	Formalism	2
2.1	Decay rates and CP -observables	2
2.2	Amplitude model	4
2.2.1	Form Factors and Resonance Lineshapes	4
2.2.2	Spin Densities	5
2.3	Fit implementation	7
2.4	Validation	8
3	Analysis strategy	11
4	Data samples and event selection	11
4.1	Stripping and Trigger selection	11
4.2	Offline selection	11
4.2.1	Phase space region	12
4.2.2	Physics background vetoes	13
4.2.3	Training of multivariate classifier	16
4.2.4	Final selection	17
4.3	Simulation	22
5	Yields determination	23
5.1	Signal model	23
5.2	Background models	24
5.3	Results	26
6	Decay-time Resolution	27
6.1	Calibration for Run-I data	28
6.2	Calibration for Run-II data	29
6.3	Decay-time bias	32
7	Acceptance	34
7.1	MC corrections	34
7.1.1	Truth matching of simulated candidates	34
7.1.2	Correction of data-simulation differences	34
7.2	Decay-time acceptance	35
7.3	Phase space acceptance	39
8	Flavour Tagging	41
8.1	OS tagger combination	42
8.2	Tagging performance	44
9	Production and Detection Asymmetries	45
9.1	B_s Production Asymmetry	45
9.2	$K^-\pi^+$ Detection Asymmetry	46

10 Decay-time fit	49
10.1 Fit to $B_s^0 \rightarrow D_s\pi\pi\pi$ data	49
10.2 Fit to $B_s^0 \rightarrow D_sK\pi\pi$ data	49
11 Time-dependent amplitude fit	53
11.1 Signal Model Construction	53
11.2 Results	57
12 Systematic uncertainties	60
12.1 Fit bias	60
12.2 Background subtraction	60
12.3 Decay-time acceptance	61
12.4 Decay-time resolution and tagging	62
12.5 Production, detection asymmetries and mixing frequency	63
12.6 Multiple candidates	63
12.7 Length and momentum scales	63
12.8 Phase space acceptance	64
12.9 Resonance description	64
12.10 Alternative amplitude models	65
13 Summary	72
A Parametrization of Amplitude Lineshapes	73
B Stripping and Trigger cuts	76
C Details of multivariate classifier	78
D Detailed mass fits	83
E Decay-time Resolution fits	88
F Comparison of time-acceptance in subsamples	92
G Comparison of phase-space acceptance in subsamples	92
H OS tagger calibration parameters	95
I Spin Amplitudes	96
J Considered Decay Chains	97
K Additional information for the time-dependent amplitude fit	98
L Data-simulation comparisson	101
M Data distributions	102
References	108

1 Introduction

This note presents the first measurement of the CKM angle $\gamma \equiv \arg[-(V_{ud}V_{ub}^*)/(V_{cd}V_{cb}^*)]$ using $B_s^0 \rightarrow D_s K\pi\pi$ decays, where the $K\pi\pi$ subsystem is dominated by excited kaon states such as the $K_1(1270)$ and $K_1(1400)$ resonances [1–3]. In these decays, sensitivity to the weak phase results from the interference between $b \rightarrow c$ and $b \rightarrow u$ transitions achieved through $B_s^0 - \bar{B}_s^0$ mixing [4,5]. The amplitudes for both processes are of the same order in the Wolfenstein parameters λ , $\mathcal{O}(\lambda^3)$, so that interference effects are expected to be large. The corresponding Feynman diagrams are shown in Fig. 1.1. Due to the interference between mixing and decay amplitudes, the physical CP violating observables in these decays are functions of a combination of γ and the mixing phase β_s , namely $\gamma - 2\beta_s$. To account for the non-constant strong phase across the phase space, one can either perform a time-dependent amplitude fit or select a suitable phase-space region and introduce a coherence factor as additional hadronic parameter to the decay-time fit, in which case the procedure is very similar to the analysis of $B_s^0 \rightarrow D_s K$ decays [6,7]. Both approaches are explored in this note. The topologically very similar yet flavour specific decay $B_s \rightarrow D_s \pi\pi\pi$ is used as calibration channel, not only to calibrate the tagging algorithms and determine the decay-time acceptance but also to constrain the $B_s^0 - \bar{B}_s^0$ mixing frequency. The branching ration of these decay modes was measured by LHCb to be $\frac{\mathcal{B}(B_s^0 \rightarrow D_s K\pi\pi)}{\mathcal{B}(B_s^0 \rightarrow D_s \pi\pi\pi)} = 0.052 \pm 0.005(\text{stat}) \pm 0.003(\text{syst})$ [1,2].

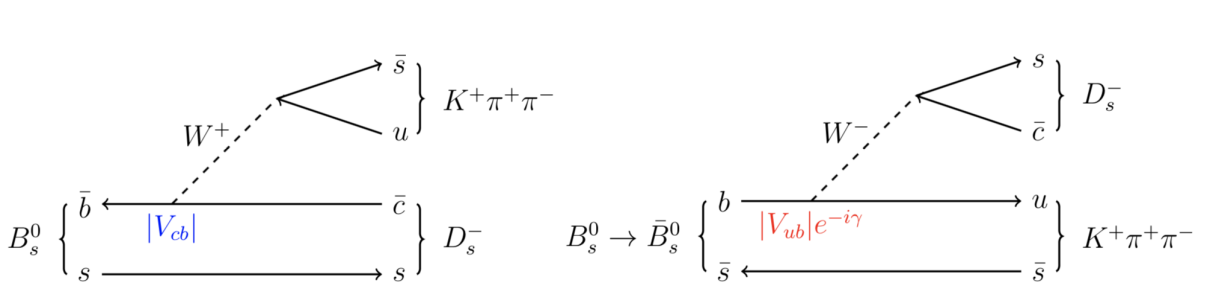


Figure 1.1: Feynman diagram for $B_s^0/\bar{B}_s^0 \rightarrow D_s^- K^+ \pi^+ \pi^-$ decays.

2 Formalism

2.1 Decay rates and CP -observables

The differential decay rate of B_s^0 or \bar{B}_s^0 decays to the final state $D_s^- K^+ \pi\pi$ or $D_s^+ K^- \pi\pi$ is given by:

$$\begin{aligned} \frac{d\Gamma(\mathbf{x}, t, q_t, q_f)}{e^{-\Gamma_s t} dt d\Phi_4} &\propto (|\mathcal{A}_f^c(\mathbf{x})|^2 + |\mathcal{A}_f^u(\mathbf{x})|^2) \cosh\left(\frac{\Delta\Gamma_s t}{2}\right) \\ &\quad + q_t q_f (|\mathcal{A}_f^c(\mathbf{x})|^2 - |\mathcal{A}_f^u(\mathbf{x})|^2) \cos(\Delta m_s t) \\ &\quad - 2\text{Re}(\mathcal{A}_f^c(\mathbf{x})^* \mathcal{A}_f^u(\mathbf{x}) e^{-iq_f(\gamma-2\beta_s)}) \sinh\left(\frac{\Delta\Gamma_s t}{2}\right) \\ &\quad - 2q_t q_f \text{Im}(\mathcal{A}_f^c(\mathbf{x})^* \mathcal{A}_f^u(\mathbf{x}) e^{-iq_f(\gamma-2\beta_s)}) \sin(\Delta m_s t) \end{aligned} \quad (2.1)$$

where $q_t = +1$ (-1) refers to an initially produced B_s^0 (\bar{B}_s^0) flavour eigenstate, $q_t = 0$ to an undetermined initial flavour, $q_f = +1$ or -1 denotes $f = D_s^- K^+ \pi\pi$ or $\bar{f} = D_s^+ K^- \pi\pi$ final states and Γ_s , $\Delta\Gamma_s$ and Δm_s are the width average, the width difference and the mass difference of the two B_s mass eigenstates. We choose a convention in which $\Delta\Gamma_s < 0$ and $\Delta m_s > 0$. We further assume $|q/p| = 1$ for the complex coefficients p and q which relate the B_s meson mass eigenstates to the flavour eigenstates (no CP violation in the mixing). The CKM angle γ can be extracted from the CP violating phase associated to the interference between mixing and decay, $\gamma - 2\beta_s$, since the $B_s^0 - \bar{B}_s^0$ mixing phase, β_s , is well constrained from $B_s \rightarrow J/\psi \phi$ and related modes.

The static total decay amplitudes $\mathcal{A}_f^c(\mathbf{x})$ and $\mathcal{A}_f^u(\mathbf{x})$ are given by the coherent sum over all intermediate state amplitudes $A_i(\mathbf{x})$, each weighted by a complex coefficient describing the relative magnitude and phase which is to be determined from data,

$$\mathcal{A}(B_s^0 \rightarrow D_s^- K^+ \pi\pi) \equiv \mathcal{A}_f^c(\mathbf{x}) = \sum_i a_i^c A_i(\mathbf{x}) \quad (2.2)$$

$$\mathcal{A}(\bar{B}_s^0 \rightarrow D_s^- K^+ \pi\pi) \equiv \mathcal{A}_f^u(\mathbf{x}) = \sum_i a_i^u A_i(\mathbf{x}) \quad (2.3)$$

where the superscript c (u) indicates a $b \rightarrow c$ ($b \rightarrow u$) quark-level transition and \mathbf{x} represents a unique set of kinematic conditions within the five-dimensional phase space of the decay. Convenient choices for the kinematic observables include the invariant mass combinations of the final state particles or acoplanarity and helicity angles. In practice, we do not need to choose a particular five-dimensional basis, but use the full four-vectors of the decay in our analysis. The dimensionality is handled by the phase space element which can be written in terms of any set of five independent kinematic observables, $\mathbf{x} = (x_1, \dots, x_5)$, as

$$d\Phi_4 = \phi_4(\mathbf{x}) d^5x, \quad (2.4)$$

where $\phi_4(\mathbf{x}) = \left| \frac{\partial\Phi_4}{\partial(x_1, \dots, x_5)} \right|$ is the phase space density. In contrast to three-body decays, the four-body phase space density function is not flat in the usual kinematic variables. An analytic expression for ϕ_4 can be found in Ref. [8], but is not needed in practice, see Sec. 7.3.

49 Assuming there is no direct CP violation in the B_s decay implies for the CP conjugate
50 transition amplitudes:

$$\mathcal{A}(\bar{B}_s^0 \rightarrow \bar{f}) = \mathcal{A}_f^c(\mathbf{x}) = \mathcal{A}_f^c(\bar{\mathbf{x}}) \quad (2.5)$$

$$\mathcal{A}(B_s^0 \rightarrow \bar{f}) = \mathcal{A}_{\bar{f}}^u(\mathbf{x}) = \mathcal{A}_{\bar{f}}^u(\bar{\mathbf{x}}) \quad (2.6)$$

51 where the CP -conjugate phase space point $\bar{\mathbf{x}}$ is defined such that it is mapped onto
52 \mathbf{x} by the interchange of final state charges, and the reversal of three-momenta. The
53 phenomenological description of the intermediate state amplitudes is discussed in Sec. 2.2.

54

55 Rather than developing an amplitude model describing the whole phase space, it is also
56 possible to determine the CKM angle γ , in a model-independent way, from the decay-time
57 distribution only. The differential decay rate integrated over the phase space yields:

$$\int \frac{d\Gamma(x, t, q_t, q_f)}{e^{-\Gamma_s t} dt d\Phi_4} \propto \cosh\left(\frac{\Delta\Gamma_s t}{2}\right) + q_t q_f C \cos(\Delta m_s t) \\ + D_f \sinh\left(\frac{\Delta\Gamma_s t}{2}\right) - q_t S_f \sin(\Delta m_s t) \quad (2.7)$$

58 where the same convention for the CP coefficients as for the $B_s \rightarrow D_s K$ analysis is used:

$$C = \frac{1 - r^2}{1 + r^2} \quad (2.8)$$

$$D_f = -\frac{2r\kappa \cos(\delta - q_f(\gamma - 2\beta_s))}{1 + r^2} \quad (2.9)$$

$$S_f = q_f \frac{2r\kappa \sin(\delta - q_f(\gamma - 2\beta_s))}{1 + r^2} \quad (2.10)$$

59 The coherence factor κ , the strong phase difference δ and the ratio of the suppressed
60 ($b \rightarrow u$) over favored ($b \rightarrow c$) decay mode, averaged over the phase space, are defined as:

$$\kappa e^{i\delta} \equiv \frac{\int \mathcal{A}_f^c(x)^* \mathcal{A}_f^u(x) d\Phi_4}{\sqrt{\int |\mathcal{A}_f^c(x)|^2 d\Phi_4} \sqrt{\int |\mathcal{A}_f^u(x)|^2 d\Phi_4}} \quad (2.11)$$

$$r \equiv \frac{\sqrt{\int |\mathcal{A}_f^u(x)|^2 d\Phi_4}}{\sqrt{\int |\mathcal{A}_f^c(x)|^2 d\Phi_4}}. \quad (2.12)$$

61 The five CP coefficients $C, D \equiv D_f, \bar{D} \equiv D_{\bar{f}}, S \equiv S_f, \bar{S} \equiv S_{\bar{f}}$ can be extracted from
62 a fit to the decay-time distribution which allows to infer the four physical observables
63 $r, \delta, \gamma, \kappa$ as discussed in more detail in Sect. 2.4. This approach will be called phase-space
64 integrated fit in the following. In contrast, the approach using Eq. 2.1 will be referred
65 to as full time-dependent amplitude fit. In case of the phase-space integrated fit, the
66 coherence factor dilutes the sensitivity to the weak phase γ due to the integration over
67 the interfering amplitudes across the phase space. The value of κ is bounded between
68 zero and unity. The latter corresponds to the limit of only one contributing intermediate
69 state in which case the same sensitivity as in $B_s \rightarrow D_s K$ decays is reached, while $\kappa = 0$
70 would result in no sensitivity to γ at all.

71 **2.2 Amplitude model**

72 To construct the intermediate state amplitudes $A_i(\mathbf{x})$, the isobar approach is used, which
 73 assumes that the decay process can be factorized into subsequent two-body decay am-
 74 plitudes [9–11]. This gives rise to two different decay topologies; quasi two-body decays
 75 $B_s \rightarrow (R_1 \rightarrow h_1 h_2) (R_2 \rightarrow h_3 h_4)$ or cascade decays $B_s \rightarrow h_1 [R_1 \rightarrow h_2 (R_2 \rightarrow h_3 h_4)]$. In
 76 either case, the intermediate state amplitude is parameterized as a product of orbital
 77 angular momentum, L , dependent form factors B_L , included for each vertex of the decay
 78 tree, Breit-Wigner propagators T_R , included for each resonance R , and an overall angular
 79 distribution represented by a spin factor S ,

$$A_i(\mathbf{x}) = B_{L_{B_s}}(\mathbf{x}) [B_{L_{R_1}}(\mathbf{x}) T_{R_1}(\mathbf{x})] [B_{L_{R_2}}(\mathbf{x}) T_{R_2}(\mathbf{x})] S_i(\mathbf{x}). \quad (2.13)$$

80 The following description of the individual components is adapted from Ref. [12] and
 81 only included for completeness.

82 **2.2.1 Form Factors and Resonance Lineshapes**

83 To account for the finite size of the decaying resonances, the Blatt-Weisskopf penetration
 84 factors, derived in Ref. [13] by assuming a square well interaction potential with radius
 85 r_{BW} , are used as form factors, B_L . They depend on the breakup momentum q , which is
 86 defined as the magnitude of the three-momentum of one of the daughters in the rest frame
 87 of the decaying resonance and the orbital angular momentum L , between the resonance
 88 daughters. Their explicit expressions are

$$\begin{aligned} B_0(q) &= 1, \\ B_1(q) &= 1/\sqrt{1 + (q r_{\text{BW}})^2}, \\ B_2(q) &= 1/\sqrt{9 + 3 (q r_{\text{BW}})^2 + (q r_{\text{BW}})^4}. \end{aligned} \quad (2.14)$$

89 Resonance lineshapes are described as function of the energy-squared, s , by Breit-Wigner
 90 propagators

$$T(s) = \frac{1}{m_0^2 - s - i m_0 \Gamma(s)}, \quad (2.15)$$

91 where the total width, $\Gamma(s)$, is normalized to give the nominal width, Γ_0 , when evaluated
 92 at the nominal mass m_0 .

93 For a decay into two stable particles $R \rightarrow AB$, the energy dependence of the decay
 94 width can be described by

$$\Gamma_{R \rightarrow AB}^{(2)}(s) = \Gamma_0 \frac{m_0}{\sqrt{s}} \left(\frac{q}{q_0} \right)^{2L+1} \frac{B_L(q)^2}{B_L(q_0)^2}, \quad (2.16)$$

95 where q_0 is the value of the breakup momentum at the resonance pole [14].

96 The energy-dependent width for a three-body decay $R \rightarrow ABC$, on the other hand, is
 97 considerably more complicated and has no analytic expression in general. However, it can
 98 be obtained numerically by integrating the transition amplitude-squared over the phase
 99 space,

$$\Gamma_{R \rightarrow ABC}^{(3)}(s) = \frac{1}{2\sqrt{s}} \int |A_{R \rightarrow ABC}|^2 d\Phi_3, \quad (2.17)$$

and therefore requires knowledge of the resonant substructure. The three-body amplitude $A_{R \rightarrow ABC}$ can be parameterized similarly to the four-body amplitude in Eq. (2.13). In particular, it includes form factors and propagators of intermediate two-body resonances.

Both Eq. (2.16) and Eq. (2.17) give only the partial width for the decay into a specific channel. To obtain the total width, a sum over all possible decay channels has to be performed,

$$\Gamma(s) = \sum_i g_i \Gamma_i(s), \quad (2.18)$$

where the coupling strength to channel i , is given by g_i .

Equation (2.16) is used by default for resonances decaying into a two-body final state. For the $K\pi$ and $\pi\pi$ S-wave resonances as well as for the $\rho(770)$ meson more sophisticated parameterizations are employed. Their explicit expressions are given in Appendix A. The nominal masses and widths of the resonances are taken from the PDG [15] with the exceptions described in Appendix K. The running width distributions for various 3-body resonances, calculated from Eq. 2.17, are shown in Appendix A.

Some particles may not originate from a resonance but are in a state of relative orbital angular momentum. We denote such non-resonant states by surrounding the particle system with brackets and indicate the partial wave state with an subscript; for example $(\pi\pi)_S$ refers to a non-resonant di-pion S -wave. The lineshape for non-resonant states is set to unity.

2.2.2 Spin Densities

The spin amplitudes are phenomenological descriptions of decay processes that are required to be Lorentz invariant, compatible with angular momentum conservation and, where appropriate, parity conservation. They are constructed in the covariant Zemach (Rarita-Schwinger) tensor formalism [16–18]. At this point, we briefly introduce the fundamental objects of the covariant tensor formalism which connect the particle’s four-momenta to the spin dynamics of the reaction and give a general recipe to calculate the spin factors for arbitrary decay trees. Further details can be found in Refs. [19, 20].

A spin- S particle with four-momentum p , and spin projection λ , is represented by the polarization tensor $\epsilon_{(S)}(p, \lambda)$, which is symmetric, traceless and orthogonal to p . These so-called Rarita-Schwinger conditions reduce the a priori 4^S elements of the rank- S tensor to $2S + 1$ independent elements in accordance with the number of degrees of freedom of a spin- S state [17, 21].

The spin projection operator $P_{(S)}^{\mu_1 \dots \mu_S \nu_1 \dots \nu_S}(p_R)$, for a resonance R , with spin $S = \{0, 1, 2\}$, and four-momentum p_R , is given by [20]:

$$\begin{aligned} P_{(0)}^{\mu\nu}(p_R) &= 1 \\ P_{(1)}^{\mu\nu}(p_R) &= -g^{\mu\nu} + \frac{p_R^\mu p_R^\nu}{p_R^2} \\ P_{(2)}^{\mu\nu\alpha\beta}(p_R) &= \frac{1}{2} \left[P_{(1)}^{\mu\alpha}(p_R) P_{(1)}^{\nu\beta}(p_R) + P_{(1)}^{\mu\beta}(p_R) P_{(1)}^{\nu\alpha}(p_R) \right] - \frac{1}{3} P_{(1)}^{\mu\nu}(p_R) P_{(1)}^{\alpha\beta}(p_R), \end{aligned} \quad (2.19)$$

where $g^{\mu\nu}$ is the Minkowski metric. Contracted with an arbitrary tensor, the projection operator selects the part of the tensor which satisfies the Rarita-Schwinger conditions.

For a decay process $R \rightarrow AB$, with relative orbital angular momentum L , between particle A and B , the angular momentum tensor is obtained by projecting the rank- L tensor $q_R^{\nu_1} q_R^{\nu_2} \dots q_R^{\nu_L}$, constructed from the relative momenta $q_R = p_A - p_B$, onto the spin- L subspace,

$$L_{(L)\mu_1\dots\mu_L}(p_R, q_R) = (-1)^L P_{(L)\mu_1\dots\mu_L\nu_1\dots\nu_L}(p_R) q_R^{\nu_1} \dots q_R^{\nu_L}. \quad (2.20)$$

Their $|\vec{q}_R|^L$ dependence accounts for the influence of the centrifugal barrier on the transition amplitudes. For the sake of brevity, the following notation is introduced,

$$\begin{aligned} \varepsilon_{(S)}(R) &\equiv \varepsilon_{(S)}(p_R, \lambda_R), \\ P_{(S)}(R) &\equiv P_{(S)}(p_R), \\ L_{(L)}(R) &\equiv L_{(L)}(p_R, q_R). \end{aligned} \quad (2.21)$$

Following the isobar approach, a four-body decay amplitude is described as a product of two-body decay amplitudes. Each sequential two-body decay $R \rightarrow A B$, with relative orbital angular momentum L_{AB} , and total intrinsic spin S_{AB} , contributes a term to the overall spin factor given by

$$\begin{aligned} S_{R \rightarrow AB}(\mathbf{x}|L_{AB}, S_{AB}; \lambda_R, \lambda_A, \lambda_B) &= \varepsilon_{(S_R)}(R) X(S_R, L_{AB}, S_{AB}) L_{(L_{AB})}(R) \\ &\times \Phi(\mathbf{x}|S_{AB}; \lambda_A, \lambda_B), \end{aligned} \quad (2.22)$$

where

$$\Phi(\mathbf{x}|S_{AB}; \lambda_A, \lambda_B) = P_{(S_{AB})}(R) X(S_{AB}, S_A, S_B) \varepsilon_{(S_A)}^*(A) \varepsilon_{(S_B)}^*(B). \quad (2.23)$$

Here, a polarization vector is assigned to the decaying particle and the complex conjugate vectors for each decay product. The spin and orbital angular momentum couplings are described by the tensors $P_{(S_{AB})}(R)$ and $L_{(L_{AB})}(R)$, respectively. Firstly, the two spins S_A and S_B , are coupled to a total spin- S_{AB} state, $\Phi(\mathbf{x}|S_{AB})$, by projecting the corresponding polarization vectors onto the spin- S_{AB} subspace transverse to the momentum of the decaying particle. Afterwards, the spin and orbital angular momentum tensors are properly contracted with the polarization vector of the decaying particle to give a Lorentz scalar. This requires in some cases to include the tensor $\varepsilon_{\alpha\beta\gamma\delta} p_R^\delta$ via

$$X(j_a, j_b, j_c) = \begin{cases} 1 & \text{if } j_a + j_b + j_c \text{ even} \\ \varepsilon_{\alpha\beta\gamma\delta} p_R^\delta & \text{if } j_a + j_b + j_c \text{ odd} \end{cases}, \quad (2.24)$$

where $\varepsilon_{\alpha\beta\gamma\delta}$ is the Levi-Civita symbol and j refers to the arguments of X defined in Eqs. 2.22 and 2.23. Its antisymmetric nature ensures the correct parity transformation behavior of the amplitude. The spin factor for a whole decay chain, for example $R \rightarrow (R_1 \rightarrow AB)(R_2 \rightarrow CD)$, is obtained by combining the two-body terms and performing a sum over all unobservable, intermediary spin projections

$$\sum_{\lambda_{R_1}, \lambda_{R_2}} S_{R \rightarrow R_1 R_2}(\mathbf{x}|L_{R_1 R_2}; \lambda_{R_1}, \lambda_{R_2}) S_{R_1 \rightarrow AB}(\mathbf{x}|L_{AB}; \lambda_{R_1}) S_{R_2 \rightarrow CD}(\mathbf{x}|L_{CD}; \lambda_{R_2}), \quad (2.25)$$

where $\lambda_R = \lambda_A = \lambda_B = \lambda_C = \lambda_D = 0$, $S_{AB} = S_{CD} = 0$ and $S_{R_1 R_2} = L_{R_1 R_2}$, as only pseudoscalar initial/final states are involved.

The spin factors for all decay topologies considered in this analysis are explicitly given in Appendix I.

¹⁶⁴ 2.3 Fit implementation

¹⁶⁵ The hadronic amplitudes are renormalized prior to the amplitude fit such that

$$\int |A_i(\mathbf{x})|^2 d\Phi_4 = 1. \quad (2.26)$$

¹⁶⁶ This allows us to set more intuitive starting values as the amplitude coefficients are all on
¹⁶⁷ a comparable scale. Moreover, the total amplitudes $\mathcal{A}_f^{c(u)}(\mathbf{x})$ are renormalized on-the-fly
¹⁶⁸ (*i.e.* at each minimization step) such that

$$\begin{aligned} & \int |\mathcal{A}_f^{c(u)}(\mathbf{x})|^2 d\Phi_4 = 1 \\ & \arg \left(\int \mathcal{A}_f^c(\mathbf{x})^* \mathcal{A}_f^u(\mathbf{x}) d\Phi_4 \right) = 0. \end{aligned} \quad (2.27)$$

¹⁶⁹ As a result, the average amplitude ratio and strong phase difference between the $b \rightarrow u$ and
¹⁷⁰ $b \rightarrow c$ transitions can be introduced as direct fit parameters instead of derived quantities
¹⁷¹ that have to be calculated from Equation 2.11 after the fit. For the differential decay rate
¹⁷² follows:

$$\begin{aligned} \frac{d\Gamma(\mathbf{x}, t, q, f)}{e^{-\Gamma_s t} dt d\Phi_4} \propto & (|\mathcal{A}_f^c(\mathbf{x})|^2 + r^2 |\mathcal{A}_f^u(\mathbf{x})|^2) \cosh \left(\frac{\Delta\Gamma_s t}{2} \right) \\ & + q_t q_f (|\mathcal{A}_f^c(\mathbf{x})|^2 - r^2 |\mathcal{A}_f^u(\mathbf{x})|^2) \cos (\Delta m_s t) \\ & - 2 r \text{Re} (\mathcal{A}_f^c(\mathbf{x})^* \mathcal{A}_f^u(\mathbf{x}) e^{i\delta - iq_f(\gamma - 2\beta_s)}) \sinh \left(\frac{\Delta\Gamma_s t}{2} \right) \\ & - 2 q_t q_f r \text{Im} (\mathcal{A}_f^c(\mathbf{x})^* \mathcal{A}_f^u(\mathbf{x}) e^{i\delta - iq_f(\gamma - 2\beta_s)}) \sin (\Delta m_s t) \end{aligned} \quad (2.28)$$

¹⁷³ This renormalization procedure was found to be crucial for the fit stability since it reduces
¹⁷⁴ the correlation between the a_i^c and a_i^u amplitude coefficients significantly. Due to the
¹⁷⁵ overall normalization, one of the complex amplitude coefficients a_i^c can be fixed to unity
¹⁷⁶ and since r and δ are included as fit parameters one of the complex amplitude coefficient
¹⁷⁷ a_i^u can be additionally fixed to unity.

¹⁷⁸ We force strong decays in the cascade topology to have the same pattern in $b \rightarrow c$
¹⁷⁹ and $b \rightarrow u$ transitions by the sharing of couplings between related quasi-two-body final
¹⁸⁰ states. For example, given the two a_i^c parameters required for $B_s \rightarrow D_s^- K_1(1270)^+$
¹⁸¹ with $K_1(1270)^+ \rightarrow \rho(770)^0 \pi^+$ and $K_1(1270)^+ \rightarrow K^*(892) \pi^+$, the amplitude $\bar{B}_s \rightarrow$
¹⁸² $D_s^- K_1(1270)^+$ with $K_1(1270)^+ \rightarrow \rho(770)^0 \pi^+$ and $K_1(1270)^+ \rightarrow K^*(892) \pi^+$ only requires
¹⁸³ one additional global complex parameter to represent the different production processes
¹⁸⁴ of $B_s \rightarrow D_s^- K_1(1270)^+$ and $\bar{B}_s \rightarrow D_s^- K_1(1270)^+$, while the relative magnitude and phase
¹⁸⁵ of $K_1(1270)^+ \rightarrow \rho(770)^0 \pi^+$ and $K_1(1270)^+ \rightarrow K^*(892) \pi^+$ are the same regardless of
¹⁸⁶ the production mechanism. For this purpose, multiple decay amplitudes of a three-body
¹⁸⁷ resonance are defined relative to a given reference channel.

188 2.4 Validation

189 The amplitude fit is performed by using the amplitude analysis tool **MINT2**. It was
 190 previously applied to analyze $D^0 \rightarrow 4\pi$ and $D^0 \rightarrow KK\pi\pi$ decays [12] which have an
 191 identical general spin structure (*i.e.* scalar to four scalar decay) to $B_s \rightarrow D_s K\pi\pi$ decays.
 192 In the course of the $D^0 \rightarrow hhhh$ analysis, the implementation of the amplitudes were
 193 extensively cross-checked against other available tools such as **qft++** [22], **AmpGen** [23]
 194 and where possible **EVTGEN** [24]. Since no additional line shapes or spin factors are
 195 needed for this analysis, we consider the amplitude calculation as fully validated.

196 This does, however, not apply to the full time-dependent amplitude pdf which is
 197 newly implemented for this analysis. To cross-check it, we use **EVTGEN** to generate
 198 toy events with time-dependent CP violation according to the **SSD_Cp** event model [24].
 199 Since this event model does not allow for multiple interfering resonances, we generate
 200 only the decay chain $B_s \rightarrow D_s(K_1(1400) \rightarrow K^*(892)\pi)$. Table 2.1 lists the generated
 201 input parameters. The toy data set is fitted with our **MINT2** implementation of the full
 202 time-dependent amplitude pdf and the phasespace-integrated pdf. Flat decay-time and
 203 phase-space acceptances are used. The true ID of the B_s meson is used to tag the initial
 204 flavor (*i.e.* perfect tagging). For technical reasons (the extreme case of perfect resolution
 205 is currently not implemented in our fitter) we smeared the generated decay-times with a
 206 Gaussian of width 45 fs. We use a Gaussian of the same width to convolute the pdf for
 207 fitting. More details of the fit procedures are given in Secs. 10 and 11. The fit projections
 208 are shown in Figs. 2.1 and 2.2.

209 The CP coefficients $C, D, \bar{D}, S, \bar{S}$ are the fit parameters in case of the phasespace-
 210 integrated pdf, which are converted after to the fit to the physical observables r, κ, δ and γ
 211 using the **GammaCombo** package [25]. The obtained 1-CL contours are shown in Fig. 2.3.
 212 The full pdf determines r, δ and γ directly. As shown in Tab. 2.2 and 2.3, the fit results
 213 are in excellent agreement with the generated input values. The phasespace-integrated fit
 214 is, in addition, performed with the **B2DX** fitter used for the $B_s \rightarrow D_s K$ analysis yielding
 215 identical results. Note though that some parts of the **B2DX** fitter have been taken over to
 216 our **MINT2** fitter, such that the implementations are not fully independent.

Table 2.1: Input values used to generate **EVTGEN** toy events according to the **SSD_Cp** event model.

τ	1.5 ps
$\Delta\Gamma$	-0.1 ps^{-1}
Δm_s	17.757 ps^{-1}
r	0.37
κ	1
δ	10.0°
γ	71.1°
β_s	0.0°

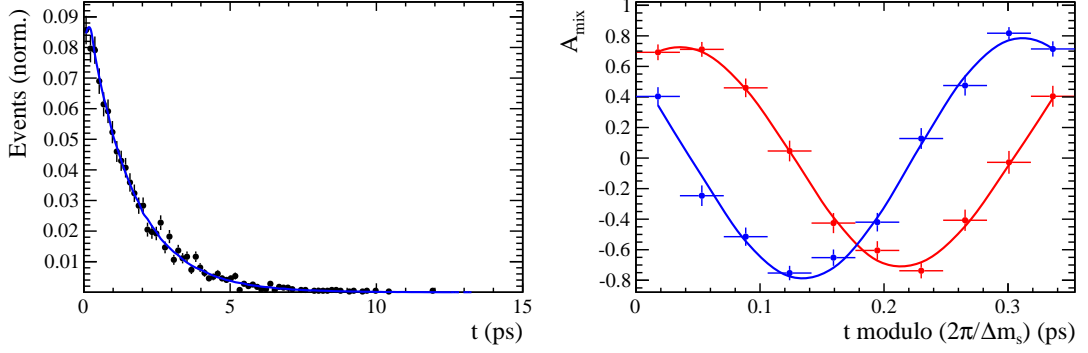


Figure 2.1: Left: Time distribution of $B_s \rightarrow D_s K \pi \pi$ events generated with EVTGEN (points with error bars) and MINT2 fit projections (solid line). Right: Time-dependent asymmetry between mixed and unmixed events folded into one oscillation period for $D_s^- K^+ \pi \pi$ (red) and $D_s^+ K^- \pi \pi$ (blue) final states. The data points show events generated with EVTGEN, while the solid lines show the MINT2 fit projections.

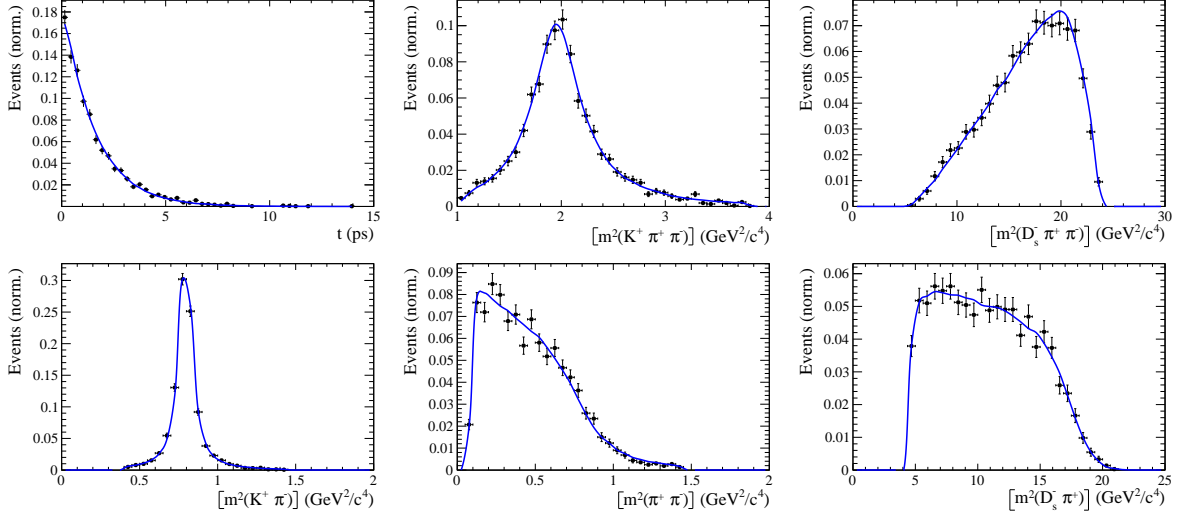


Figure 2.2: Time and invariant mass distributions of $B_s \rightarrow D_s K \pi \pi$ events generated with EVTGEN (points with error bars) and MINT2 fit projections (blue solid line).

Table 2.2: Result of the phasespace-integrated fit to EVTGEN toy events.

	Generated	Fit result	Pull(σ)
C	0.759	0.767 ± 0.023	0.3
D	-0.314	-0.194 ± 0.205	0.6
\bar{D}	-0.101	-0.189 ± 0.210	-0.4
S	-0.570	-0.556 ± 0.033	0.4
\bar{S}	-0.643	-0.683 ± 0.031	-1.3

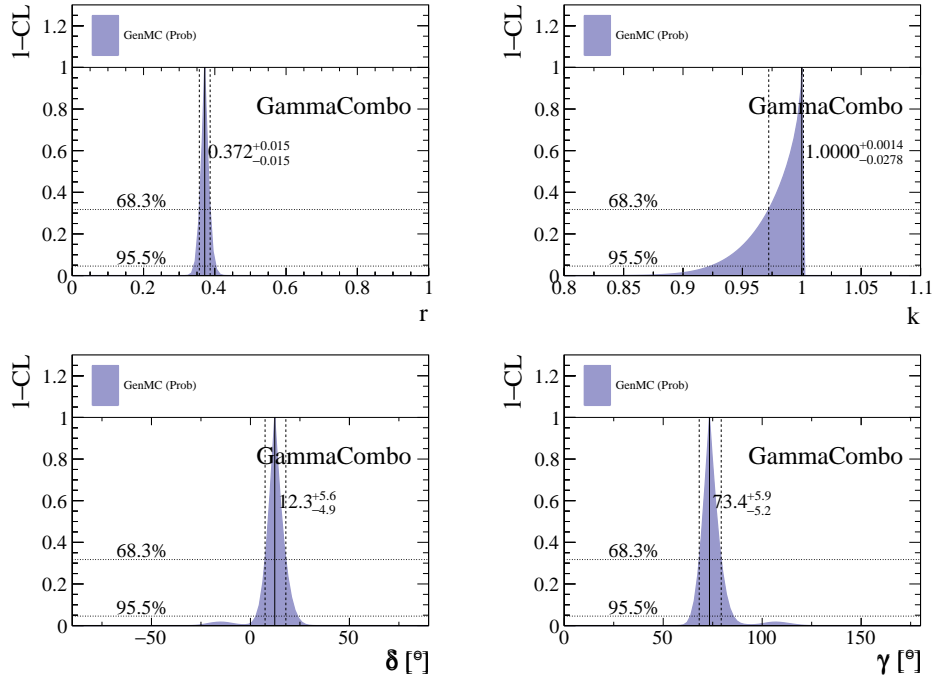


Figure 2.3: The 1-CL contours for the physical observable r, κ, δ and γ obtained with the phasespace-integrated fit to the EVTGEN toy sample.

Table 2.3: Results for the physical observables obtained from fits to EVTGEN toy events.

	Generated	Full PDF	Phasespace-integrated
r	0.370	0.372 ± 0.015	0.372 ± 0.015
κ	1.0	1.0	1.000 ± 0.035
δ	10.0°	12.2 ± 5.1	12.3 ± 5.1
γ	71.1°	73.2 ± 5.5	73.4 ± 5.5

217 3 Analysis strategy

218 The selection of the signal, $B_s \rightarrow D_s K\pi\pi$, and calibration channel, $B_s \rightarrow D_s \pi\pi\pi$, are
219 outlined in Sect. 4, followed by the determination of the signal and background yields. The
220 calibration channel is used to study the decay-time acceptance, see Sect. 7, and to calibrate
221 the flavor tagging algorithms in Sect. 8. Moreover, the B_s mixing frequency is measured
222 in Sect. 10.1. Afterwards, the CKM angle γ is extracted from $B_s \rightarrow D_s K\pi\pi$ data using
223 two different approaches: the results of the phase-space integrated fit are presented in
224 Sect. 10.2, while Sect. 11 discusses the significantly more complicated full time-dependent
225 amplitude fit. The systematic uncertainties of both methods are determined in Sect. 12,
226 before we compare the results and conclude in Sect. 13.

227 4 Data samples and event selection

228 4.1 Stripping and Trigger selection

229 The dataset used for this analysis corresponds to 1 fb^{-1} of proton-proton collision data col-
230 lected in 2011 with a centre of mass energy $\sqrt{s} = 7 \text{ TeV}$, 2 fb^{-1} collected in 2012 with $\sqrt{s} =$
231 7 TeV and 4 fb^{-1} collected in 2015/2016/2017 with $\sqrt{s} = 13 \text{ TeV}$. Candidate $B_s^0 \rightarrow D_s K\pi\pi$
232 ($B_s^0 \rightarrow D_s \pi\pi\pi$) decays are reconstructed using the `B02DKPiPiD2HHHPIDBeauty2CharmLine`
233 (`B02DPiPiPiD2HHHPIDBeauty2CharmLine`) line of the `BHadronCompleteEvent` stream of
234 `Stripping21r1` (2011), `Stripping21` (2012), `Stripping24r1` (2015) and `Stripping28r1p1` (2016)
235 and `Stripping29r2` (2017). Both stripping lines employ the same selection cuts, listed in
236 Appendix B, except for the PID requirement on the bachelor kaon/pion.

237 Events that pass the stripping selection are further required to fulfill the following
238 trigger requirements: at the hardware stage, the B_s^0 candidates are required to be TOS
239 on the `L0Hadron` trigger or TIS on `L0Global`; at Hlt1, B_s^0 candidates are required to be
240 TOS on the `Hlt1TrackAllL0` (`Hlt1TrackMVA` or `Hlt1TwoTrackMVA`) trigger line for Run-I
241 (Run-II) data; at Hlt2, candidates have to be TOS on either one of the 2, 3 or 4-body
242 topological trigger lines or the inclusive ϕ trigger. More details on the used HLT lines are
243 given in Appendix B.

244 Due to a residual kinematic dependence on whether the event is triggered by `L0Hadron`
245 or not and on the data taking condition, the analysis is performed in four disjoint categories:
246 `[Run-I,L0-TOS]`, `[Run-I,L0-TIS]`, `[Run-II,L0-TOS]` and `[Run-II,L0-TIS]`, where for simplic-
247 ity we denote `L0Hadron-TOS` as `L0-TOS` and (`L0Global-TIS` and not `L0Hadron-TOS`) as
248 `L0-TIS`.

249 4.2 Offline selection

250 The offline selection, in particular the requirements on the D_s hadron, are guided by
251 the previous analyses of $B_s \rightarrow D_s K/\pi$, $B_d \rightarrow D^0 \pi$ as well as the branching fraction
252 measurement of $B_s^0 \rightarrow D_s K\pi\pi$ decays. Tables 4.1 and 4.2 summarize all selection
253 requirements which are described in the following. Throughout the note, we abbreviate
254 $B_s^0 \rightarrow D_s X_s (\rightarrow K\pi\pi)$ and $B_s^0 \rightarrow D_s X_d (\rightarrow \pi\pi\pi)$.

255 Given the high number of pp interactions per bunch crossing, a large fraction of
256 events have more than one reconstructed PV. We choose the 'best' PV to be the one
257 to which the B_s candidate has the smallest χ^2_{IP} . In instances where the association

of the B_s candidate to the best PV is wrong, the decay time of this candidate will be incorrect. These wrongly associated candidates are rejected by requiring that the B_s χ^2_{IP} with respect to any other PV is sufficiently higher than with respect to the best PV ($\Delta\chi^2_{IP} = \chi^2_{IP,\text{SECONDBEST}} - \chi^2_{IP,\text{BEST}} > 20$). Events with only a single PV are not affected.

In order to clean up the sample and to align the Run-I to the slightly tighter Run-II stripping selection, we apply the following loose cuts to the b-hadron:

- DIRA > 0.99994
- min IP $\chi^2 < 16$ to the best PV,
- FD $\chi^2 > 100$ to the best PV,
- Vertex $\chi^2/\text{nDoF} < 8$.

The cut on the B_s decay-time is tightened with respect to the stripping selection ($t > 0.2$ ps) because, while offline we use the decay-time determined for a DTF in which the PV position, the D_s and the B_s mass are constrained, in the stripping the simple decay-time returned by a kinematic fit is used. The difference between these two decay-times extends up to 0.1 ps, thus cutting at 0.4 ps avoids any boundary effects and simplifies the time-acceptance studies. We further remove outliers with poorly estimated decay times ($\delta t < 0.15$ ps).

We reconstruct the $B_s^0 \rightarrow D_s h \pi\pi$ decay through three different final states of the D_s meson: $D_s \rightarrow KK\pi$, $D_s \rightarrow \pi\pi\pi$ and $D_s \rightarrow K\pi\pi$. Of those, $D_s \rightarrow KK\pi$ is the most prominent one, while $\mathcal{BR}(D_s \rightarrow \pi\pi\pi) \approx 0.2 \cdot \mathcal{BR}(D_s \rightarrow KK\pi)$ and $\mathcal{BR}(D_s \rightarrow K\pi\pi) \approx 0.12 \cdot \mathcal{BR}(D_s \rightarrow KK\pi)$ holds for the others. For the $KK\pi$ final state we make use of the well known resonance structure; the decay proceeds either via the narrow ϕ resonance, the broader K^{*0} resonance or (predominantly) non-resonant. Within the ϕ resonance region the sample is already sufficiently clean after the stripping so that we do not impose additional criteria on the D_s daughters. For the K^{*0} and non-resonant regions consecutively tighter requirements on the particle identification and the D_s flight-distance are applied. We apply global requirements (*i.e.* independent of the D_s Dalitz-plot position) for the other final states. All cuts are summarized in Table 4.1.

4.2.1 Phase space region

Due to the comparably low masses of the final state particles with respect to the B_s mass, there is, in contrast to for example b-hadron to charmonia or charm decays, a huge phase-space available for the $B_s^0 \rightarrow D_s K\pi\pi$ decay. For the invariant mass of the $K\pi\pi$ subsystem it extends up to 3.4 GeV. It has however been observed that the decay proceeds predominantly through the low lying axial vector states $K_1(1270)$ and $K_1(1400)$, while the combinatorial background is concentrated at high $K\pi\pi$ invariant masses ($m(K\pi\pi) > 2000$ MeV). Moreover, the strange hadron spectrum above 2 GeV is poorly understood experimentally such that a reliable extraction of the strong phase motion in that region is not possible. We consequently choose to limit the considered phase space region to $m(K\pi\pi) < 1950$ MeV, which is right below the charm-strange threshold ($B_s^0 \rightarrow D_s^+ D_s^-$).

297 **4.2.2 Physics background vetoes**

298 We veto various physical backgrounds, which have either the same final state as our
 299 signal decay, or can contribute via a single misidentification of $K \leftrightarrow \pi$, $K \leftrightarrow p$ or $\pi \leftrightarrow p$.
 300 Depending on the D_s final state different vetoes are applied in order to account for peaking
 301 backgrounds originating from charm meson or charmed baryon decays.

302 1. $D_s^- \rightarrow K^+ K^- \pi^-$

303 (a) $D^- \rightarrow K^+ \pi^- \pi^-$:

304 Possible with $\pi^- \rightarrow K^-$ misidentification, vetoed by requiring $m(K^+ K_\pi^- \pi^-) \neq$
 305 $m(D^-) \pm 40$ MeV or the K^- has to fulfill more stringent PID criteria depending
 306 on the resonant region (see Table 4.1).

307 (b) $\Lambda_c^- \rightarrow K^+ \bar{p} \pi^-$:

308 Possible with $\bar{p} \rightarrow K^-$ misidentification, vetoed by requiring $m(K^+ K_p^- \pi^-) \neq$
 309 $m(\Lambda_c^-) \pm 40$ MeV or the K^- has to fulfill more stringent PID criteria depending
 310 on the resonant region (see Table 4.1).

311 (c) $D^0 \rightarrow KK$:

312 D^0 combined with a random π can fake a $D_s \rightarrow KK\pi$ decay, vetoed by
 313 requiring $m(KK) < 1840$ MeV.

314 2. $D_s^- \rightarrow \pi^+ \pi^- \pi^-$

315 (a) $D^0 \rightarrow \pi\pi$:

316 D^0 combined with a random π can fake a $D_s \rightarrow \pi\pi\pi$ decay, vetoed by requiring
 317 both possible combinations to have $m(\pi\pi) < 1700$ MeV.

318 3. $D_s^- \rightarrow K^- \pi^+ \pi^-$

319 (a) $D^- \rightarrow \pi^- \pi^+ \pi^-$:

320 Possible with $\pi^- \rightarrow K^-$ misidentification, vetoed by requiring $m(K_\pi^- \pi^+ \pi^-) \neq$
 321 $m(D^-) \pm 40$ MeV or $\text{PIDK}(K^+) > 15$.

322 (b) $\Lambda_c^- \rightarrow \bar{p} \pi^+ \pi^-$:

323 Possible with $\bar{p} \rightarrow K^-$ misidentification, vetoed by requiring $m(K_p^- \pi^+ \pi^-) \neq$
 324 $m(\Lambda_c^-) \pm 40$ MeV or $\text{PIDK}(K^-) - \text{PIDp}(K^-) > 5$.

325 (c) $D^0 \rightarrow K\pi$:

326 D^0 combined with a random π can fake a $D_s \rightarrow K\pi\pi$ decay, vetoed by requiring
 327 both possible combinations to have $m(K\pi) < 1750$ MeV.

328 The effects of these veto cuts are illustrated in Figs. 4.1,4.2 and 4.3. To reduce cross-feed
 329 from our calibration channel into the signal channel and vice-versa we require tight PID
 330 cuts on the ambiguous bachelor track; for the signal channel we apply $\text{PIDK}(K^+) > 10$
 331 and for the calibration channel $\text{PIDK}(\pi^+) < 0$. In addition, we veto $B_s^0 \rightarrow D_s^- D_s^+$ decays
 332 which is illustrated in Fig. 4.4.

- 333 1. $X_s^+ \rightarrow K^+\pi^+\pi^-$:
- 334 (a) $B_s^0 \rightarrow D_s\pi\pi\pi$:
 335 Possible with $\pi^+ \rightarrow K^+$ misidentification, suppressed with $\text{PIDK}(K^+) > 10$.
- 336 (b) $B_s^0 \rightarrow D_s^-(D_s^+ \rightarrow K^+\pi^+\pi^-)$:
 337 Outside of considered phase-space region, see Sec. 4.2.1.
- 338 (c) $B_s^0 \rightarrow D_s^-(D_s^+ \rightarrow K^+K^-\pi^+)$:
 339 To suppress $B_s^0 \rightarrow D_s^-K^+K^-\pi^+$ background, possible with $K^- \rightarrow \pi^-$ misiden-
 340 tification, we require $\text{PIDK}(\pi^-) < 0$. In case the invariant mass of the $K^+\pi^+\pi^-$
 341 system recomputed applying the kaon mass hypothesis to the pion is close to
 342 the D_s mass ($m(K^+\pi^+\pi_K^-) = m(D_s) \pm 20$ MeV), we further tighten the cut to
 343 $\text{PIDK}(\pi^-) < -5$.
- 344 2. $X_d^+ \rightarrow \pi^+\pi^+\pi^-$:
- 345 (a) $B_s^0 \rightarrow D_sK\pi\pi$:
 346 Possible with single missID of $K^+ \rightarrow \pi^+$, suppressed with $\text{PIDK}(\pi^+) < 0$.
- 347 (b) $B_s^0 \rightarrow D_s^-(D_s^+ \rightarrow \pi^+\pi^+\pi^-)$:
 348 Outside of considered phase-space region, see Sec. 4.2.1.
- 349 (c) $B_s^0 \rightarrow D_s^-(D_s^+ \rightarrow K^+\pi^-\pi^+)$:
 350 Possible with single missID of $K^+ \rightarrow \pi^+$, vetoed by requiring $m(\pi^+\pi_K^+\pi^-) \neq$
 351 $m(D_s) \pm 20$ MeV or $\text{PIDK}(\pi^+) < -5$ for both π^+ .

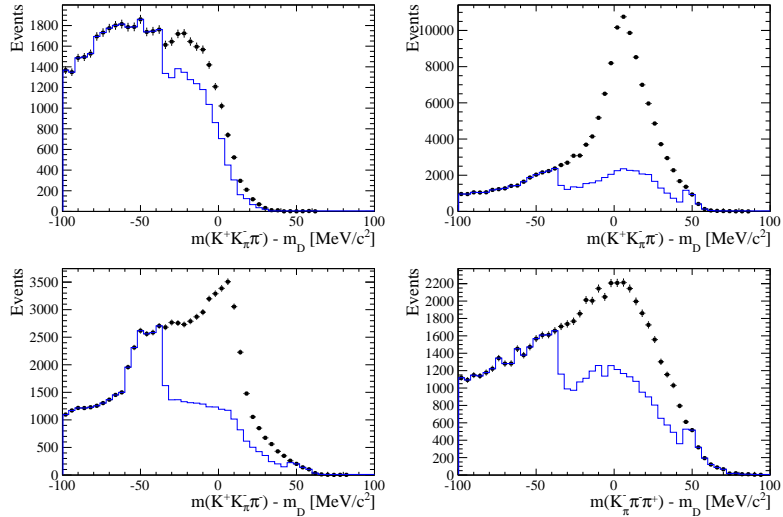


Figure 4.1: Background contributions from D^- decays where the π^- is misidentified as K^- . The D_s invariant mass is recomputed applying the pion mass hypothesis to the kaon and shown for the $D_s \rightarrow \phi\pi$, $D_s \rightarrow K^*(892)K$, $D_s \rightarrow KK\pi$ (non-resonant) and $D_s \rightarrow K\pi\pi$ final state categories from top-left to bottom-right. The distributions are shown without (black) and with (blue) the D^- -veto applied.

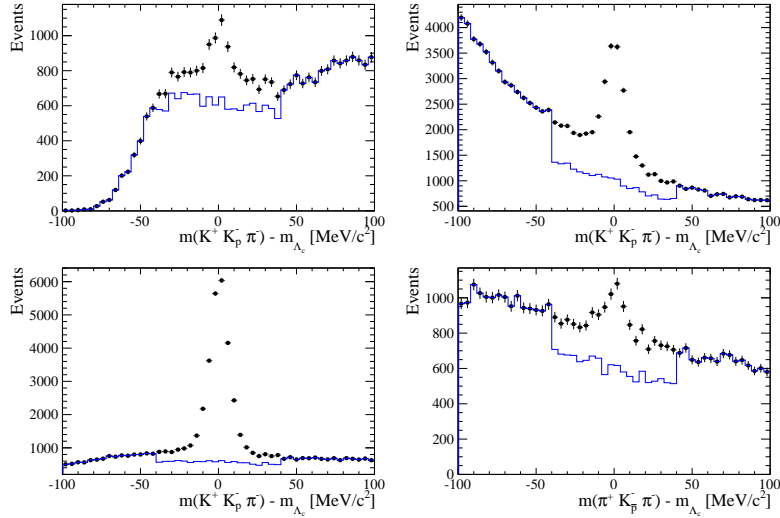


Figure 4.2: Background contributions from Λ_c decays where the \bar{p} is misidentified as K^- . The D_s invariant mass is recomputed applying the proton mass hypothesis to the kaon and shown for the $D_s \rightarrow \phi\pi$, $D_s \rightarrow K^*(892)K$, $D_s \rightarrow KK\pi$ (non-resonant) and $D_s \rightarrow K\pi\pi$ final state categories from top-left to bottom-right. The distributions are shown without (black) and with (blue) the Λ_c -veto applied.

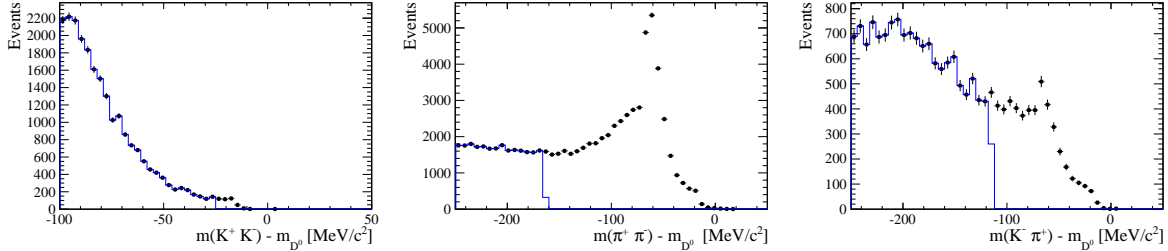


Figure 4.3: Background contributions to $D_s \rightarrow KK\pi$ (left), $D_s \rightarrow \pi\pi\pi$ (middle) and $D_s \rightarrow K\pi\pi$ (right) from $D^0 \rightarrow hh$ decays combined with a random pion. The peak at $m(\pi\pi) - m(D^0) \approx -60$ MeV ($m(K\pi) - m(D^0) \approx -60$ MeV) are due to $D^0 \rightarrow K\pi$ ($D^0 \rightarrow KK$) where a kaon is misidentified as pion.

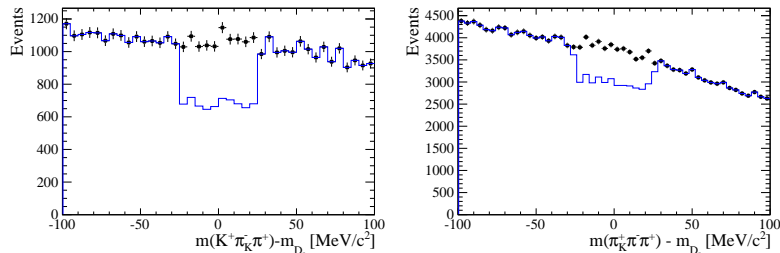


Figure 4.4: Background contributions to $B_s \rightarrow D_s K\pi\pi$ (left) and $B_s \rightarrow D_s \pi\pi\pi$ (right) from $B_s \rightarrow D_s D_s$ decays where the kaon is misidentified as pion. The $X_{s,d}$ invariant mass is recomputed applying the kaon mass hypothesis to the pion and shown without (black) and with (blue) the D_s -veto applied.

352 **4.2.3 Training of multivariate classifier**

353 The Toolkit for Multivariate Analysis (TMVA [26]) is used to train a multivariate classifier
 354 (BDT with gradient boosting, BDTG) discriminating signal and combinatorial background.
 355 We use $B_s \rightarrow D_s \pi\pi$ data that passes all previously mentioned selection steps, including
 356 the trigger and stripping selection, offline cuts and physical background vetoes, as signal
 357 proxy. The background is statistically subtracted by applying `sWeights` based on the
 358 fit to the reconstructed B_s mass shown in Fig. 4.5(left). This is a simplified version
 359 (performed in a reduced mass range) of the final mass fits described in Sec. 5. The
 360 sideband $B_s \rightarrow D_s K\pi\pi$ data ($m(B_s) > 5500$ MeV) is used as background proxy.

361 Training the classifier on a sub-sample which is supposed to be used in the final analysis
 362 might cause a bias, as the classifier selects, in case of overtraining, the training events
 363 more efficiently. As overtraining can not be completely avoided, we split the signal and
 364 the background training samples into two disjoint subsamples according to whether the
 365 event number is even or odd. We then train the classifier on the even sample and apply it
 366 to the odd one, and vice-versa (cross-training).

367 The following discriminating variables are used for the BDTG training¹:

- 368 • logarithm of the B_s impact-parameter χ^2 , $B_s \log(\chi_{IP}^2)$
- 369 • logarithm of the cosine of the B_s direction angle, $\log(\text{DIRA})$
- 370 • fit quality of the DTF with PV constrain, χ_{DTF}^2/ndf
- 371 • logarithm of the minimal B_s^0 decay vertex quality difference for adding one extra
 372 track, $\log(\Delta\chi_{add-track}^2)$
- 373 • the difference between the transverse momentum of the B_s - candidate and the
 374 transverse momentum of all the particles reconstructed with a cone of radius
 375 $r = \sqrt{(\Delta\Phi)^2 + (\Delta\eta)^2} < 1$ rad around the B_s - candidate normalized to the sum of
 376 both, $B_s A_{pT}^{\text{cone}}$
- 377 • largest ghost probability of all tracks, $\max(\text{ghostProb})$
- 378 • logarithm of the the smallest $X = X_d, X_s$ daughter impact-parameter χ^2 , $X \log(\min(\chi_{IP}^2))$
- 379 • largest distance of closest approach of the $X = X_d, X_s$ daughters, $\max(\text{DOCA})$
- 380 • cosine of the largest opening angle between the D_s and another bachelor track h_i in
 381 the plane transverse to the beam, $\cos(\max \theta_{D_s h_i})$
- 382 • logarithm of the the smallest D_s daughter impact-parameter χ^2 , $D_s \log(\min(\chi_{IP}^2))$
- 383 • logarithm of the D_s flight-distance significance, $D_s \log(\chi_{FD}^2)$
- 384 • logarithm of the D_s radial flight-distance, $D_s \log(RFD)$

¹ The following options are chosen: NTrees=500, MinNodeSize=2.5%, BoostType=Grad:Shrinkage=0.10, UseBaggedBoost:BaggedSampleFraction=0.5, nCuts=40, MaxDepth=3, NegWeightTreatment=Pray.

386 Loose cuts on the variables χ^2_{DTG}/ndf , $\Delta\chi^2_{add-track}$ and $\cos(\max\theta_{D_s h_i})$ are applied prior
 387 to the training which are expected to be 100% signal efficient. Figure 4.6 shows the
 388 distributions of the input variables for signal and background. As shown in Appendix C,
 389 these distributions differ between data-taking period and trigger category. In particular
 390 variables depending on the B_s kinematics and the event multiplicity are affected (*e.g.*
 391 $\theta_{D_s h_i}$ or A_{pT}^{cone}). The BDTG is consequently trained separately for these categories. The
 392 resulting classifier response is shown in Fig. 4.7 for each category (even and odd test
 393 samples combined) and in Appendix C for each training.

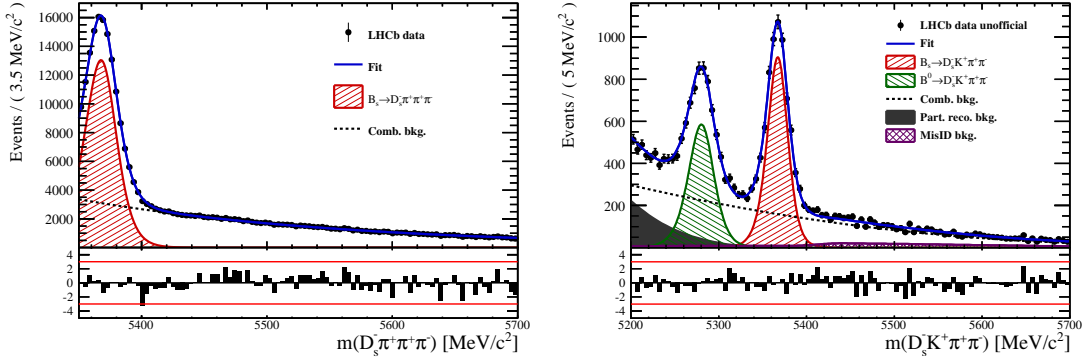


Figure 4.5: Left: Reconstructed B_s mass for $B_s \rightarrow D_s \pi\pi\pi\pi$ events that pass the preselection (all categories combined). The fitted PDF is shown in blue, the signal component in red and the background component in black.

Right: Reconstructed B_s mass for $B_s \rightarrow D_s K\pi\pi$ events that pass the $BDTG > 0$ requirement (all categories combined).

394 4.2.4 Final selection

395 The cut on the BDTG output is optimized using the signal significance as figure of merit:

$$FOM(BDTG) = \frac{N_s(BDTG)}{\sqrt{N_s(BDTG) + N_b(BDTG)}} \quad (4.1)$$

396 where $N_s(BDTG)$ is the $B_s \rightarrow D_s K\pi\pi$ signal yield for a given BDTG cut and $N_b(BDTG)$
 397 is the combinatorial background yield in the signal region ($m(D_s K\pi\pi) = m_{B_s} \pm 40$ MeV).
 398 To compute the yields as function of the BDTG cut, we use the BDTG efficiencies, $\epsilon_{s,b}$,
 399 evaluated on the corresponding test samples. To fix the overall scale, it is required to
 400 know the yields at (at least) one point of the scanned range. We arbitrarily choose this
 401 fix point to be $BDTG > 0$ and perform a fit to the reconstructed B_s mass as described
 402 in Sec. 5 to obtain the yields $N_{s,b}(0)$, see Fig. 4.5(right). These yields are then efficiency
 403 corrected to calculate the yields for a given BDTG cut:

$$N_{s,b}(BDTG) = N_{s,b}(0) \cdot \frac{\epsilon_{s,b}(BDTG)}{\epsilon_{s,b}(0)}. \quad (4.2)$$

404 Figure 4.8 shows the resulting BDTG scans for each training category.

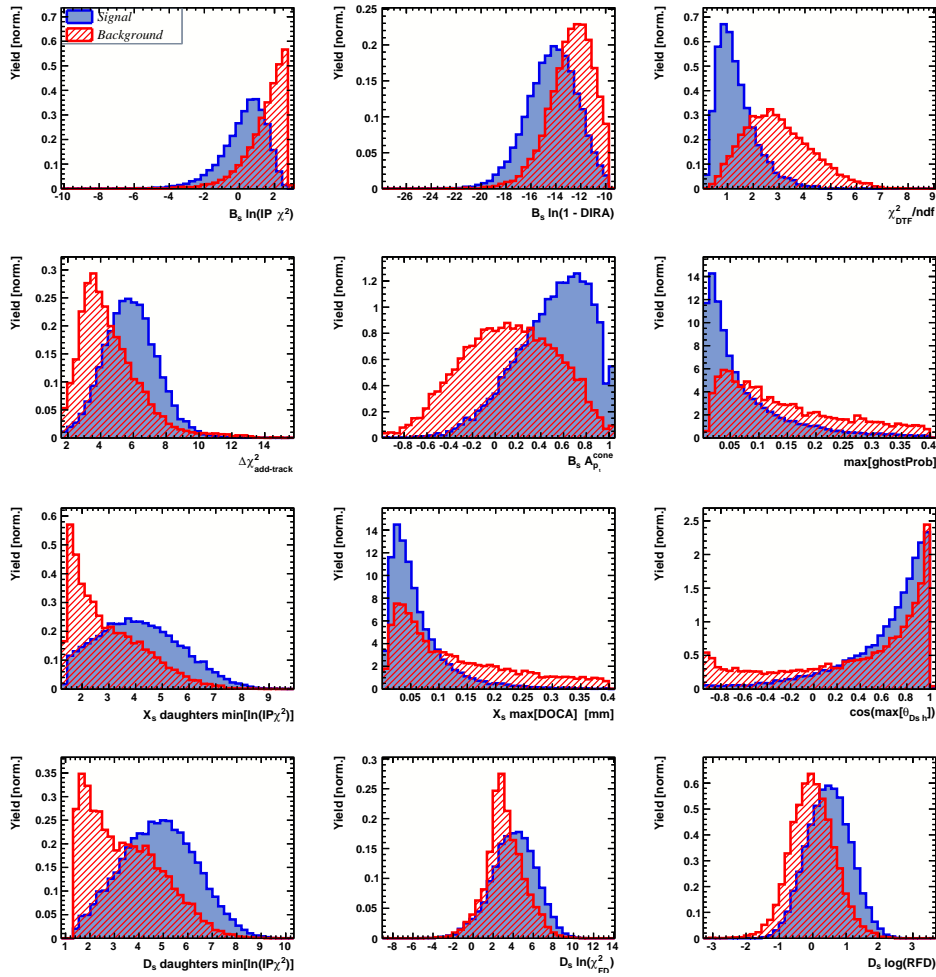


Figure 4.6: Discriminating variables used to train the BDTG for all data categories combined.

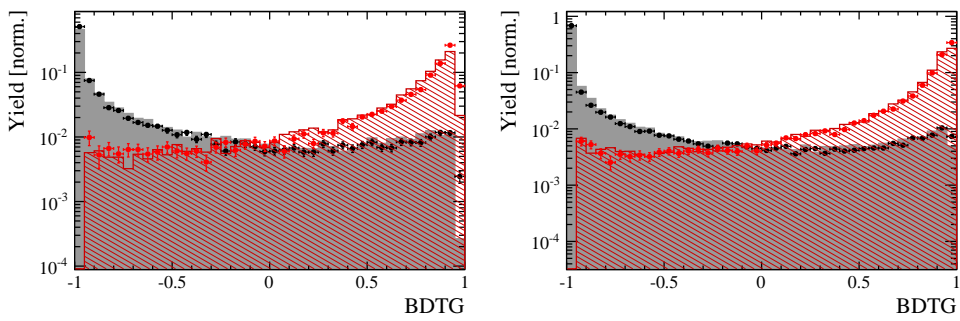


Figure 4.7: Signal (red) and background (black) distributions for the BDTG response for Run-I (left) and Run-II (right) data. Filled histograms (data points) show the BDTG response for the L0-TOS (L0-TIS) category. Even and odd test samples are combined.

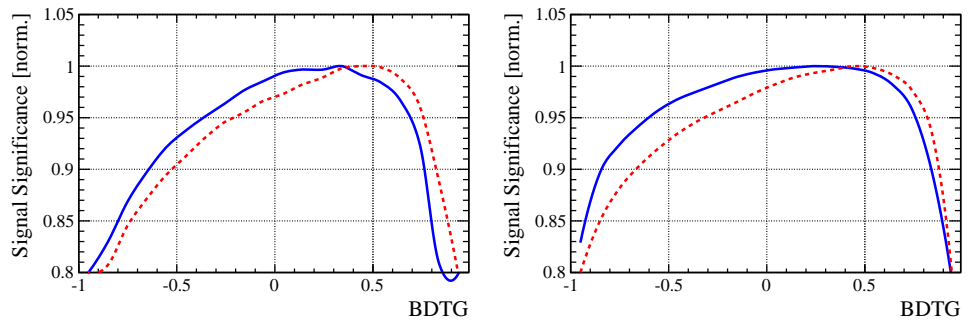


Figure 4.8: Signal significance as function of the applied cut on the BDTG response for Run-I (left) and Run-II (right) data. The scans for the L0-TOS (L0-TIS) category are shown in blue (red). The signal significance is normalized to be 1 at the optimal BDTG cut value.

Table 4.1: Offline selection requirements for $D_s \rightarrow 3h$ candidates.

	Description	Requirement
$D_s \rightarrow hh\bar{h}$	$m(hh\bar{h})$	$= m_{D_s} \pm 25$ MeV
$D_s^- \rightarrow KK\pi^-$	D^0 veto	$m(KK) < 1840$ MeV
$D_s^- \rightarrow \phi\pi^-$	$m(KK)$ PIDK(K^+) PIDK(K^-) PIDK(π^-) χ_{FD}^2 FD in z D^- veto Λ_c veto	$= m_\phi \pm 12$ MeV > -10 > -10 < 20 > 0 > -1 $m(K^+K_\pi^-\pi^-) \neq m(D^-) \pm 40$ MeV PIDK(K^-) > 5 $m(K^+K_p^-\pi^-) \neq m(\Lambda_c) \pm 40$ MeV PIDK(K^-) – PIDp(K^-) > 2
$D_s^- \rightarrow K^*(892)K^-$	$m(KK)$ $m(K^+\pi^-)$ PIDK(K^+) PIDK(K^-) PIDK(π^-) χ_{FD}^2 FD in z D^- veto Λ_c veto	$\neq m_\phi \pm 12$ MeV $= m_{K^*(892)} \pm 75$ MeV > -10 > 0 < 10 > 0 > 0 $m(K^+K_\pi^-\pi^-) \neq m(D^-) \pm 40$ MeV PIDK(K^-) > 15 $m(K^+K_p^-\pi^-) \neq m(\Lambda_c) \pm 40$ MeV PIDK(K^-) – PIDp(K^-) > 5
$D_s^- \rightarrow (KK\pi^-)_{NR}$	$m(KK)$ $m(K^+\pi^-)$ PIDK(K^+) PIDK(K^-) PIDK(π^-) χ_{FD}^2 FD in z D^- veto Λ_c veto	$\neq m_\phi \pm 12$ MeV $\neq m_{K^*(892)} \pm 75$ MeV > 5 > 5 < 10 > 4 > 0 $m(K^+K_\pi^-\pi^-) \neq m(D^-) \pm 40$ MeV PIDK(K^-) > 15 $m(K^+K_p^-\pi^-) \neq m(\Lambda_c) \pm 40$ MeV PIDK(K^-) – PIDp(K^-) > 5
$D_s^- \rightarrow \pi\pi\pi$	PIDK(π) PIDp(π) D^0 veto χ_{FD}^2 FD in z	< 10 < 20 $m(\pi^+\pi^-) < 1700$ MeV > 9 > 0
$D_s^- \rightarrow K^-\pi^+\pi^-$	PIDK(K) PIDK(π) PIDp(π) D^0 veto χ_{FD}^2 FD in z D^- veto Λ_c veto	> 8 < 5 < 20 $m(K^-\pi^+) < 1750$ MeV > 9 > 0 $m(K_\pi^-\pi^+\pi^-) \neq m(D^-) \pm 40$ MeV PIDK(K^-) > 15 $m(K_p^-\pi^+\pi^-) \neq m(\Lambda_c) \pm 40$ MeV PIDK(K^-) – PIDp(K^-) > 5

Table 4.2: Offline selection requirements for $B_s \rightarrow D_s K\pi\pi(D_s\pi\pi\pi)$ candidates.

	Description	Requirement
$B_s \rightarrow D_s h\pi\pi$	$m(D_s h\pi\pi)$	$> 5200 \text{ MeV}$
	χ^2_{vtx}/ndof	< 8
	DIRA	> 0.99994
	χ^2_{FD}	> 100
	χ^2_{IP}	< 16
	χ^2_{DTF}/ndof	< 15
	$\Delta\chi^2_{add-track}$	> 2
	$\cos(\max \theta_{D_s h_i})$	> -0.9
	t	$> 0.4 \text{ ps}$
	δt	$< 0.15 \text{ ps}$
	Phasespace region	$m(h\pi\pi) < 1.95 \text{ GeV}$ $m(h\pi) < 1.2 \text{ GeV}$ $m(\pi\pi) < 1.2 \text{ GeV}$
Wrong PV veto		$\text{nPV} = 1 \parallel \min(\Delta\chi^2_{IP}) > 20$
BDTG		$> 0.35 \text{ [Run-I,L0-TOS]}$ $> 0.45 \text{ [Run-I,L0-TIS]}$ $> 0.25 \text{ [Run-II,L0-TOS]}$ $> 0.45 \text{ [Run-II,L0-TIS]}$
$X_s^+ \rightarrow K^+\pi^+\pi^-$	PIDK(K)	> 10
	PIDK(π^+)	< 10
	PIDK(π^-)	< 0
	D_s veto	$m(K^+\pi^+\pi_K^-) \neq m(D_s) \pm 20 \text{ MeV} \parallel \text{PIDK}(\pi^-) < -5$
$X_d^+ \rightarrow \pi^+\pi^+\pi^-$	PIDK(π^+)	< 0
	PIDK(π^-)	< 10
	D_s veto	$m(\pi^+\pi_K^+\pi^-) \neq m(D_s) \pm 20 \text{ MeV} \parallel \text{PIDK}(\pi^+) < -5$
All tracks	hasRich	$= 1$

405 4.3 Simulation

406 Several Monte Carlo (MC) samples are used in the analysis for acceptance and background
 407 studies. A full list of them is given in Tab. 4.3. In each case, the decay model includes
 408 a mixture of non-interfering resonances contributing to the bachelor system and a non-
 409 resonant (phase-space) component. For $B_s \rightarrow D_s X_s$ these are: 25% $X_s \rightarrow \pi(K_1(1270) \rightarrow$
 410 $K\rho(770))$, 70% $X_s \rightarrow \pi(K_1(1400) \rightarrow K^*(892)\pi)$ and 5% $X_s \rightarrow K\pi\pi$ (non-resonant). And
 411 similar for $B_s \rightarrow D_s X_d$: 85% $X_d \rightarrow \pi(a_1(1260) \rightarrow \rho(770)\pi)$, 10% $X_d \rightarrow \pi(a_1(1260) \rightarrow \sigma\pi)$
 412 and 5% $X_d \rightarrow K\pi\pi$ (non-resonant). All MC samples are generated using Pythia8,
 413 reconstructed using Reco14c, Reco15 and Reco16 for Run-I, 15 and 16 data and selected
 414 using the same criteria as in data.

Table 4.3: List of simulated samples used in the analysis.

Decay	Event Type	Sim	Statistics				Filter
			11	12	15	16	
$B_s \rightarrow (D_s \rightarrow KK\pi)K\pi\pi$	13266007	08i	1.2 M	1.2 M	-	-	Generator Level
$B_s \rightarrow (D_s \rightarrow KK\pi)K\pi\pi$	13266008	09c	70 k	80 k	50 k	100 k	Generator Level, Stripping
$B_s \rightarrow (D_s \rightarrow K\pi\pi)K\pi\pi$	13266058	09c	70 k	80 k	50 k	100 k	Generator Level, Stripping
$B_s \rightarrow (D_s \rightarrow \pi\pi\pi)K\pi\pi$	13266038	09c	70 k	80 k	50 k	100 k	Generator Level, Stripping
$B_s \rightarrow (D_s \rightarrow KK\pi)\pi\pi\pi$	13266006	08i	1.2 M	1.2 M	-	-	Generator Level
$B_s \rightarrow (D_s \rightarrow KK\pi)\pi\pi\pi$	13266068	09c	70 k	80 k	50 k	100 k	Generator Level, Stripping
$B_s \rightarrow (D_s \rightarrow K\pi\pi)\pi\pi\pi$	13266088	09c	70 k	80 k	50 k	100 k	Generator Level, Stripping
$B_s \rightarrow (D_s \rightarrow \pi\pi\pi)\pi\pi\pi$	13266078	09c	70 k	80 k	50 k	100 k	Generator Level, Stripping
$B_s \rightarrow D_s^*\pi\pi\pi, D_s \rightarrow KK\pi$	13266201	08i	1.2 M	1.2 M	-	-	Generator Level

415 5 Yields determination

416 An extended unbinned maximum likelihood fit to the reconstructed B_s mass of the selected
 417 events is performed in order to determine the signal and background yields. The invariant
 418 mass $m(D_s h\pi\pi)$ is determined from a DTF constraining the mass of the D_s to the PDG
 419 value and the position of the PV. The probability density functions (PDFs) used to
 420 describe the signal and background components are described in the following.

421 Due to different mass resolutions, we perform the invariant mass fits simultaneously
 422 for each data-taking period and each trigger category. We further introduce four D_s final
 423 state categories: $D_s \rightarrow \phi\pi$, $D_s \rightarrow K^*(892)\pi$, $D_s \rightarrow \pi\pi\pi$ and $D_s \rightarrow Kh\pi$ to account for
 424 different signal purities. The $D_s \rightarrow Kh\pi$ category combines the two D_s decay channels
 425 with the lowest statistics: $D_s \rightarrow KK\pi$ (non-resonant) and $D_s \rightarrow K\pi\pi$. This amounts to
 426 16 categories in total.

427 5.1 Signal model

428 The signal B_s -mass distribution of both $B_s^0 \rightarrow D_s K\pi\pi$ and $B_s^0 \rightarrow D_s \pi\pi\pi$ is modeled
 429 using a Johnson's SU function [27], which results from a variable transformation of a
 430 normal distribution to allow for asymmetric tails:

$$\mathcal{J}(x|\mu, \sigma, \nu, \tau) = \frac{e^{-\frac{1}{2}r^2}}{2\pi \cdot c \cdot \sigma \cdot \tau \cdot \sqrt{z^2 + 1}} \quad (5.1)$$

$$r = -\nu + \frac{\operatorname{asinh}(z)}{\tau} \quad (5.2)$$

$$z = \frac{x - (\mu - c \cdot \sigma \cdot e^\tau \sinh(\nu \cdot \tau))}{c \cdot \tau} \quad (5.3)$$

$$c = \frac{e^{\tau^2} - 1}{2\sqrt{e^{\tau^2} \cdot \cosh(2\nu \cdot \tau) + 1}}. \quad (5.4)$$

431 It is conveniently expressed in terms of the central moments up to order four: The mean
 432 of the distribution μ , the standard deviation σ , the skewness ν and the kurtosis τ . The
 433 tail parameters ν and τ are fixed to the values obtained by a fit to the invariant mass
 434 distribution of simulated events shown in Fig 5.1. To account for differences between
 435 simulation and real data, linear scaling factors for the mean μ and width σ are determined
 436 in the fit to $B_s^0 \rightarrow D_s \pi\pi\pi$ data and later fixed in the fit to $B_s^0 \rightarrow D_s K\pi\pi$ decays. The scale
 437 factors are determined separately for each data-taking period and each trigger category.

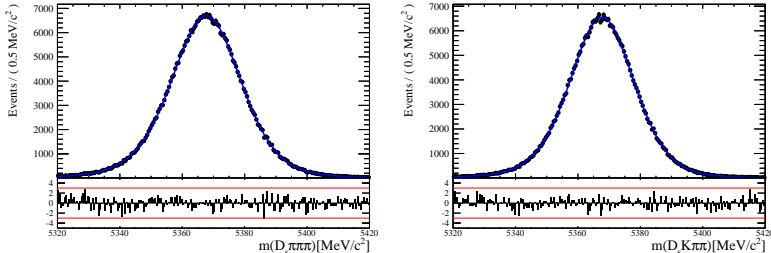


Figure 5.1: Invariant mass distributions of simulated (left) $B_s^0 \rightarrow D_s \pi\pi\pi$ and (right) $B_s^0 \rightarrow D_s K\pi\pi$ events. A fit with a Johnson's SU PDF is overlaid.

438 **5.2 Background models**

439 After the full selection the following residual background components have to be accounted
440 for:

441

442 **Combinatorial background**

443 The combinatorial background is described by a second order polynomial, whose
444 parameters are determined, for each D_s final state separately, in the fit to data. For
445 systematic studies an exponential PDF is used.

446

447 **Peaking B_d background**

448 Decays of B_d mesons into the $D_s h\pi\pi$ final state are described by the B_s signal PDF
449 where the mean is shifted by the known mass difference $m_{B_s} - m_{B_d}$ [15].

450

451 **Partially reconstructed background**

452 Partially reconstructed $B_s^0 \rightarrow D_s^* \pi\pi\pi$ decays, with $D_s^* \rightarrow D_s \gamma$ or $D_s^* \rightarrow D_s \pi^0$, are expected
453 to be peaking lower than signal in the $m(D_s \pi\pi\pi)$ spectrum with large tails due to the
454 momentum carried away by the not reconstructed π^0 or γ . An empirical description for
455 the shape of this contribution is derived from a $B_s^0 \rightarrow D_s^* \pi\pi\pi$ MC sample subject to
456 the nominal $B_s^0 \rightarrow D_s \pi\pi\pi$ selection. Figure 5.2 (top) shows the respective reconstructed
457 $m(D_s \pi\pi\pi)$ distribution. A sum of three bifurcated Gaussian functions (*i.e.* Gaussian
458 functions with different widths on the left and the right side of the maximum value) is used
459 to describe it. In the fit to data, all parameters are fixed to the ones obtained from MC
460 except for the parameter which describes the width of the right tail of the distribution to
461 account for data-simulation differences in mass resolution. The equivalent $B_s^0 \rightarrow D_s^* K\pi\pi$
462 component contributing to the $B_s^0 \rightarrow D_s K\pi\pi$ data sample is described by the same PDF
463 with the right tail fixed to the $B_s^0 \rightarrow D_s \pi\pi\pi$ result.

464 Contributions from $B^0 \rightarrow D_s^* K\pi\pi$ decays are modeled with the $B_s^0 \rightarrow D_s^* K\pi\pi$ PDF
465 shifted by $m_{B_s^0} - m_{B^0}$.

466

467 **Misidentified background**

468 A small fraction of $B_s \rightarrow D_s^- \pi^+ \pi^+ \pi^-$ and $B_s^0 \rightarrow D_s^* \pi^+ \pi^+ \pi^-$ decays, where one of the
469 pions is misidentified as a kaon, contaminate the $B_s^0 \rightarrow D_s K^+ \pi^+ \pi^-$ sample. To determine
470 the corresponding background shapes, we use simulated events passing the nominal
471 selection except for the PID cuts on the bachelor π^+ tracks. The **PIDCalib** package
472 is used to determine the p_T, η -dependent $\pi^+ \rightarrow K^+$ misidentification probability for
473 each pion. We change the particle hypothesis from pion to kaon for the pion with the
474 higher misidentification probability and recompute the invariant B_s^0 mass, $m(D_s^- \pi_K^+ \pi^+ \pi^-)$.
475 Similarly, the invariant masses $m(\pi_K^+ \pi^+ \pi^-)$ and $m(\pi_K^+ \pi^-)$ are recomputed and required
476 to be within the considered phasespace region. The background distributions are shown
477 in Fig. 5.2 (middle, bottom) and modeled by the sum of three Crystal Ball functions.

478 The expected yield of misidentified $B_s^0 \rightarrow D_s\pi\pi\pi$ ($B_s^0 \rightarrow D_s^*\pi^+\pi^+\pi^-$) candidates in
 479 the $B_s^0 \rightarrow D_sK\pi\pi$ sample is computed by multiplying the fake rate (within the considered
 480 B_s mass range) of $0.63 \pm 0.01\%$ ($0.55 \pm 0.02\%$) for Run-I and $0.33 \pm 0.01\%$ ($0.24 \pm 0.01\%$)
 481 for Run-II by the $B_s^0 \rightarrow D_s\pi\pi\pi$ ($B_s^0 \rightarrow D_s^*\pi^+\pi^+\pi^-$) yield as determined in the mass
 482 fit to the $B_s^0 \rightarrow D_s\pi\pi\pi$ data sample. The yields are corrected for the $\text{PID}(\pi^+) < 0$
 483 requirement which has an efficiency of $77.1 \pm 0.1\%$ for Run-I and $81.0 \pm 0.1\%$ for Run-II
 484 data. The $B_s^0 \rightarrow D_s^*\pi^+\pi^+\pi^-$ yield is additionally corrected for the efficiency of the cut
 485 $m(D_sK\pi\pi) > 5200 \text{ MeV}$ evaluated on MC. In the fit to data, the misidentified background
 486 yields are fixed to the predicted ones.

487 We consider the $B_s^0 \rightarrow D_sK\pi\pi$ and $B_s^0 \rightarrow D_s^*K\pi\pi$ components contributing to the
 488 $B_s^0 \rightarrow D_s\pi\pi\pi$ data sample to be negligible due to the low branching fractions and the
 489 tight PID cuts on the bachelor pions.

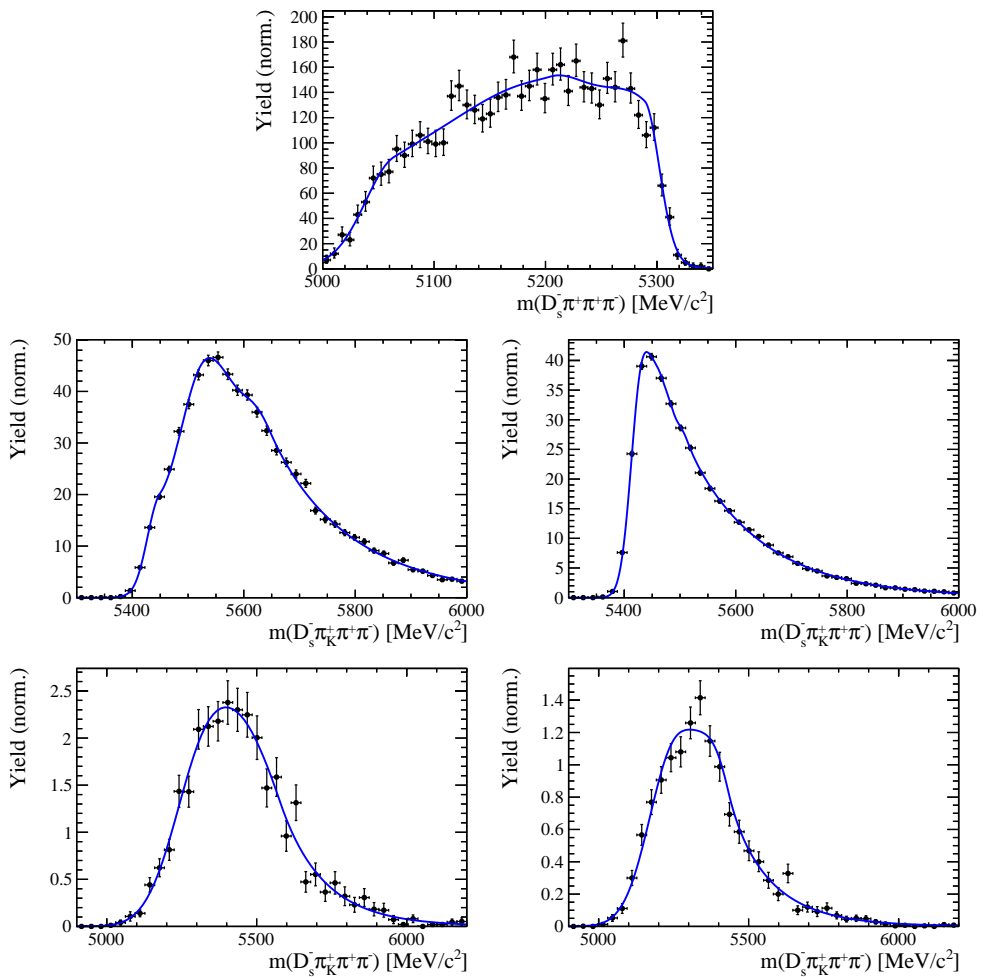


Figure 5.2: Top: Invariant mass distribution of simulated $B_s^0 \rightarrow D_s^*\pi\pi\pi$ events, where the γ/π^0 is excluded from the reconstruction. Middle: Invariant mass distribution of simulated $B_s^0 \rightarrow D_s\pi\pi\pi$ events for Run-I (left) and Run-II (right), where one of the pions is reconstructed as a kaon taking the misidentification probability into account. Bottom: Invariant mass distribution for simulated $B_s^0 \rightarrow D_s^*\pi\pi\pi$ events for Run-I (left) and Run-II (right), where the γ/π^0 from the D_s^* is excluded from reconstruction and one of the pions is reconstructed as a kaon taking the misidentification probability into account. The fitted PDFs are shown in blue.

490 5.3 Results

491 Figure 5.3 shows the invariant mass distribution for $B_s^0 \rightarrow D_s\pi\pi\pi$ and $B_s^0 \rightarrow D_sK\pi\pi$ can-
 492 didates passing all selection criteria. The projections for all categories of the simultaneous
 493 fit are shown in Appendix D. The integrated signal and background yields are listed in
 494 Tables 5.1 and 5.2.

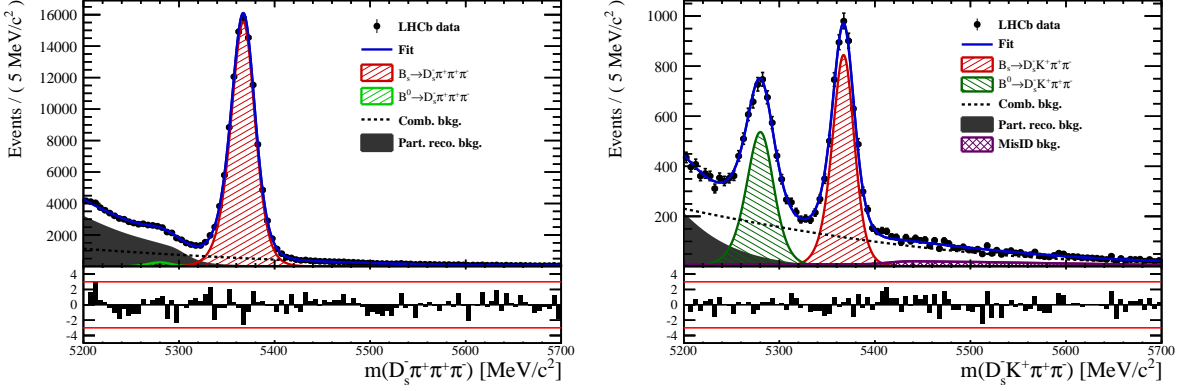


Figure 5.3: Invariant mass distribution of $B_s^0 \rightarrow D_s\pi\pi\pi$ (left) and $B_s^0 \rightarrow D_sK\pi\pi$ (right) candidates integrated over all categories.

Table 5.1: Total signal and background yields for the $B_s \rightarrow D_s\pi\pi\pi$ sample (left) and signal yield for the different D_s final states contributing to the $B_s \rightarrow D_s\pi\pi\pi$ sample (right).

Component	Yield
$B_s \rightarrow D_s\pi\pi\pi$	104176 ± 356
$B^0 \rightarrow D_s\pi\pi\pi$	1742 ± 363
Partially reconstructed bkg.	43157 ± 407
Combinatorial bkg.	40992 ± 455

D_s final state	Signal yield
$D_s^- \rightarrow \phi^0(1020)\pi^-$	35429 ± 202
$D_s^- \rightarrow K^{*0}(892)K^-$	29388 ± 194
$D_s^- \rightarrow (K^- h^+\pi^-)$	21695 ± 164
$D_s^- \rightarrow \pi^+\pi^-\pi^-$	17665 ± 148

Table 5.2: Total signal and background yields for the $B_s \rightarrow D_sK\pi\pi$ sample (left) and signal yield for the different D_s final states contributing to the $B_s \rightarrow D_sK\pi\pi$ sample (right).

Component	Yield
$B_s \rightarrow D_sK\pi\pi$	5172 ± 88
$B^0 \rightarrow D_sK\pi\pi$	4109 ± 100
Partially reconstructed bkg.	1825 ± 204
Misidentified bkg.	1186 ± 0
Combinatorial bkg.	9172 ± 221

D_s final state	Signal yield
$D_s^- \rightarrow \phi^0(1020)\pi^-$	1637 ± 47
$D_s^- \rightarrow K^{*0}(892)K^-$	1537 ± 47
$D_s^- \rightarrow (K^- h^+\pi^-)$	1134 ± 41
$D_s^- \rightarrow \pi^+\pi^-\pi^-$	864 ± 41

495 6 Decay-time Resolution

496 The observed oscillation of B mesons is prone to dilution, if the detector resolution is
 497 of similar magnitude as the oscillation period. In the B_s^0 system, considering that the
 498 measured oscillation frequency of the B_s^0 [28] and the average LHCb detector resolution [29]
 499 are both $\mathcal{O}(50 \text{ fs}^{-1})$, this is the case. Therefore, it is crucial to correctly describe the
 500 decay time resolution in order to avoid a bias on the measurement of time dependent CP
 501 violation. Since the time resolution depends on the particular event, especially the decay
 502 time itself, the sensitivity on γ can be significantly improved by using an event dependent
 503 resolution model rather than an average resolution. For this purpose, we use the per-event
 504 decay time error that is estimated based on the uncertainty obtained from the global
 505 kinematic fit of the momenta and vertex positions (DTF) with additional constraints on
 506 the PV position and the D_s mass. In order to apply it correctly, it has to be calibrated.
 507 The raw decay time error distributions for $B_s^0 \rightarrow D_s\pi\pi\pi$ signal candidates are shown in
 508 Figure 6.1 for Run-I and Run-II data. Significant deviations between the two different
 509 data taking periods are observed due to the increase in center of mass energy from Run-I
 510 to Run-II, as well as (among others) new tunings in the pattern and vertex reconstruction.
 511 The decay time error calibration is consequently performed separately for both data taking
 512 periods.

513 For Run-I data, we use the calibration from the closely related $B_s^0 \rightarrow D_s K$ analysis
 514 which was performed on a data sample of prompt- D_s candidates combined with a random
 515 pion track from the PV. We verify the portability to our decay channel on MC.

516 For Run-II data, a new lifetime unbiased stripping line (LTUB) has been implemented
 517 which selects prompt- D_s candidates combined with random $K\pi\pi$ tracks from the PV.

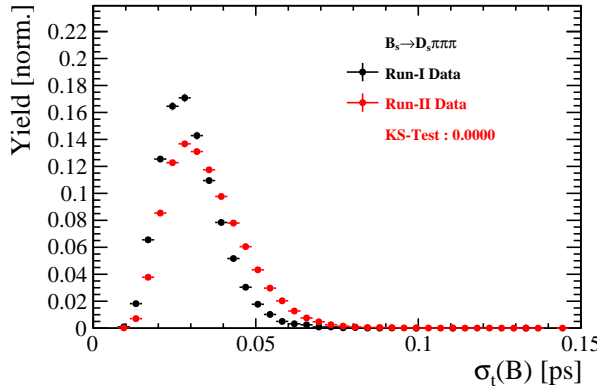


Figure 6.1: Distribution of the decay time error for $B_s^0 \rightarrow D_s\pi\pi\pi$ signal candidates for Run-I (black) and Run-II (red) data (sWeighted).

518 6.1 Calibration for Run-I data

519 For simulated $B_s^0 \rightarrow D_s K \pi\pi$ events, the spread of the differences between reconstructed
 520 decay time and true decay time, $\Delta t = t - t_{true}$, is a direct measure of the decay time
 521 resolution. The sum of two Gaussian pdfs with common mean but different widths is used
 522 to fit the distribution of the decay time difference Δt as shown in Fig. 6.2. The effective
 523 damping of the CP amplitudes due to the finite time resolution is described by the dilution
 524 \mathcal{D} . In the case of infinite precision, there would be no damping and therefore $\mathcal{D} = 1$ would
 525 hold, while for a resolution that is much larger than the B_s^0 oscillation frequency, \mathcal{D} would
 526 approach 0. For a double-Gaussian resolution model, the dilution is given by [7]

$$\mathcal{D} = f_1 e^{-\sigma_1^2 \Delta m_s^2 / 2} + (1 - f_1) e^{-\sigma_2^2 \Delta m_s^2 / 2}, \quad (6.1)$$

527 where σ_1 and σ_2 are the widths of the Gaussians, f_1 is the relative fraction of events
 528 described by the first Gaussian relative to the second and Δm_s is the oscillation frequency
 529 of B_s^0 mesons. An effective single Gaussian width is calculated from the dilution as,

$$\sigma_{eff} = \sqrt{(-2/\Delta m_s^2) \ln \mathcal{D}}, \quad (6.2)$$

530 which converts the resolution into a single-Gaussian function with an effective resolution
 531 that causes the same damping effect on the magnitude of the B_s oscillation. For the Run-I
 532 $B_s^0 \rightarrow D_s K \pi\pi$ MC sample the effective average resolution is found to be $\sigma_{eff} = 39.1 \pm 0.3$ fs.

533 To analyze the relation between the per-event decay time error σ_t and the actual
 534 resolution σ_{eff} , the simulated $B_s^0 \rightarrow D_s K \pi\pi$ sample is divided into equal-statistics slices
 535 of σ_t . For each slice, the effective resolution is determined as described above. Details of
 536 the fit results in each slice are shown in appendix E. Figure 6.2 shows the obtained values
 537 for σ_{eff} as a function of the per-event decay time error σ_t . To account for the variable
 538 binning, the bin values are not placed at the bin center but at the weighted mean of the
 539 respective per-event-error bin. A linear function is used to parametrize the distribution.
 540 The obtained values are

$$\sigma_{eff}^{MC}(\sigma_t) = (0.0 \pm 0.0) \text{ fs} + (1.232 \pm 0.010) \sigma_t \quad (6.3)$$

541 where the offset is fixed to 0. For comparison, the calibration function found for $B_s^0 \rightarrow D_s K$
 542 MC is also shown in Figure 6.2 [7]:

$$\sigma_{eff}^{D_s K, MC}(\sigma_t) = (0.0 \pm 0.0) \text{ fs} + (1.201 \pm 0.013) \sigma_t. \quad (6.4)$$

543 Due to the good agreement between the scale factors for $B_s^0 \rightarrow D_s K$ and $B_s^0 \rightarrow D_s K \pi\pi$
 544 MC, we conclude that the resolution calibration for $B_s^0 \rightarrow D_s K$ data [7]:

$$\sigma_{eff}^{D_s K}(\sigma_t) = (10.26 \pm 1.52) \text{ fs} + (1.280 \pm 0.042) \sigma_t \quad (6.5)$$

545 can be used for our analysis. The following calibration functions were used in the
 546 $B_s^0 \rightarrow D_s K$ analysis to estimate the systematic uncertainty on the decay-time resolution:

$$\sigma_{eff}^{D_s K}(\sigma_t) = (-0.568 \pm 1.570) \text{ fs} + (1.243 \pm 0.044) \sigma_t \quad (6.6)$$

$$\sigma_{eff}^{D_s K}(\sigma_t) = (0.0 \pm 0.0) \text{ fs} + (1.772 \pm 0.012) \sigma_t \quad (6.7)$$

548 It was also observed in this analysis that the scale factor is largely independent of the B_s
 549 kinematics and decay-time [6], consistent with other studies, for example in [30].

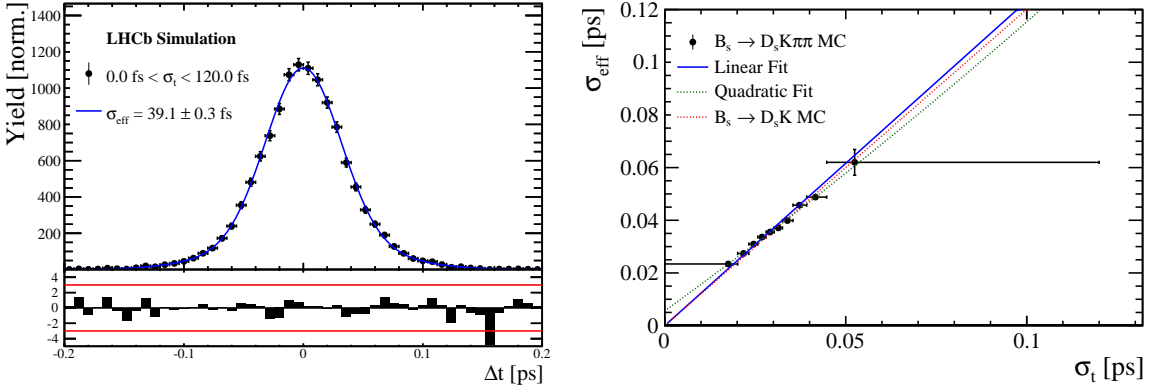


Figure 6.2: (Left) Difference of the true and measured decay time of $B_s^0 \rightarrow D_s K\pi\pi$ MC candidates. (Right) The measured resolution σ_{eff} as function of the per-event decay time error estimate σ_t for $B_s \rightarrow D_s K\pi\pi$ MC (Run-I). The fitted calibration curve is shown in blue.

550 6.2 Calibration for Run-II data

551 For the resolution calibration of Run-II data, a sample of promptly produced D_s candidates
 552 is selected using the B02DsKPiPiLTUBD2HHHBeauty2CharmLine stripping line. This
 553 lifetime-unbiased stripping line does not apply selection requirements related to lifetime
 554 or impact parameter, allowing for a study of the resolution. In order to reduce the rate
 555 of this sample it is pre-scaled in the stripping. Each D_s candidate is combined with a
 556 random kaon track and two random pion tracks which originate from the PV to obtain a
 557 sample of fake B_s candidates with a known true decay-time of $t_{\text{true}} = 0$. The difference of
 558 the measured decay time, t , of these candidates with respect to the true decay time is
 559 attributed to the decay time resolution.

560 The offline selection of the fake B_s candidates is summarized in Tab. 6.1. The selection
 561 is similar than the one for real data with the important difference that the D_s candidate
 562 is required to come from the PV by cutting on the impact parameter significance. Even
 563 after the full selection, a significant number of multiple candidates is observed. These
 564 are predominantly fake B_s candidates that share the same D_s candidate combined with
 565 different random tracks from the PV. We select one of these multiple candidates randomly
 566 which retains approximately 20% of the total candidates. As can be seen in Figure M.3,
 567 the shapes of the distributions of the unscaled decay time error σ_t for data taken in 2016
 568 and 2017 are significantly different. Therefore, the scaling of the decay time error is
 569 treated separately for 2015+2016 and 2017 data. The invariant mass distribution of the
 570 selected D_s candidates is shown in Fig. 6.3. To separate true D_s candidates from random
 571 combinations, the sPlot method is used to statistically subtract combinatorial background
 572 from the sample.

573 Figure 6.4 and 6.5 show the sWeighted decay-time distributions for fake B_s candidates
 574 from 2016 and 2017 data, respectively. Similar as in the previous section, the decay-time
 575 distribution is fitted with a double-Gaussian resolution model in slices of the per-event
 576 decay time error. Since some D_s candidates might actually originate from true B_s decays,
 577 the decay-time distribution of the fake B_s candidates might show a bias towards positive
 578 decay times. Therefore, we determine the decay-time resolution from the negative decay-
 579 time distribution only. Details of the fit results in each slice are shown in appendix E.

580 The resulting calibration functions are:

$$\sigma_{eff}^{Data,16}(\sigma_t) = (11.6 \pm 1.6) \text{ fs} + (0.877 \pm 0.040) \sigma_t \quad (6.8)$$

581

$$\sigma_{eff}^{Data,17}(\sigma_t) = (6.5 \pm 1.4) \text{ fs} + (0.961 \pm 0.036) \sigma_t \quad (6.9)$$

582 For 2016, the result is in good agreement with the one obtained for the $B_s \rightarrow J/\psi\phi$
583 (Run-II) analysis that uses 2016 data [31].

$$\sigma_{eff}^{J/\psi\phi}(\sigma_t) = (12.25 \pm 0.33) \text{ fs} + (0.8721 \pm 0.0080) \sigma_t \quad (6.10)$$

Table 6.1: Offline selection requirements for fake B_s candidates from promptly produced D_s candidates combined with random prompt $K\pi\pi$ bachelor tracks. The PID and veto cuts depending on the D_s final state and Dalitz plot position are the same as in Table. 4.1.

	Description	Requirement
$B_s \rightarrow D_s K\pi\pi$	χ_{vtx}^2/ndof	< 8
	χ_{DTF}^2/ndof	< 15
	t	< 0 ps
$D_s \rightarrow hh$	χ_{vtx}^2/ndof	< 5
	DIRA	> 0.99994
	χ_{FD}^2	> 9
	p_T	> 1800 MeV
	χ_{IP}^2	< 9
	$\chi_{IP}^2(h)$	> 5
Wrong PV veto	nPV = 1 min($\Delta\chi_{IP}^2$) > 20	
$X_s \rightarrow K\pi\pi$	$\chi_{IP}^2(h)$	< 40
	PIDK(K)	> 10
	PIDK(π)	< 5
	isMuon(h)	False
All tracks	p_T	> 500 MeV

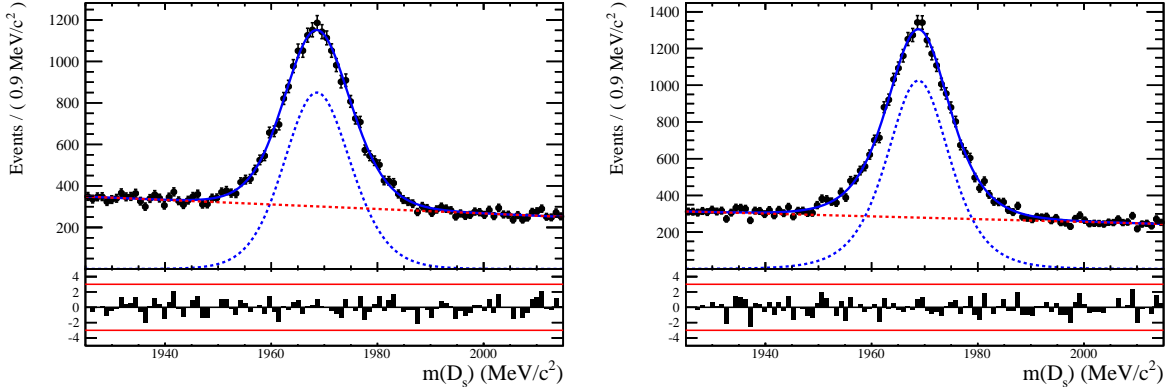


Figure 6.3: The invariant mass distribution for prompt D_s candidates for data taken from the LTUB stripping line in (left) 2016 and (right) 2017.

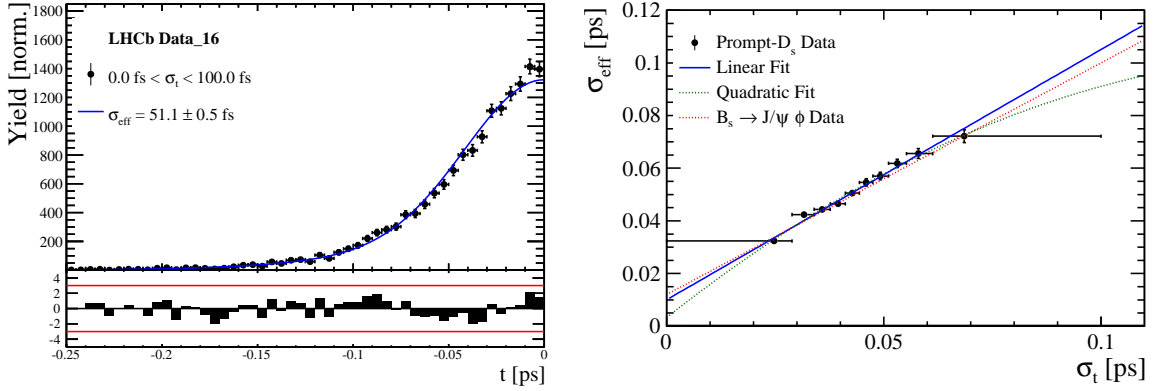


Figure 6.4: (Left) Decay-time distribution for fake B_s candidates from promptly produced D_s candidates, combined with random prompt $K\pi\pi$ bachelor tracks. (Right) The measured resolution σ_{eff} as function of the per-event decay time error estimate σ_t for fake B_s candidates (Run-II data). The fitted calibration curve is shown in blue. Data taken in 2016.

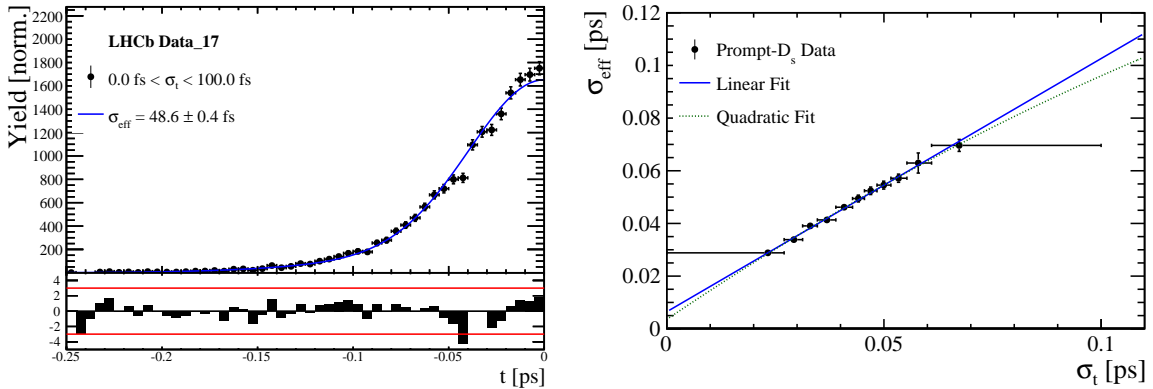


Figure 6.5: (Left) Decay-time distribution for fake B_s candidates from promptly produced D_s candidates, combined with random prompt $K\pi\pi$ bachelor tracks. (Right) The measured resolution σ_{eff} as function of the per-event decay time error estimate σ_t for fake B_s candidates (Run-II data). The fitted calibration curve is shown in blue. Data taken in 2017.

584 6.3 Decay-time bias

585 The analyses of $B_s \rightarrow J/\psi\phi$ [32] and $B_s \rightarrow D_s\pi$ [33] decays reported that the mean
 586 of the resolution model is not centered around zero for Run-II data. This decay-time
 587 bias is understood to be an effect of a misalignment between the VELO halves in the
 588 order of $8\text{ }\mu\text{m}$ in x -direction. To determine the decay-time bias from the prompt $D_s K\pi\pi$
 589 sample, the requirement $t < 0$ used for the calibration of the decay-time error estimate
 590 is removed. Since the decay-time bias shows a significant dependence on kinematic
 591 and geometric properties of the decay, the prompt sample is reweighted to match the
 592 three-dimensional $p_T(B_s)$, σ_t and $\chi^2_{FD}(D_s)$ distribution observed on $B_s \rightarrow D_s\pi\pi\pi$ signal
 593 data as shown in Fig. 6.6. An adaptive binning algorithm is used ensuring sufficient
 594 statistics in each bin. The decay-time bias is extracted from a fit to the (reweighted)
 595 decay-time distribution of the prompt candidates shown in Fig. 6.7. A systematic error is
 596 estimated by utilizing different reweighting schemes: a 2D reweighting in $p_T(B_s)$, σ_t ; three
 597 consecutive 1D reweightings in $p_T(B_s)$, σ_t and $\chi^2_{FD}(D_s)$; an additional 1D reweighting
 598 in $\eta(B_s)$ after the nominal 3D weighting; two 2D weightings in $(p_T(B_s), \eta(B_s))$ and
 599 $(\sigma_t, \chi^2_{FD}(D_s))$. Additionally, a fit is performed which includes an exponential decay-time
 600 distribution to account for a potential long-lived background component from true B
 601 decays and the fit range is adjusted from $[-0.25, 0.25]$ ps to $[-0.2, 0.05]$ ps. The largest
 602 deviation from the nominal result is assigned as systematic.

603 The procedure is validated using simulated $B_s \rightarrow D_s\pi$ signal and prompt $D_s\pi$ samples,
 604 which are processed including a realistic VELO misalignment (as observed for data). As
 605 shown in Fig. 6.8, the decay-time biases extracted from the two samples differ significantly
 606 before the reweighting and are in a good agreement afterwards.

607 It was further observed that the offline selection, in particular the requirement on
 608 the D_s flight distance significance, introduces an additional decay-time bias of the order
 609 -1 fs for signal decays, while prompt candidates are not affected. The decay-time bias
 610 originating from the candidate selection is thus determined from the $B_s \rightarrow D_s\pi\pi\pi$ MC
 611 sample, see Fig. 6.9. Identical results are obtained with the $B_s \rightarrow D_s K\pi\pi$ MC sample.

612 Table 6.2 summarizes the decay-time biases due to the selection and VELO misalign-
 613 ment as well as the combined decay-time bias to be used in the resolution model for
 614 different data-taking periods. It is verified on the $B_s^0 \rightarrow D_s\pi$ MC sample (with VELO
 615 misalignment) that the decay-time biases of these two sources add linearly.

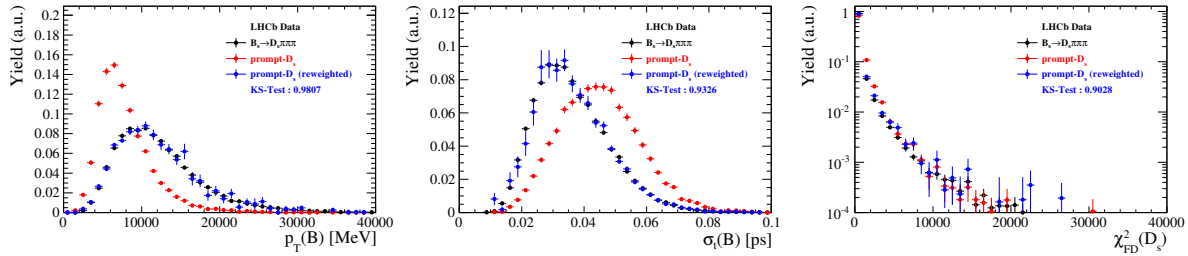


Figure 6.6: Comparison of selected variables for $B_s \rightarrow D_s\pi\pi\pi$ signal data (black) and prompt $D_s K\pi\pi$ data before (red) and after (blue) reweighting.

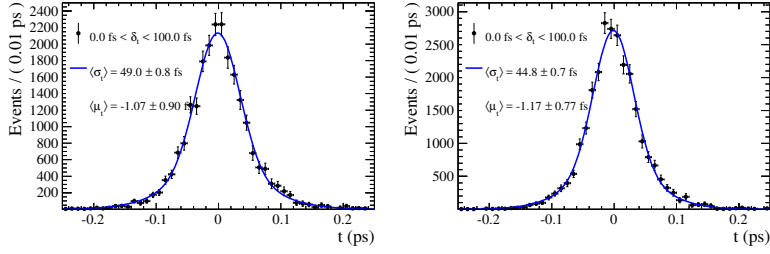


Figure 6.7: Reweighted decay-time distribution for fake B_s candidates from promptly produced D_s candidates, combined with random prompt $K\pi\pi$ bachelor tracks for 2016 (left) and 2017 (right) data.

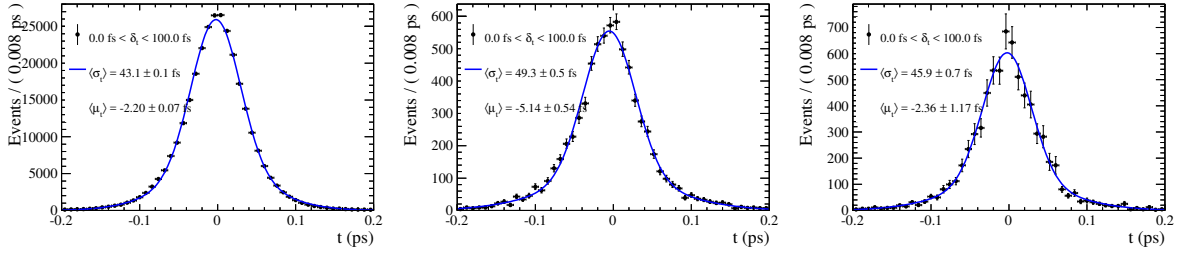


Figure 6.8: Difference of the true and measured decay time of $B_s^0 \rightarrow D_s\pi$ MC candidates processed with a realistic VELO misalignment (left). Decay-time distribution of prompt $D_s\pi$ MC candidates processed with a realistic VELO misalignment before (middle) and after (right) reweighting.

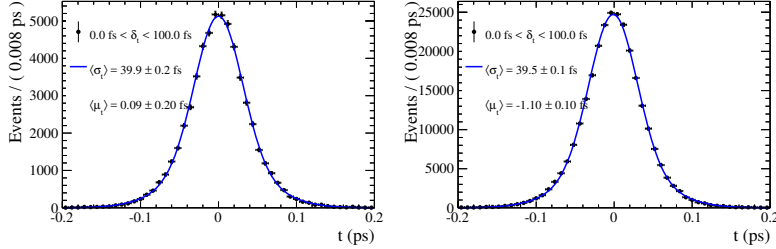


Figure 6.9: Difference of the true and measured decay time of $B_s^0 \rightarrow D_s\pi\pi\pi$ MC (Run-II) candidates after passing the stripping and trigger selection (left) and after full selection (right).

Table 6.2: Decay-time biases due to the selection and VELO misalignment as well as the total decay-time bias used in the resolution model.

	Decay-time bias [fs]		
	Selection	Alignment	Total
Run-1	-1.20 ± 0.11	-	-1.20 ± 0.11
15/16	-1.10 ± 0.10	$-1.07 \pm 0.90 \pm 1.30$	-2.17 ± 1.68
17	-1.10 ± 0.10	$-1.17 \pm 0.77 \pm 1.58$	-2.27 ± 1.78

616 7 Acceptance

617 7.1 MC corrections

618 7.1.1 Truth matching of simulated candidates

619 We use the `BackgroundCategory` tool to truth match our simulated candidates. Candidates
 620 with background category (`BKGCAT`) 20 or 50 are considered to be true signal. Background
 621 category 60 is more peculiar since it contains both badly reconstructed signal candidates
 622 and ghost background. This is due to the fact that the classification algorithms identifies
 623 all tracks for which less than 70% of the reconstructed hits are matched to generated
 624 truth-level quantities as ghosts. In particular for signal decays involving many tracks (as
 625 in our case), this arbitrary cutoff is not 100% efficient. Moreover, the efficiency is expected
 626 to depend on the kinematics which would lead to a biased acceptance determination if
 627 candidates with `BKGCAT`= 60 would be removed. We therefore include `BKGCAT`= 60 and
 628 statistically subtract the ghost background by using the `sPlot` technique. The `sWeights`
 629 are calculated from a fit to the reconstructed B_s mass. The signal contribution is modeled
 630 as described in Sec. 5.1 and the background with a polynomial. The fit is performed
 631 simultaneously in two categories; the first includes events with `BKGCAT` = 20 or 50 and
 632 the second events with `BKGCAT` = 60. To account for the different mass resolution we
 633 use a different σ for each category, while the mean and the tail parameters are shared
 634 between them. The background component is only included for the second category.

635 A significant fraction of 7% of the true signal candidates are classified as ghosts, while
 636 only 20% of the events classified with `BKGCAT`= 60 are indeed genuine ghosts.

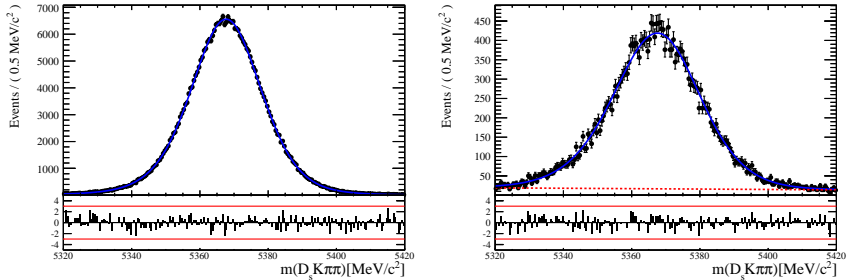


Figure 7.1: The reconstructed B_s mass distribution for simulated $B_s \rightarrow D_s K\pi\pi$ decays classified with `BKGCAT` = 20 or 50 (left) and `BKGCAT` = 60 (right) after the full selection.

637 7.1.2 Correction of data-simulation differences

638 For the evaluation of phase space efficiency and to a lesser extend also the decay-time
 639 efficiency we rely on simulated data as discussed in the following sections. A number
 640 of data-driven corrections are applied to the MC samples to account for known data-
 641 simulation differences. The MC sample is reweighted to match the three-dimensional
 642 p_T , η and track multiplicity distribution observed on real data. These corrections are
 643 derived from the calibration channel $B_s \rightarrow D_s \pi\pi\pi$ and applied to both the signal and
 644 calibration channel MC samples. The distributions before and after reweighting are shown
 645 in Appendix L. We use the `PIDCorr` tool to correct the simulated PID responses based on
 646 PID calibration samples [34].

647 7.2 Decay-time acceptance

648 The decay-time distribution of the B_s^0 mesons is sculpted due to the geometry of the LHCb
 649 detector and the applied selection cuts, which are described in Section 4. In particular, any
 650 requirement on the flight distance, the impact parameter or the direction angle (DIRA)
 651 of the B_s^0 mesons, as well as the direct cut on the proper-time, will lead to a decay-time
 652 dependent efficiency $\epsilon(t)$.

653 We use a combination of control channels to derive the acceptance function $\epsilon(t)$,
 654 because for $B_s^0 \rightarrow D_s K\pi\pi$ decays the decay-time acceptance is strongly correlated with
 655 the CP -observables which we aim to measure. Therefore, extracting the CP -observables
 656 and the acceptance shape at the same time is not possible. A fit to the decay-time
 657 distribution of $B_s^0 \rightarrow D_s \pi\pi\pi$ candidates is performed and the obtained acceptance shape
 658 is corrected for the small difference observed between the $B_s^0 \rightarrow D_s K\pi\pi$ and $B_s^0 \rightarrow D_s \pi\pi\pi$
 659 MC samples. In addition, we include the control channel $B^0 \rightarrow D_s K\pi\pi$ to increase
 660 the statistical precision. A simultaneous fit to the four datasets ($B_s^0 \rightarrow D_s \pi\pi\pi$ data,
 661 $B^0 \rightarrow D_s K\pi\pi$ data, $B_s^0 \rightarrow D_s K\pi\pi$ MC and $B_s^0 \rightarrow D_s \pi\pi\pi$ MC) is performed to allow for
 662 a straightforward propagation of uncertainties. In each case, a PDF of the following form

$$663 \quad \mathcal{P}(t, \sigma_t) = \left[e^{-\Gamma t} \cdot \cosh\left(\frac{\Delta\Gamma t'}{2}\right) \otimes \mathcal{R}(t - t', \sigma_t) \right] \cdot \epsilon(t), \quad (7.1)$$

663 is used to describe the decay-time distribution. For real data, the values for $\Gamma_{s,d}$ and
 664 $\Delta\Gamma_{s,d}$ are fixed to the latest HFLAV results [35], while for simulated data, the generated
 665 values are used. A single Gaussian resolution function $\mathcal{R}(t - t', \sigma_t)$ is used where the
 666 decay-time error estimate is scaled with the respective calibration functions determined in
 667 Sec. 6. Each decay-time acceptance $\epsilon(t)$ is modeled using cubic splines, allowing for the
 668 analytical computation of the decay-time integrals appearing in the PDF [36]. The splines
 669 are parametrized by so-called knots (t_0, t_1, \dots, t_N) which determine their boundaries. Two
 670 knots are located by default at the lower and upper edge of the interval allowed for the
 671 decay time, the remaining ones are chosen such that there is an approximately equal
 672 amount of data in-between two consecutive knots. In the basis of cubic b-splines, $b_i(t)$,
 673 the acceptance is then constructed as:

$$674 \quad \epsilon(t) = \sum_{i=0}^N v_i b_i(t) \quad (7.2)$$

674 where the spline coefficients v_i are determined from the fit. We fix coefficient v_{N-1} to unity
 675 in order to normalize the overall acceptance function. To stabilize the upper decay-time
 676 acceptance, v_N is fixed by a linear extrapolation from the two previous coefficients:

$$677 \quad v_N = v_{N-1} + \frac{v_{N-2} - v_{N-1}}{t_{N-2} - t_{N-1}} \cdot (t_N - t_{N-1}). \quad (7.3)$$

677 It was found that at least $N = 6$ knots are necessary for a sufficient fit quality.

678 Three distinct splines are used in the following combinations to describe the acceptances
 679 for the four datasets:

- 680 • $B_s^0 \rightarrow D_s K\pi\pi$ MC: $\epsilon_{D_s K\pi\pi}^{MC}(t)$
- 681 • $B_s^0 \rightarrow D_s \pi\pi\pi$ MC: $\epsilon_{D_s \pi\pi\pi}^{MC}(t) = R(t) \cdot \epsilon_{D_s K\pi\pi}^{MC}(t)$
- 682 • $B_s^0 \rightarrow D_s \pi\pi\pi$ data: $\epsilon_{D_s \pi\pi\pi}^{Data}(t) = R(t) \cdot \epsilon_{D_s K\pi\pi}^{Data}(t)$
- 683 • $B^0 \rightarrow D_s K\pi\pi$ data: $\epsilon_{D_s K\pi\pi}^{Data}(t)$

684 where $\epsilon_{D_s K\pi\pi}^{MC}(t)$ represents the acceptance in $B_s^0 \rightarrow D_s K\pi\pi$ MC, $R(t)$ represents the
 685 ratio of acceptances in $B_s^0 \rightarrow D_s \pi\pi\pi$ and $B_s^0 \rightarrow D_s K\pi\pi$ MC and the final acceptance in
 686 $B_s^0 \rightarrow D_s K\pi\pi$ data is represented by $\epsilon_{D_s K\pi\pi}^{Data}(t)$.

687 The acceptances are determined separately for each data-taking period and each trigger
 688 category as discussed in more detail in Appendix F. The fit results are shown in Figs. 7.2
 689 to 7.5 and the fitted parameters are summarized in Tables 7.1 to 7.4.

Table 7.1: Time acceptance parameters for events in category [Run-I,L0-TOS].

Knot position	Coefficient	$B_s^0 \rightarrow D_s K\pi\pi$ data	$B_s^0 \rightarrow D_s K\pi\pi$ MC	Ratio
0.4	v_0	0.309 ± 0.018	0.410 ± 0.007	1.007 ± 0.029
0.5	v_1	0.694 ± 0.031	0.776 ± 0.011	0.936 ± 0.021
1.4	v_2	0.858 ± 0.043	0.896 ± 0.015	1.004 ± 0.024
2.5	v_3	1.090 ± 0.028	1.099 ± 0.009	0.992 ± 0.015
6.5	v_4	1.0 (fixed)	1.0 (fixed)	1.0 (fixed)
10.0	v_5	0.921 (interpolated)	0.913 (interpolated)	1.007 (interpolated)

Table 7.2: Time acceptance parameters for events in category [Run-I,L0-TIS].

Knot position	Coefficient	$B_s^0 \rightarrow D_s K\pi\pi$ data	$B_s^0 \rightarrow D_s K\pi\pi$ MC	Ratio
0.4	v_0	0.158 ± 0.014	0.216 ± 0.005	0.986 ± 0.040
0.5	v_1	0.422 ± 0.029	0.524 ± 0.010	0.965 ± 0.029
1.4	v_2	0.802 ± 0.047	0.860 ± 0.017	0.982 ± 0.029
2.5	v_3	1.099 ± 0.034	1.098 ± 0.011	1.002 ± 0.019
6.5	v_4	1.0 (fixed)	1.0 (fixed)	1.0 (fixed)
10.0	v_5	0.913 (interpolated)	0.914 (interpolated)	0.998 (interpolated)

Table 7.3: Time acceptance parameters for events in category [Run-II,L0-TOS].

Knot position	Coefficient	$B_s^0 \rightarrow D_s K\pi\pi$ data	$B_s^0 \rightarrow D_s K\pi\pi$ MC	Ratio
0.4	v_0	0.285 ± 0.009	0.368 ± 0.005	1.023 ± 0.020
0.5	v_1	0.663 ± 0.017	0.749 ± 0.009	0.911 ± 0.016
1.4	v_2	0.856 ± 0.025	0.893 ± 0.012	1.016 ± 0.019
2.5	v_3	1.060 ± 0.017	1.071 ± 0.008	0.996 ± 0.013
6.5	v_4	1.0 (fixed)	1.0 (fixed)	1.0 (fixed)
10.0	v_5	0.948 (interpolated)	0.938 (interpolated)	1.004 (interpolated)

Table 7.4: Time acceptance parameters for events in category [Run-II,L0-TIS].

Knot position	Coefficient	$B_s^0 \rightarrow D_s K\pi\pi$ data	$B_s^0 \rightarrow D_s K\pi\pi$ MC	Ratio
0.4	v_0	0.117 ± 0.008	0.171 ± 0.003	0.965 ± 0.034
0.5	v_1	0.422 ± 0.019	0.474 ± 0.008	0.952 ± 0.024
1.4	v_2	0.733 ± 0.027	0.777 ± 0.013	0.973 ± 0.025
2.5	v_3	1.071 ± 0.020	1.046 ± 0.010	0.989 ± 0.015
6.5	v_4	1.0 (fixed)	1.0 (fixed)	1.0 (fixed)
10.0	v_5	0.938 (interpolated)	0.959 (interpolated)	1.009 (interpolated)

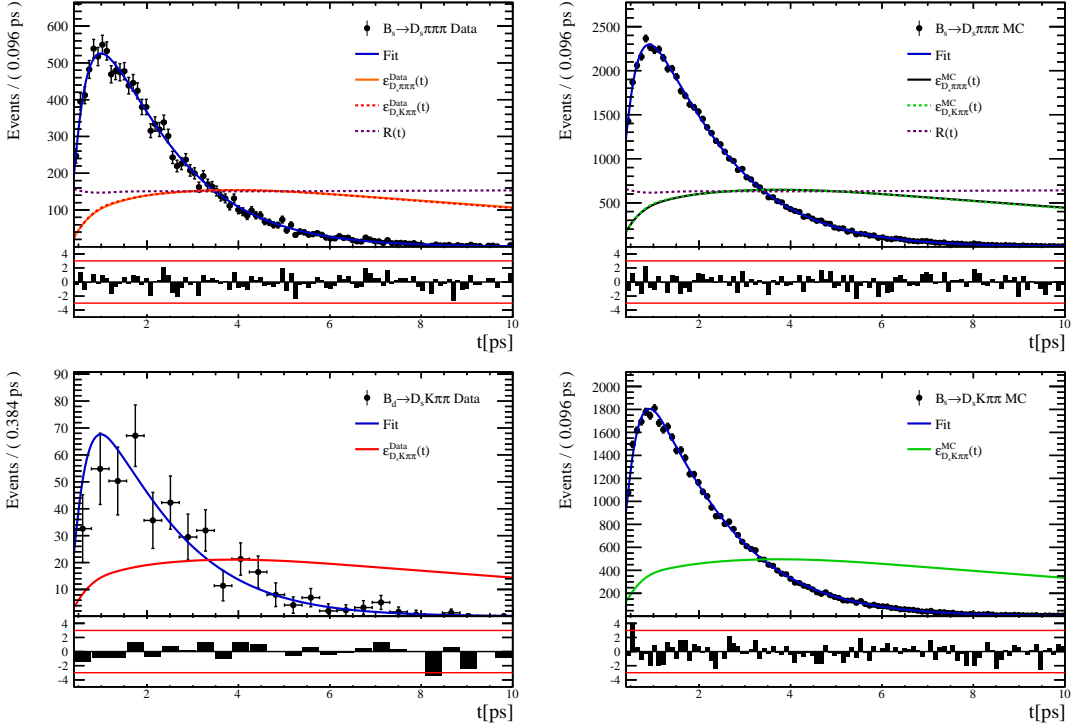


Figure 7.2: Decay-time fit projections for $B_s^0 \rightarrow D_s \pi\pi\pi$ data (top-left), $B_s^0 \rightarrow D_s \pi\pi\pi$ MC (top-right), $B^0 \rightarrow D_s K\pi\pi$ data (bottom-left) and $B_s^0 \rightarrow D_s K\pi\pi$ MC (bottom-right) in category [Run-I,L0-TOS]. The respective acceptance function is overlaid in an arbitrary scale.

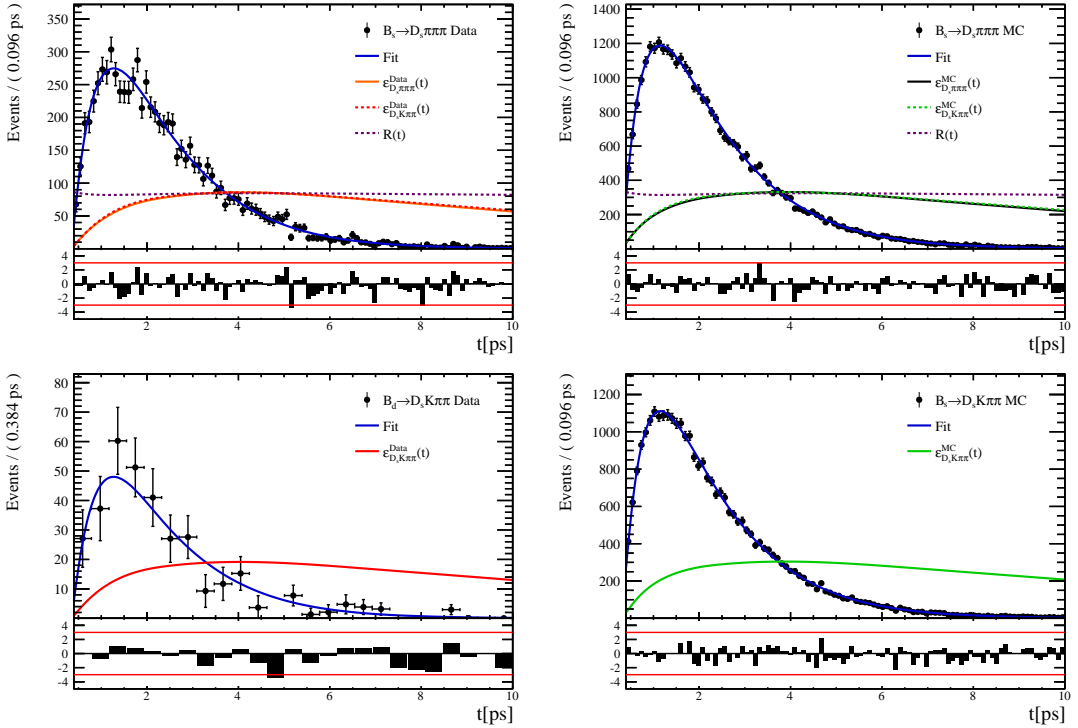


Figure 7.3: Decay-time fit projections for $B_s^0 \rightarrow D_s \pi\pi\pi$ data (top-left), $B_s^0 \rightarrow D_s \pi\pi\pi$ MC (top-right), $B^0 \rightarrow D_s K\pi\pi$ data (bottom-left) and $B_s^0 \rightarrow D_s K\pi\pi$ MC (bottom-right) in category [Run-I,L0-TIS]. The respective acceptance function is overlaid in an arbitrary scale.

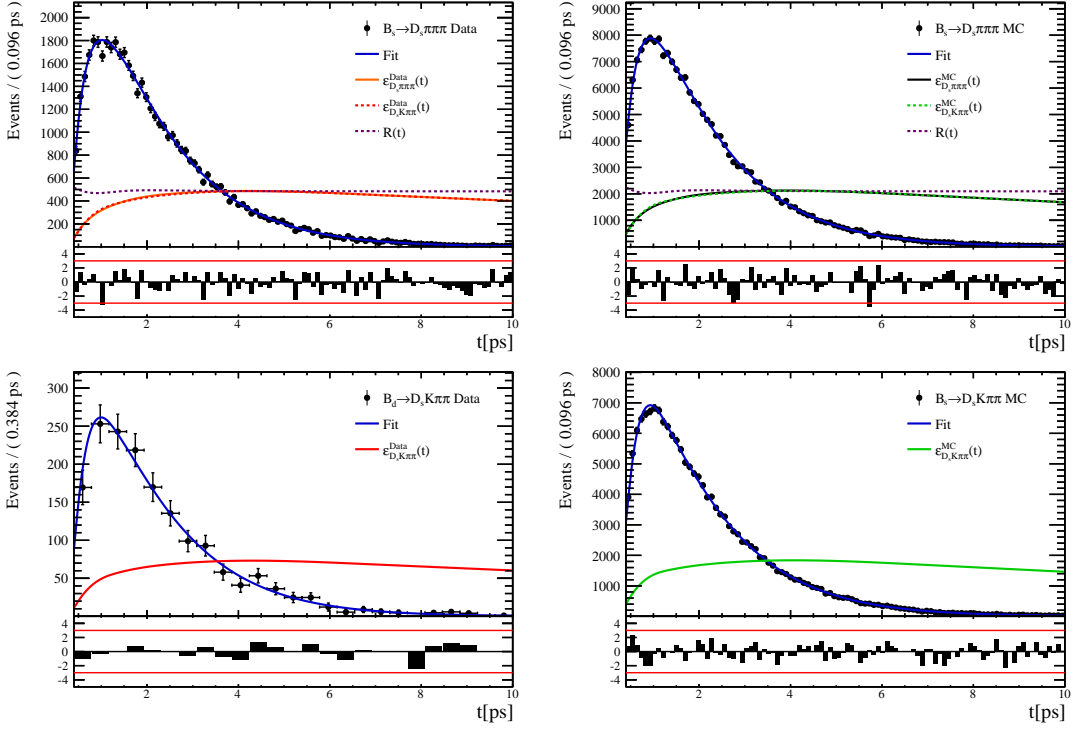


Figure 7.4: Decay-time fit projections for $B_s^0 \rightarrow D_s \pi\pi\pi$ data (top-left), $B_s^0 \rightarrow D_s \pi\pi\pi$ MC (top-right), $B_s^0 \rightarrow D_s K\pi\pi$ data (bottom-left) and $B_s^0 \rightarrow D_s K\pi\pi$ MC (bottom-right) in category [Run-II,L0-TOS]. The respective acceptance function is overlaid in an arbitrary scale.

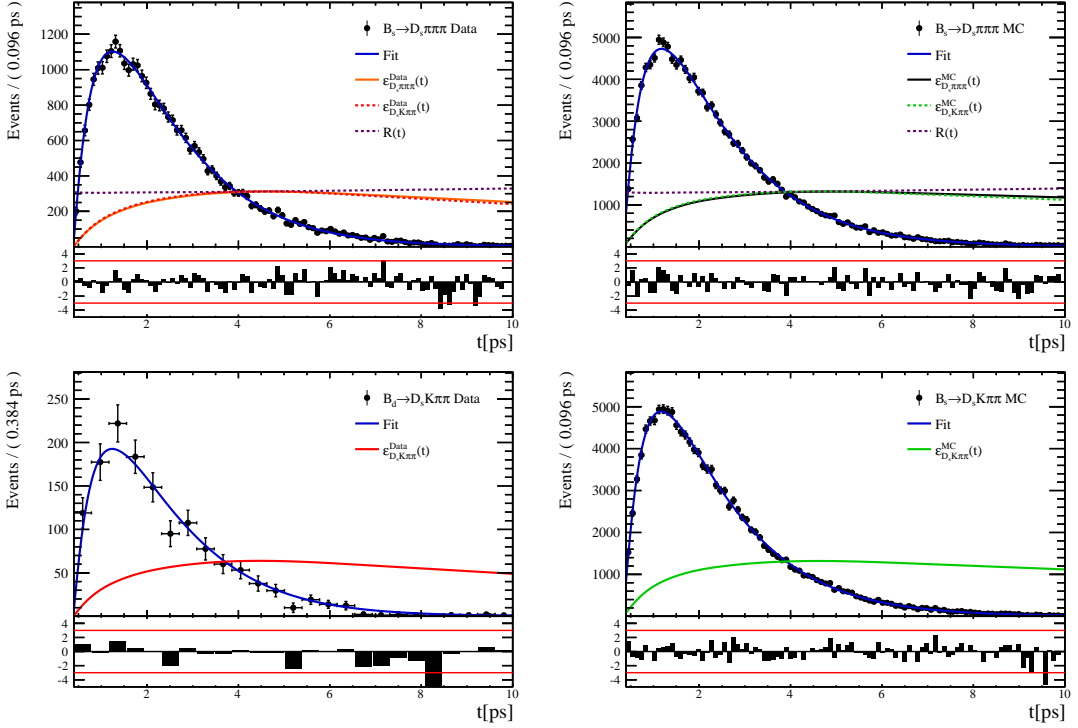


Figure 7.5: Decay-time fit projections for $B_s^0 \rightarrow D_s \pi\pi\pi$ data (top-left), $B_s^0 \rightarrow D_s \pi\pi\pi$ MC (top-right), $B_s^0 \rightarrow D_s K\pi\pi$ data (bottom-left) and $B_s^0 \rightarrow D_s K\pi\pi$ MC (bottom-right) in category [Run-II,L0-TIS]. The respective acceptance function is overlaid in an arbitrary scale.

690 7.3 Phase space acceptance

691 The signal PDF used for the full time-dependent amplitude fit can be written in terms of
 692 the differential decay rate from Equation 2.28 as

$$\mathcal{P}(\mathbf{x}, t, g, f) = \frac{\left(\frac{d\Gamma(\mathbf{x}, t, q, f)}{dt d\Phi_4} \right) \cdot \epsilon(\mathbf{x}) \cdot \epsilon(t)}{\int \sum_{q,f} \left(\frac{d\Gamma(\mathbf{x}, t, q, f)}{dt d\Phi_4} \right) \cdot \epsilon(\mathbf{x}) \cdot \epsilon(t) dt d\Phi_4} \quad (7.4)$$

693 where $\epsilon(\mathbf{x})$ is the phase-space efficiency. Note that the efficiency in the numerator appears
 694 as an additive constant in the log \mathcal{L} that does not depend on any fit parameters such that it
 695 can be ignored. However, the efficiency function still enters via the normalization integrals.
 696 In contrast to the time integrals which can be performed analytically as discussed in
 697 Sec. 7.2, the phase-space integrals are determined numerically. For this purpose, we use
 698 simulated events generated with **EVTGEN**, pass them through the full detector simulation
 699 and apply the same selection criteria as for data in order to perform the MC integrals. As
 700 an example, the integral of the total $b \rightarrow c$ amplitude squared can be approximated as

$$\int |\mathcal{A}_f^c(\mathbf{x})|^2 \epsilon(\mathbf{x}) d\Phi_4 \approx \frac{1}{N_{MC}} \sum_k^{N_{MC}} \frac{|\mathcal{A}_f^c(\mathbf{x}_k)|^2}{|A'(\mathbf{x}_k)|^2} \quad (7.5)$$

701 where A' labels the amplitude model used for the generation and x_k is the k -th MC
 702 event. As a result, the phase-space efficiency can be included in the fit without explicitly
 703 modeling it. The size of the fully selected MC sample ($N_{MC} = 380k$) is more than 70 times
 704 larger as the data sample which results in an integral precision smaller than 0.2%. The
 705 efficiency projections are shown in Fig. 7.6 for visualization purposes only. As discussed
 706 in Appendix G, the phase space efficiency differs significantly among L0-trigger categories
 707 while the differences are small between the data-taking periods and negligible between
 708 the D_s final states. To account for this, the MC events are scaled such that the relative
 709 proportions of the four categories [Run-I,L0-TOS], [Run-I,L0-TIS], [Run-II,L0-TOS] and
 710 [Run-II,L0-TIS] are the same as observed on the $B_s \rightarrow D_s K\pi\pi$ data sample.

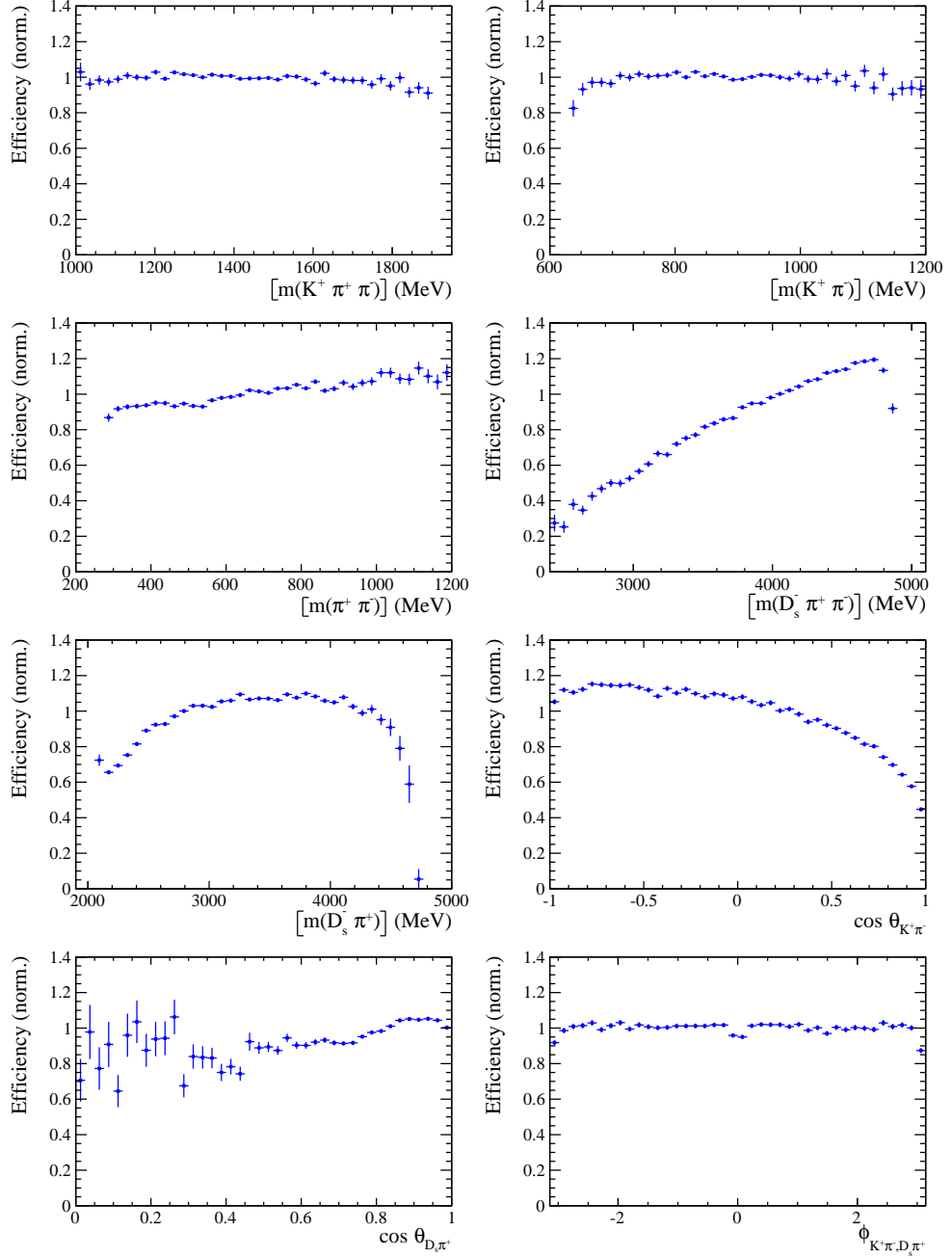


Figure 7.6: Efficiency variation as a function of the phase-space variables obtained from the ratio of selected and generated MC events.

711 8 Flavour Tagging

712 To identify the initial flavour state of the B_s^0 meson, a number of flavour tagging algorithms
 713 are used that either determine the flavour of the non-signal b-hadron produced in the
 714 event (opposite site, OS [37]) or use particles produced in the fragmentation of the signal
 715 candidate B_s^0/\bar{B}_s^0 (same side, SS [38]). For the same side, the algorithm searching for the
 716 charge of an additional kaon that accompanies the fragmentation of the signal candidate is
 717 used (SS-Kaon). For the opposite site, five different taggers are chosen: the algorithms that
 718 use the charge of an electron or a muon from semi-leptonic B decays (OS- e,μ), the tagger
 719 that uses the charge of a kaon from a $b \rightarrow c \rightarrow s$ decay chain (OS-Kaon), the algorithm
 720 which reconstructs opposite-side charm hadrons from a number of decay channels (OS-c)
 721 and the algorithm that determines the B_s^0/\bar{B}_s^0 candidate flavour from the charge of a
 722 secondary vertex, reconstructed from the OS b decay product (OS-VtxCharge).

723 Every tagging algorithm is prone to misidentify the signal candidate at a certain
 724 mistag rate ω . This might be caused by particle misidentification, flavour oscillation
 725 of the neutral opposite site B-meson or by tracks that are wrongly picked up from the
 726 underlying event. An imperfect determination of the B_s^0 production flavor dilutes the
 727 observed CP asymmetry by a factor $D_{tag} = 1 - 2\omega$. This means that the statistical
 728 precision, with which the CP asymmetry can be measured, scales as the inverse square
 729 root of the effective tagging efficiency:

$$\epsilon_{eff} = \epsilon_{tag}(1 - 2\omega)^2, \quad (8.1)$$

730 where ϵ_{tag} is the fraction of tagged candidates.

731 For each B_s^0/\bar{B}_s^0 candidate, the tagging algorithms provide, besides a flavour tag
 732 $q = 1, -1, 0$ (for an initial B_s^0 , \bar{B}_s^0 or no tag), a prediction for the mistag probability η
 733 based on the output of multivariate classifiers. These are trained on either simulated or
 734 **sWeighted** samples of flavour specific control channels ($B_s^0 \rightarrow D_s^- \pi^+$ (SS algorithm) and
 735 $B^+ \rightarrow J/\psi K^+$ (OS algorithms)) and are optimized for highest ϵ_{eff} on data. Utilizing
 736 flavour-specific final states, the estimated mistag η of each tagger has to be calibrated to
 737 match the actual mistag probability ω . For the calibration, a linear model

$$\omega(\eta) = p_0 + p_1 \cdot (\eta - \langle \eta \rangle), \quad (8.2)$$

738 is used where $\langle \eta \rangle$ is the average estimated mistag probability. A perfectly calibrated
 739 tagger would lead to $\omega(\eta) = \eta$ and one would expect $p_1 = 1$ and $p_0 = \langle \eta \rangle$. Due to the
 740 different interaction cross-sections of oppositely charged particles, the tagging calibration
 741 parameters depend on the initial state flavour of the B_s^0 . Therefore, the flavour asymmetry
 742 parameters Δp_0 , Δp_1 and $\Delta \epsilon_{tag}$ are introduced.

743 8.1 OS tagger combination

744 First, the OS electron, muon, kaon, charm and the secondary vertex charge taggers are
 745 individually calibrated and then combined into a single OS-Combo tagger using the
 746 **EspressoPerformanceMonitor** tool. We choose the flavour specific decay $B_s \rightarrow D_s \pi\pi\pi$ as
 747 calibration mode since it is very similar to the signal decay $B_s \rightarrow D_s K\pi\pi$. The calibration
 748 is performed separately for Run-I and Run-II data. The OS-c tagger is not included for
 749 Run-I data since the statistics is too low. Where available the latest Run-II tuning is used
 750 for Run-II data, otherwise the Run-I tuning of the taggers is used. The calibration sample
 751 is split in two subsamples. The single tagger calibration is performed for each and then
 752 applied to the other sample. Figures 8.1 and 8.2 show the fitted calibration functions
 753 and Tables 8.1 and 8.2 list the measured tagging performances (for both subsamples
 754 combined). The tagging calibration parameters are listed in Appendix H.

Table 8.1: The flavour tagging performances for the used OS taggers for Run-I data.

Tagger	ϵ	ω	$\epsilon \langle D^2 \rangle = \epsilon (1 - 2\omega)^2$
OS μ	$(8.713 \pm 0.206)\%$	$(28.893 \pm 0.180(\text{stat}) \pm 2.291(\text{cal}))\%$	$(1.553 \pm 0.045(\text{stat}) \pm 0.337(\text{cal}))\%$
OS e	$(3.201 \pm 0.129)\%$	$(28.792 \pm 0.363(\text{stat}) \pm 3.611(\text{cal}))\%$	$(0.576 \pm 0.030(\text{stat}) \pm 0.196(\text{cal}))\%$
OS K	$(32.230 \pm 0.342)\%$	$(38.451 \pm 0.093(\text{stat}) \pm 1.145(\text{cal}))\%$	$(1.719 \pm 0.033(\text{stat}) \pm 0.341(\text{cal}))\%$
Vertex Charge	$(21.855 \pm 0.302)\%$	$(35.712 \pm 0.091(\text{stat}) \pm 1.474(\text{cal}))\%$	$(1.785 \pm 0.033(\text{stat}) \pm 0.368(\text{cal}))\%$

Table 8.2: The flavour tagging performances for the used OS taggers for Run-II data.

Tagger	ϵ	ω	$\epsilon \langle D^2 \rangle = \epsilon (1 - 2\omega)^2$
OS μ	$(9.664 \pm 0.151)\%$	$(30.911 \pm 0.115(\text{stat}) \pm 1.369(\text{cal}))\%$	$(1.409 \pm 0.028(\text{stat}) \pm 0.202(\text{cal}))\%$
OS e	$(4.590 \pm 0.107)\%$	$(33.577 \pm 0.140(\text{stat}) \pm 2.007(\text{cal}))\%$	$(0.495 \pm 0.014(\text{stat}) \pm 0.121(\text{cal}))\%$
OS K	$(20.185 \pm 0.205)\%$	$(36.918 \pm 0.071(\text{stat}) \pm 0.969(\text{cal}))\%$	$(1.382 \pm 0.021(\text{stat}) \pm 0.205(\text{cal}))\%$
Vertex Charge	$(20.597 \pm 0.207)\%$	$(34.751 \pm 0.075(\text{stat}) \pm 0.961(\text{cal}))\%$	$(1.916 \pm 0.027(\text{stat}) \pm 0.242(\text{cal}))\%$
OS c	$(5.500 \pm 0.116)\%$	$(32.581 \pm 0.092(\text{stat}) \pm 1.848(\text{cal}))\%$	$(0.668 \pm 0.016(\text{stat}) \pm 0.142(\text{cal}))\%$

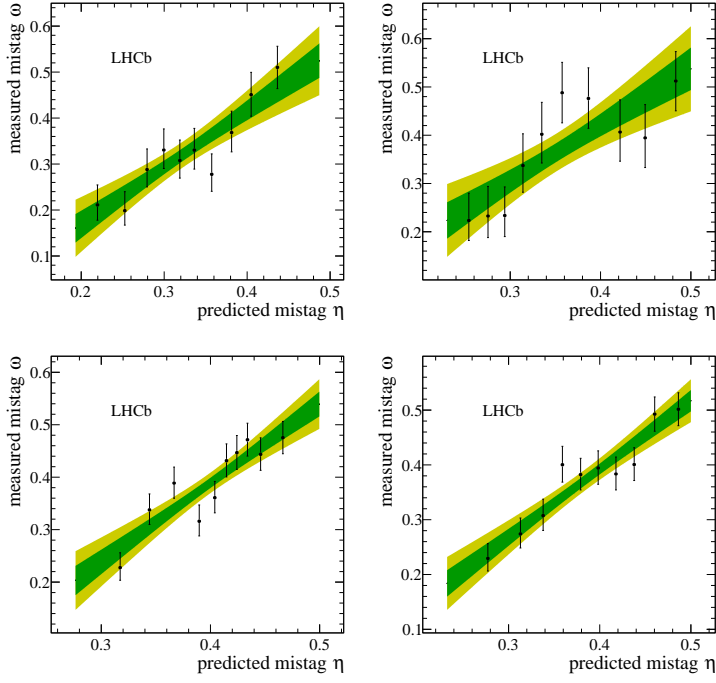


Figure 8.1: Predicted versus measured mistag probability for the (top left) OS muon, (top right) OS electron, (bottom left) OS kaon and (bottom right) OS vertex charge tagger for Run-I. A linear fit, including the 1σ and 2σ error bands is overlaid for each tagger.

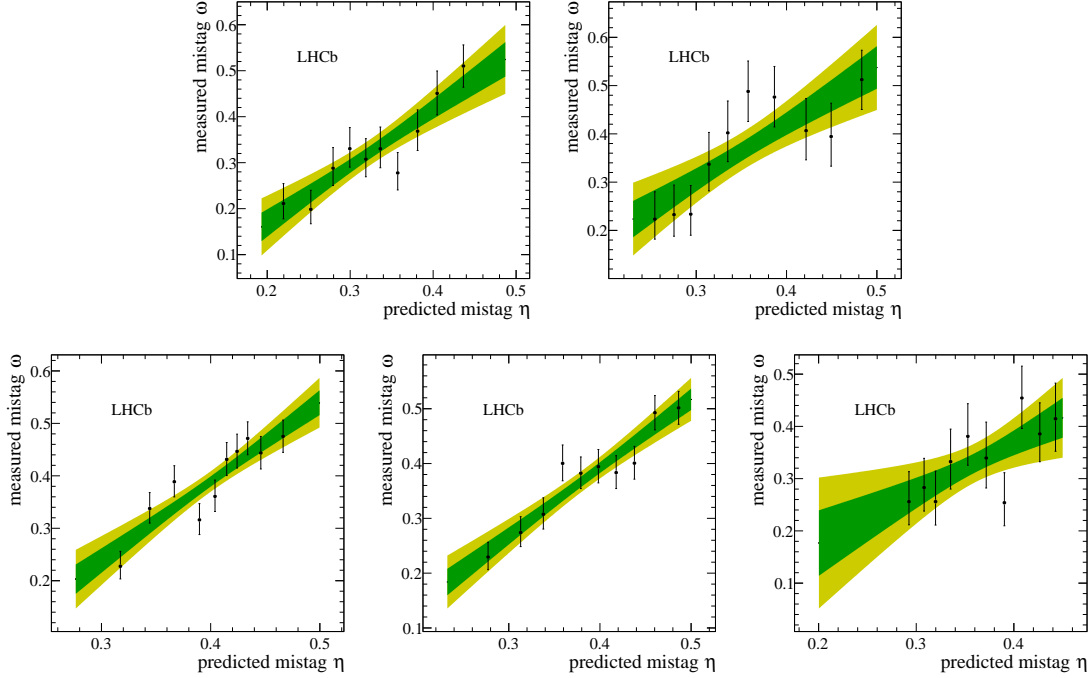


Figure 8.2: Predicted versus measured mistag probability for the (top left) OS muon, (top right) OS electron, (bottom left) OS kaon, (bottom middle) OS vertex charge and (bottom right) OS charm tagger for Run-II. A linear fit, including the 1σ and 2σ error bands is overlaid for each tagger.

755 8.2 Tagging performance

756 The OS-Combo and SS-Kaon taggers are calibrated simultaneously by fitting the $B_s \rightarrow$
 757 $D_s\pi\pi\pi$ decay-time distribution as discussed in Sec. 10. In this fit, the predicted mistag
 758 probabilities η_{OS} and η_{SS} , shown Fig. 8.3 for $B_s \rightarrow D_s\pi\pi\pi$ and $B_s \rightarrow D_sK\pi\pi$ data, are
 759 included as per-event observables, effectively giving a larger weight to the events that have
 760 a lower mistag probability. The tagger responses are combined into a single response on
 761 an event-by-event basis during the fit. Tables 8.3 and 8.4 report the tagging performances
 762 for the OS and SS combination considering three mutually exclusive categories of tagged
 763 events: OS only, SS only and both OS and SS. The tagging calibration parameters are
 764 listed in Table 10.1.

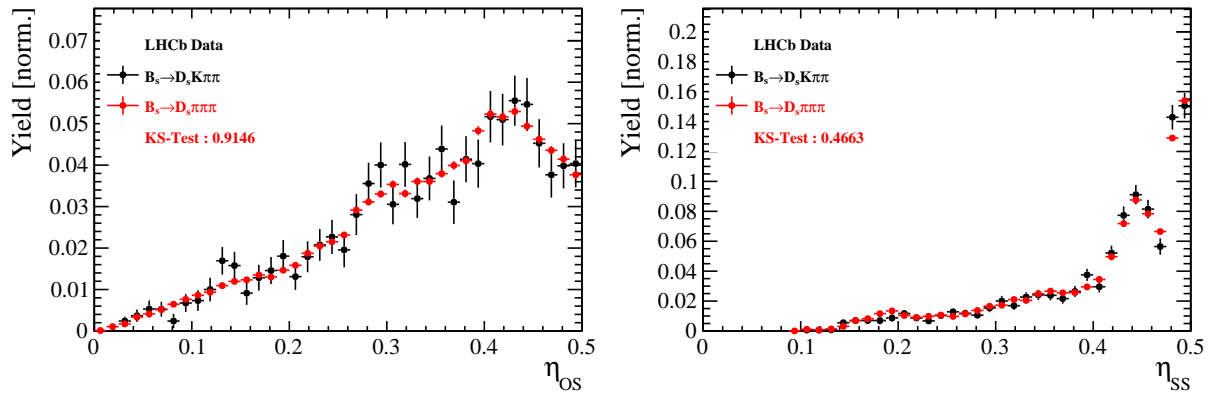


Figure 8.3: Distributions of the predicted mistag η for the OS combination (left) and the SS kaon tagger (right) for signal candidates in the $B_s^0 \rightarrow D_s K\pi\pi$ (black) and $B_s^0 \rightarrow D_s \pi\pi\pi$ (red) data samples.

Table 8.3: The flavour tagging performances for only OS tagged, only SS tagged and both OS and SS tagged events for Run-I data.

$B_s \rightarrow D_s\pi\pi\pi$	$\epsilon_{tag} [\%]$	$\langle \omega \rangle [\%]$	$\epsilon_{eff} [\%]$
Only OS	14.74 ± 0.11	39.09 ± 0.80	1.25 ± 0.16
Only SS	35.38 ± 0.18	44.26 ± 0.62	1.05 ± 0.18
Both OS-SS	33.04 ± 0.30	37.33 ± 0.73	3.41 ± 0.33
Combined	83.16 ± 0.37	40.59 ± 0.70	5.71 ± 0.40

Table 8.4: The flavour tagging performances for only OS tagged, only SS tagged and both OS and SS tagged events for Run-II data.

$B_s \rightarrow D_s\pi\pi\pi$	$\epsilon_{tag} [\%]$	$\langle \omega \rangle [\%]$	$\epsilon_{eff} [\%]$
Only OS	11.78 ± 0.05	37.01 ± 0.51	1.15 ± 0.07
Only SS	41.28 ± 0.10	42.65 ± 0.35	1.79 ± 0.12
Both OS-SS	28.62 ± 0.15	35.35 ± 0.40	3.63 ± 0.16
Combined	81.68 ± 0.19	39.28 ± 0.40	6.57 ± 0.21

9 Production and Detection Asymmetries

9.1 B_s Production Asymmetry

The production rates of b and \bar{b} hadrons in pp collisions are not expected to be identical, therefore this effect must be taken into account when computing CP asymmetries. The production asymmetry for B_s mesons is defined as:

$$A_p(B_s^0) = \frac{\sigma(\bar{B}_s^0) - \sigma(B_s^0)}{\sigma(\bar{B}_s^0) + \sigma(B_s^0)} \quad (9.1)$$

where σ are the corresponding production cross-section. This asymmetry was measured by LHCb in pp collisions at $\sqrt{s} = 7$ TeV and $\sqrt{s} = 8$ TeV by means of a time-dependent analysis of $B_s \rightarrow D_s^- \pi^+$ decays [39]. The results in bins of p_T and η of the B_s meson are shown in Table 9.1. To correct for the different kinematics of $B_s \rightarrow D_s^- \pi^+$ and $B_s^0 \rightarrow D_s K\pi\pi$ decays, the measured B_s production asymmetries $A_p(p_T, \eta)$ are folded with the sWeighted p_T, η distribution of our signal channel. The resulting effective production asymmetries are:

$$A_p(B_s^0)_{2011} = (-0.506 \pm 1.90)\% \quad (9.2)$$

$$A_p(B_s^0)_{2012} = (-0.164 \pm 1.30)\% \quad (9.3)$$

$$A_p(B_s^0)_{\text{Run-I}} = (-0.045 \pm 1.04)\%. \quad (9.4)$$

As for Run-II data no measurement is available yet, we determine the production asymmetry from $B_s \rightarrow D_s \pi\pi\pi$ data together with the tagging parameters.

Table 9.1: B_s production asymmetries in kinematic bins for 2011 and 2012 data. [39]

p_T [GeV/c]	η	$A_p(B_s^0)_{\sqrt{s}=7 \text{ TeV}}$	$A_p(B_s^0)_{\sqrt{s}=8 \text{ TeV}}$
(2.00, 7.00)	(2.10, 3.00)	$0.0166 \pm 0.0632 \pm 0.0125$	$0.0412 \pm 0.0416 \pm 0.0150$
(2.00, 7.00)	(3.00, 3.30)	$0.0311 \pm 0.0773 \pm 0.0151$	$-0.0241 \pm 0.0574 \pm 0.0079$
(2.00, 7.00)	(3.30, 4.50)	$-0.0833 \pm 0.0558 \pm 0.0132$	$0.0166 \pm 0.0391 \pm 0.0092$
(7.00, 9.50)	(2.10, 3.00)	$0.0364 \pm 0.0479 \pm 0.0068$	$0.0482 \pm 0.0320 \pm 0.0067$
(7.00, 9.50)	(3.00, 3.30)	$0.0206 \pm 0.0682 \pm 0.0127$	$0.0983 \pm 0.0470 \pm 0.0155$
(7.00, 9.50)	(3.30, 4.50)	$0.0058 \pm 0.0584 \pm 0.0089$	$-0.0430 \pm 0.0386 \pm 0.0079$
(9.50, 12.00)	(2.10, 3.00)	$-0.0039 \pm 0.0456 \pm 0.0121$	$0.0067 \pm 0.0303 \pm 0.0063$
(9.50, 12.00)	(3.00, 3.30)	$0.1095 \pm 0.0723 \pm 0.0179$	$-0.1283 \pm 0.0503 \pm 0.0171$
(9.50, 12.00)	(3.30, 4.50)	$0.1539 \pm 0.0722 \pm 0.0212$	$-0.0500 \pm 0.0460 \pm 0.0104$
(12.00, 30.00)	(2.10, 3.00)	$-0.0271 \pm 0.0336 \pm 0.0061$	$-0.0012 \pm 0.0222 \pm 0.0050$
(12.00, 30.00)	(3.00, 3.30)	$-0.0542 \pm 0.0612 \pm 0.0106$	$0.0421 \pm 0.0416 \pm 0.0162$
(12.00, 30.00)	(3.30, 4.50)	$-0.0586 \pm 0.0648 \pm 0.0150$	$0.0537 \pm 0.0447 \pm 0.0124$

779 9.2 $K^-\pi^+$ Detection Asymmetry

780 The presented measurement of the CKM-angle γ using $B_s^0 \rightarrow D_s K\pi\pi$ decays is sensitive to
 781 a possible charge asymmetry of the kaon. Kaons are known to have a nuclear cross-section
 782 which is asymmetrically dependent on the sign of their charge. It is indispensable to
 783 determine the charge asymmetry of the kaon, as fitting without taking this effect into
 784 account would introduce a 'fake' CP violation. Instead of determining the single track
 785 detection asymmetry of a kaon, it is found that the combined two track asymmetry of a
 786 kaon-pion pair is much easier to access [40]. Therefore, the two track asymmetry defined
 787 as

$$A^{det}(K^-\pi^+) = \frac{\epsilon^{det}(K^-\pi^+) - \epsilon^{det}(K^+\pi^-)}{\epsilon^{det}(K^-\pi^+) + \epsilon^{det}(K^+\pi^-)}, \quad (9.5)$$

788 is used. This asymmetry can be measured from the difference in asymmetries in the
 789 $D^+ \rightarrow K^-\pi^+\pi^+$ and $D^+ \rightarrow K_s^0\pi^+$ modes [41]:

$$\begin{aligned} A^{det}(K^-\pi^+) &= \frac{N(D^+ \rightarrow K^-\pi^+\pi^+) - N(D^- \rightarrow K^+\pi^-\pi^-)}{N(D^+ \rightarrow K^-\pi^+\pi^+) + N(D^- \rightarrow K^+\pi^-\pi^-)} \\ &\quad - \frac{N(D^+ \rightarrow K_s^0\pi^+) - N(D^- \rightarrow K_s^0\pi^-)}{N(D^+ \rightarrow K_s^0\pi^+) + N(D^- \rightarrow K_s^0\pi^-)} \\ &\quad - A(K^0), \end{aligned} \quad (9.6)$$

790 where possible CP violation in the $D^+ \rightarrow K_s^0\pi^+$ mode is predicted to be smaller than
 791 10^{-4} in the Standard Model [42]. The small asymmetry in the neutral kaon system,
 792 $A(\bar{K}^0) = -A(K^0) = (-0.054 \pm 0.014)\%$ [41], has to be taken into account as a correction.

793 We use a dedicated LHCb tool to determine $A^{det}(K^-\pi^+)$ for all data taking periods
 794 used in this analysis. A detailed description can be found in [41]. The tool provides
 795 large calibration samples of $D^\pm \rightarrow K^\pm\pi^\pm\pi^\pm$ and $D^\pm \rightarrow K_s^0\pi^\pm$ decays, which are used
 796 to determine the asymmetry following Eq. 9.6. Several weighting steps are performed
 797 to match the kinematics of the calibration samples to our signal decay sample. First,
 798 weights are assigned to the K^\pm and π^\pm of the $D^\pm \rightarrow K^\pm\pi^\pm\pi^\pm$ sample, using p, η of the
 799 K^\pm and p_T, η of the π^\pm from our $B_s^0 \rightarrow D_s K\pi\pi$ signal decay. Then, weights are assigned
 800 to the $D^\pm (p_T, \eta)$ and the $\pi^\pm (p_T)$ of the $D^\pm \rightarrow K_s^0\pi^\pm$ sample to match the corresponding,
 801 weighted distributions of the $D^\pm \rightarrow K^\pm\pi^\pm\pi^\pm$ sample. In a last step, weights are assigned
 802 to match the bachelor pions ϕ distributions between the two calibration samples. After the
 803 samples are weighted, fits are performed to the invariant $m(K^-\pi^+\pi^+)/m(K^+\pi^-\pi^-)$ and
 804 $m(K_s^0\pi^+)/m(K_s^0\pi^-)$ distributions to determine $A^{det}(K^-\pi^+)$. The PDFs used to describe
 805 the invariant mass distributions consist of gaussian functions for the signal component
 806 and exponentials describing the residual background.

807 The detection asymmetry is determined separately for every year and (since it is a
 808 charge asymmetry effect) magnet polarity. Serving as an example for Run-I and Run-
 809 II, the fits used to determine $N(D^+ \rightarrow K^-\pi^+\pi^+)/N(D^- \rightarrow K^+\pi^-\pi^-)$ and $N(D^+ \rightarrow$
 $810 K_s^0\pi^+)/N(D^- \rightarrow K_s^0\pi^-)$ for 2011, magnet up data and 2015, magnet up data are shown
 811 in Fig. 9.1 and 9.2 respectively. The obtained values of $A^{det}(K^-\pi^+) + A(K^0)$ for all
 812 years and polarities are shown in Table 9.2. Here, only the decay modes $B_s^0 \rightarrow (D_s \rightarrow$
 $813 KK\pi)K\pi\pi$ and $B_s^0 \rightarrow (D_s \rightarrow \pi\pi\pi)K\pi\pi$ are considered. For $B_s^0 \rightarrow (D_s \rightarrow K\pi\pi)K\pi\pi$,
 814 the contributions of the two oppositely charged kaons cancel each other and a detection
 815 asymmetry of zero with the same uncertainty as determined for $D_s \rightarrow KK\pi$ and $D_s \rightarrow \pi\pi\pi$

is assumed. In contrast, only the decay mode $D_s \rightarrow KK\pi$ is a source of detection asymmetry for $B_s^0 \rightarrow D_s\pi\pi\pi$ decays resulting in an average detection asymmetry of $A^{det}(K^-\pi^+) = -0.07 \pm 0.15\%$ (Run-I) and $A^{det}(K^-\pi^+) = -0.08 \pm 0.21\%$ (Run-II).

Data sample	$A^{det}(K^-\pi^+) + A(K^0)$ [%]
Run-I	
2011, mag. up	-2.01 \pm 0.32
2011, mag. down	-0.16 \pm 0.28
2011, average	-1.09 \pm 0.21
2012, mag. up	-0.90 \pm 0.20
2012, mag. down	-1.01 \pm 0.22
2012, average	-0.96 \pm 0.15
Run-II	
mag. up	-1.16 \pm 0.34
mag. down	-0.65 \pm 0.27
average	-0.91 \pm 0.22

Table 9.2: Summary of the $K^-\pi^+$ detection asymmetries for $B_s^0 \rightarrow D_s K\pi\pi$ decays obtained from the fits to the Run-I and Run-II calibration samples.

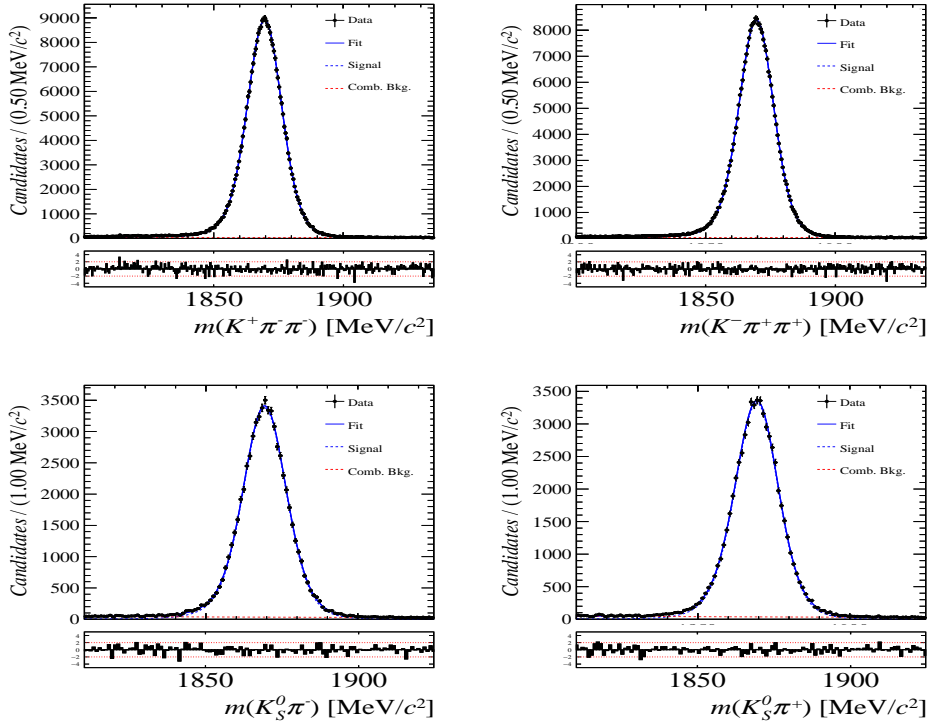


Figure 9.1: Distributions of the invariant mass of (top) $D^\pm \rightarrow K^\pm \pi^\pm \pi^\pm$ and (bottom) $D^\pm \rightarrow K_s^0 \pi^\pm$ candidates for Run-I data from the calibration samples. A fit described in the text is overlaid.

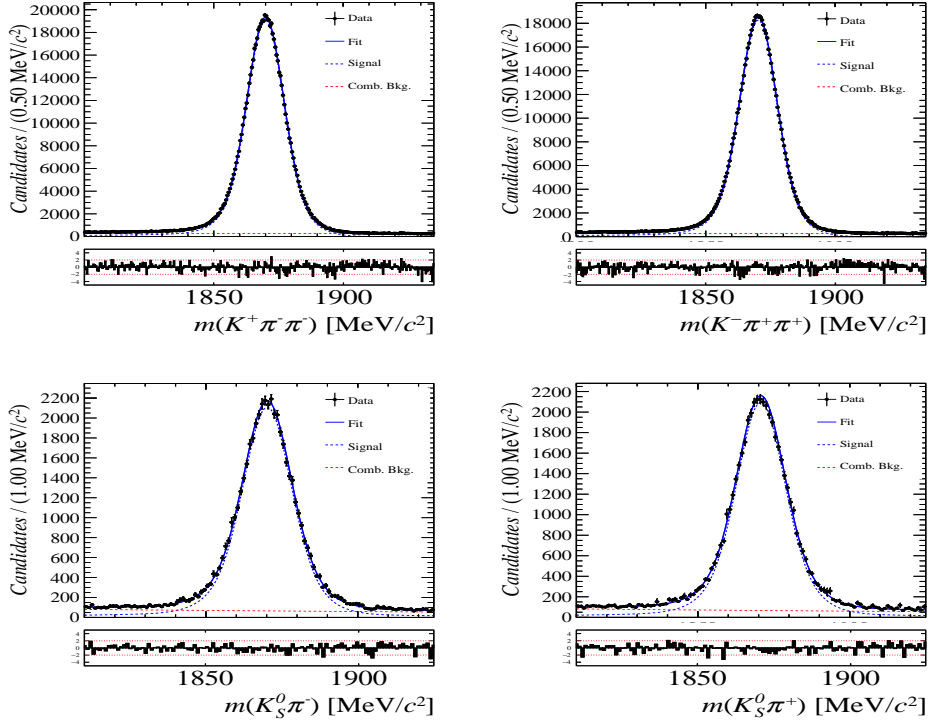


Figure 9.2: Distributions of the invariant mass of (top) $D^\pm \rightarrow K^\pm \pi^\pm \pi^\pm$ and (bottom) $D^\pm \rightarrow K_s^0 \pi^\pm$ candidates for Run-II data from the calibration samples. A fit described in the text is overlaid.

819 10 Decay-time fit

820 This section covers the (phase space integrated) decay-time fits to $B_s^0 \rightarrow D_s h\pi\pi$ data. We
 821 use the **sFit** technique [43] to statistically subtract the background, leaving only the signal
 822 PDF to describe the decay-time. The **sWeights** are calculated based on the fit to the
 823 reconstructed B_s mass distribution described in Sec. 5. The signal PDF is conditional on
 824 the tagging decisions q_i , the mistag estimates η_i ($i = \text{OS,SS}$) and the decay-time error σ_t :

$$825 \quad \mathcal{P}(t|\sigma_t, q_{\text{OS}}, \eta_{\text{OS}}, q_{\text{SS}}, \eta_{\text{SS}}) \propto \left[p(t'|q_{\text{OS}}, \eta_{\text{OS}}, q_{\text{SS}}, \eta_{\text{SS}}) \otimes \mathcal{R}(t - t', \sigma_t) \right] \cdot \epsilon(t) \quad (10.1)$$

825 where $p(t|q_{\text{OS}}, \eta_{\text{OS}}, q_{\text{SS}}, \eta_{\text{SS}})$ is given by Equation 2.7 taking the tagging dilution into
 826 account. The decay-time acceptance $\epsilon(t)$ (Sec. 7) and the Gaussian time-resolution
 827 function $\mathcal{R}(t - t', \sigma_t)$ (Sec. 6) are fixed to the values obtained by the dedicated studies.
 828 We fix the values of Γ_s and $\Delta\Gamma_s$ to the latest HFLAV results [35].

829 The unbinned maximum likelihood fits are performed simultaneously in six categories:
 830 [Run-I,L0-TOS], [Run-I,L0-TIS], [Year-15/16,L0-TOS], [Year-15/16,L0-TIS], [Year-17,L0-
 831 TOS] and [Year-17,L0-TIS] to account for different time-acceptance shapes, time-resolution
 832 and tagging calibrations.

833 10.1 Fit to $B_s^0 \rightarrow D_s\pi\pi\pi$ data

834 Since the decay $B_s^0 \rightarrow D_s\pi\pi\pi$ is flavour specific, the CP coefficients can be fixed to $C = 1$
 835 and $D_f = D_{\bar{f}} = S_f = S_{\bar{f}} = 0$. The fit determines the calibration parameters for the
 836 OS-Combo and SS-Kaon taggers, the B_s^0 production asymmetry for Run-II data as well as
 837 the mixing frequency Δm_s . Table 10.1 summarizes the fitted parameters. The **sWeighted**
 838 decay-time distribution and the time-dependent asymmetry A_{mix} between mixed and
 839 unmixed B_s^0 candidates are shown in Fig. 10.1 along with the fit projections.

840 10.2 Fit to $B_s^0 \rightarrow D_sK\pi\pi$ data

841 The measured CP coefficients $C, D_f, D_{\bar{f}}, S_f$ and $S_{\bar{f}}$ extracted from a fit to the $B_s \rightarrow$
 842 $D_s K\pi\pi$ decay-time distribution are reported in Table 10.2. The fit projection is shown in
 843 Fig. 10.2. We included a multi-dimensional Gaussian-constraint for the tagging calibration
 844 parameters (including the tagging asymmetries) with the central values and covariance
 845 matrix determined in Sec. 10.1.

846 The CP coefficients are converted to the observables $r, \kappa, \delta, \gamma$ using the GammaCombo
 847 package. The corresponding confidence levels are shown in Fig 10.3 and are dominated by
 848 the statistical uncertainty of the measured CP coefficients.

Table 10.1: Parameters determined from a fit to the $B_s \rightarrow D_s \pi\pi\pi$ decay-time distribution. The uncertainties are statistical and systematic, respectively.

Fit Parameter	Run-I	Run-II
p_0^{OS}	$0.398 \pm 0.010 \pm 0.010$	$0.371 \pm 0.005 \pm 0.005$
p_1^{OS}	$0.894 \pm 0.085 \pm 0.089$	$0.784 \pm 0.043 \pm 0.026$
Δp_0^{OS}	$0.030 \pm 0.011 \pm 0.002$	$0.007 \pm 0.006 \pm 0.002$
Δp_1^{OS}	$0.011 \pm 0.095 \pm 0.023$	$0.065 \pm 0.053 \pm 0.009$
$\epsilon_{tag}^{OS} [\%]$	$47.775 \pm 0.365 \pm 0.080$	$40.413 \pm 0.182 \pm 0.036$
$\Delta \epsilon_{tag}^{OS} [\%]$	$-0.001 \pm 1.353 \pm 0.125$	$0.313 \pm 0.619 \pm 0.081$
p_0^{SS}	$0.444 \pm 0.008 \pm 0.005$	$0.428 \pm 0.004 \pm 0.002$
p_1^{SS}	$0.949 \pm 0.111 \pm 0.067$	$0.787 \pm 0.039 \pm 0.025$
Δp_0^{SS}	$-0.019 \pm 0.009 \pm 0.001$	$-0.017 \pm 0.004 \pm 0.000$
Δp_1^{SS}	$0.065 \pm 0.124 \pm 0.017$	$0.027 \pm 0.048 \pm 0.009$
$\epsilon_{tag}^{SS} [\%]$	$68.426 \pm 0.340 \pm 0.037$	$69.700 \pm 0.171 \pm 0.287$
$\Delta \epsilon_{tag}^{SS} [\%]$	$0.004 \pm 1.242 \pm 0.089$	$-0.374 \pm 0.578 \pm 0.121$
$A_P [\%]$	-0.045 (fixed)	$-0.256 \pm 0.644 \pm 0.168$
$\Delta m_s [\text{ps}^{-1}]$		$17.7537 \pm 0.0084 \pm 0.0092$

Table 10.2: CP coefficients determined from a fit to the $B_s \rightarrow D_s K\pi\pi$ decay-time distribution. The uncertainties are statistical and systematic, respectively.

Fit Parameter	Value
C	$0.68 \pm 0.12 \pm 0.03$
D	$-0.00 \pm 0.32 \pm 0.12$
\bar{D}	$0.39 \pm 0.30 \pm 0.11$
S	$-0.15 \pm 0.17 \pm 0.03$
\bar{S}	$-0.53 \pm 0.17 \pm 0.03$

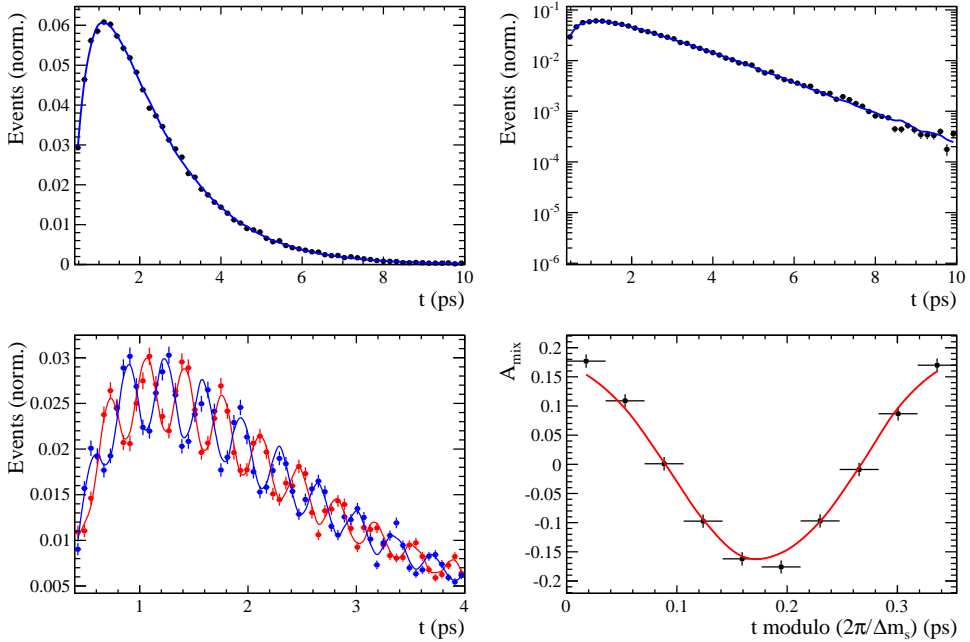


Figure 10.1: Top: Flavour averaged decay time distribution of $B_s^0 \rightarrow D_s\pi\pi\pi$ candidates. Bottom-left: Tagged decay time distribution of mixed (red) and unmixed (blue) signal candidates. Bottom-right: Time-dependent asymmetry A_{mix} between mixed and unmixed B_s^0 candidates folded into one oscillation period.

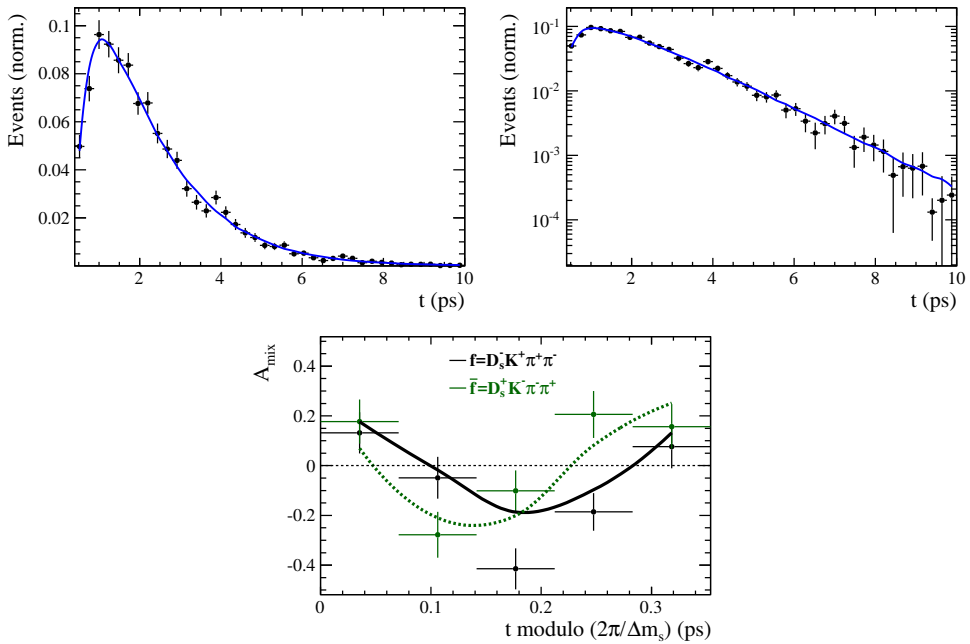


Figure 10.2: Decay-time distribution of $B_s^0 \rightarrow D_s K\pi\pi$ signal candidates with the fit projection overlaid.

Table 10.3: Statistical correlation of the CP coefficients.

	C	D	\bar{D}	S	\bar{S}
C	1.000	-0.134	-0.181	0.048	0.074
D		1.000	0.542	0.019	0.060
\bar{D}			1.000	0.005	0.118
S				1.000	0.006
\bar{S}					1.000

Table 10.4: Systematic correlation of the CP coefficients.

	C	D	\bar{D}	S	\bar{S}
C	1.000	-0.057	-0.069	-0.109	0.102
D		1.000	0.206	0.022	0.040
\bar{D}			1.000	0.008	0.071
S				1.000	-0.342
\bar{S}					1.000

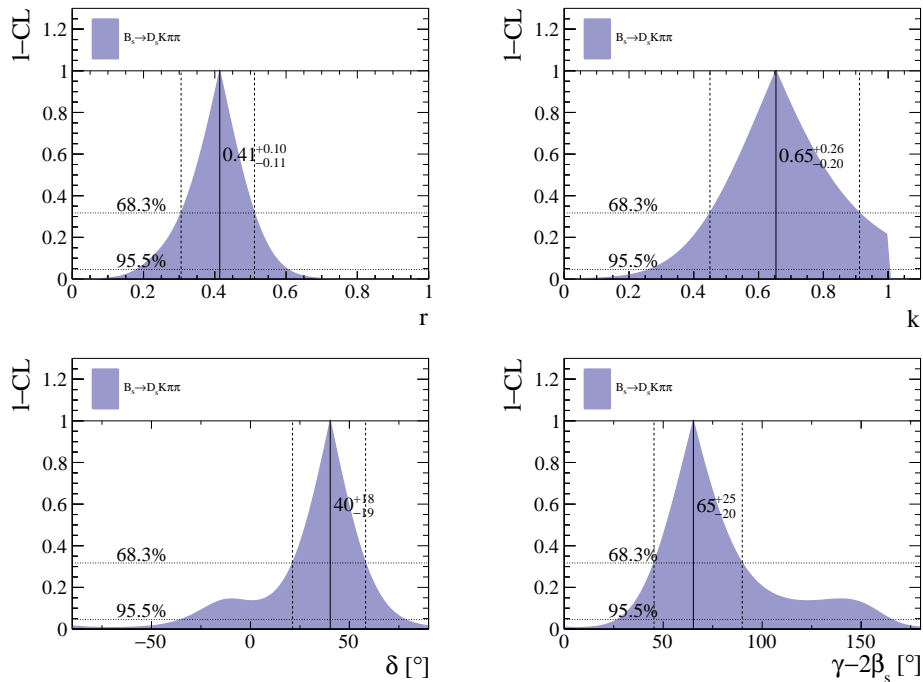


Figure 10.3: The 1-CL contours for the physical observable r , κ , δ and γ obtained with the phasespace-integrated fit.

849 11 Time-dependent amplitude fit

850 The signal PDF used for the full time-dependent fit is defined as

$$\mathcal{P}(\mathbf{x}, t | \sigma_t, q_{os}, \eta_{os}, q_{ss}, \eta_{ss}) \propto [p(\mathbf{x}, t' | q_{os}, \eta_{os}, q_{ss}, \eta_{ss}) \otimes \mathcal{R}(t - t', \sigma_t)] \cdot \epsilon(t) \quad (11.1)$$

851 where $p(\mathbf{x}, t | q_{os}, \eta_{os}, q_{ss}, \eta_{ss})$ is given the differential decay rate in Equation 2.28 taking
852 the tagging dilution into account. The phase space efficiency $\epsilon(\mathbf{x})$ is only included in the
853 normalization of $\mathcal{P}(\mathbf{x}, t | \sigma_t, q_{os}, \eta_{os}, q_{ss}, \eta_{ss})$ as discussed in Sec 7.3. The model selection
854 of the amplitude components is described in the following Section. The remaining fitting
855 strategy is exactly the same as for the decay-time fits, see Sec. 10.

856 11.1 Signal Model Construction

857 The light meson spectrum comprises multiple resonances which are expected to contribute
858 to $B_s \rightarrow D_s K\pi\pi$ decays as intermediate states. Apart from clear contributions coming
859 from resonances such as $K_1(1270)$, $K_1(1400)$, $\rho(770)$ and $K^*(892)^0$, the remaining structure
860 is impossible to infer due to the cornucopia of broad, overlapping and interfering resonances
861 within the phase space boundary. We follow the LASSO [44, 45] approach to limit the
862 model complexity in two steps.

863 First, we fit the time-integrated and flavour averaged phase-space distribution of
864 $B_s \rightarrow D_s K\pi\pi$ decays. In this case, a single total amplitude can be used:

$$\mathcal{A}_f^{eff}(\mathbf{x}) = \sum_i a_i^{eff} A_i(\mathbf{x}) \quad (11.2)$$

865 which effectively describes the incoherent superposition of the $b \rightarrow c$ and $b \rightarrow u$ amplitudes:

$$|A_f^{eff}(\mathbf{x})|^2 = |A_f^c(\mathbf{x})|^2 + |A_f^u(\mathbf{x})|^2. \quad (11.3)$$

866 This significantly simplifies the fitting procedure and allows us to include the whole pool
867 of considered intermediate state amplitudes A_i which can be found in Appendix J. The
868 LASSO penalty term added to the likelihood function

$$-2 \log \mathcal{L} \rightarrow -2 \log \mathcal{L} + \lambda \sum_i \sqrt{\int |a_i^{eff} A_i(\mathbf{x})|^2 d\Phi_4}, \quad (11.4)$$

869 shrinks the amplitude coefficients towards zero. The amount of shrinkage is controlled by
870 the parameter λ , to be tuned on data. Higher values for λ encourage sparse models, *i.e.*
871 models with only a few non-zero amplitude coefficients. The optimal value for λ is found
872 by minimizing the Bayesian information criteria [46] (BIC),

$$BIC(\lambda) = -2 \log \mathcal{L} + r \log N_{Sig}, \quad (11.5)$$

873 where N_{Sig} is the number of signal events and r is the number of amplitudes with a decay
874 fraction above a certain threshold. The fit fractions are defined as

$$F_i \equiv \frac{\int |a_i^{eff} A_i(\mathbf{x})|^2 d\Phi_4}{\int |\mathcal{A}_f^{eff}(\mathbf{x})|^2 d\Phi_4}, \quad (11.6)$$

and are a measure of the relative strength between the different transitions. Figure 11.1(left) shows the distribution of BIC values obtained by scanning over λ where we choose the decay fraction threshold to be 0.5%. At the optimal value of $\lambda = 50$, the set of amplitudes with a decay fraction above the threshold are considered further for step two of the model selection. The selected amplitudes and their fractions are summarized in Table 11.1. The fit projections are shown in Fig. 11.2. The set of selected amplitudes is stable for thresholds between 0.1% and 1%.. Other choices result in marginally different models containing one component more or less. These are included in the set of alternative models used for the systematic studies presented in Sec. 12.10.

In Stage 2, the LASSO procedure is again performed by fitting the full time-dependent amplitude PDF. The components selected by Stage 1 are included for both $b \rightarrow c$ and $b \rightarrow u$ transitions and the likelihood is extended as follows:

$$-2 \log \mathcal{L} \rightarrow -2 \log \mathcal{L} + \lambda \sum_i \sqrt{\int |a_i^c A_i(\mathbf{x})|^2 d\Phi_4} + \lambda \sum_i \sqrt{\int |a_i^u A_i(\mathbf{x})|^2 d\Phi_4} \quad (11.7)$$

Figure 11.1(right) shows a plot of the complexity factor λ , against the resulting BIC values. The final set of $b \rightarrow c$ and $b \rightarrow u$ amplitudes is selected using the optimal value of $\lambda = 6$, and is henceforth called the LASSO model. The parameters of chosen resonances are summarized in Appendix K.

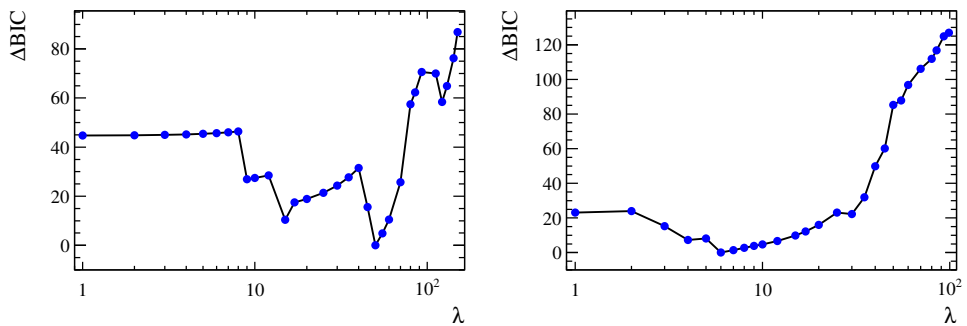


Figure 11.1: Difference in the BIC value from its minimum as function of the LASSO parameter λ for step 1 (left) and step 2 (right) of the model selection.

Table 11.1: Fit fractions of the amplitudes selected by Stage 1 of the model selection procedure.

Decay channel	Fraction [%]
$B_s \rightarrow K(1)(1270)^+ (\rightarrow K^*(892)^0 (\rightarrow K^+ \pi^-) \pi^+) D_s^-$	8.56 ± 1.43
$B_s \rightarrow K(1)(1400)^+ (\rightarrow K^*(892)^0 (\rightarrow K^+ \pi^-) \pi^+) D_s^-$	43.72 ± 2.80
$B_s \rightarrow K(1460)^+ (\rightarrow K^*(892)^0 (\rightarrow K^+ \pi^-) \pi^+) D_s^-$	3.25 ± 0.69
$B_s \rightarrow K^*(1410)^+ (\rightarrow K^*(892)^0 (\rightarrow K^+ \pi^-) \pi^+) D_s^-$	15.33 ± 1.13
$B_s \rightarrow (D_s^- \pi^+)_P K^*(892)^0 (\rightarrow K^+ \pi^-)$	4.63 ± 0.69
$B_s \rightarrow K^*(1410)^+ (\rightarrow \rho(770)^0 (\rightarrow \pi^+ \pi^-) K^+) D_s^-$	5.58 ± 0.62
$B_s \rightarrow (D_s^- K^+)_P \rho(770)^0 (\rightarrow \pi^+ \pi^-)$	1.49 ± 0.40
$B_s \rightarrow K(1)(1270)^+ (\rightarrow K(0)^*(1430)^0 (\rightarrow K^+ \pi^-) \pi^+) D_s^-$	4.72 ± 0.54
$B_s \rightarrow K(1)(1270)^+ (\rightarrow \rho(770)^0 (\rightarrow \pi^+ \pi^-) K^+) D_s^-$	14.20 ± 1.56
Sum	101.47 ± 3.86

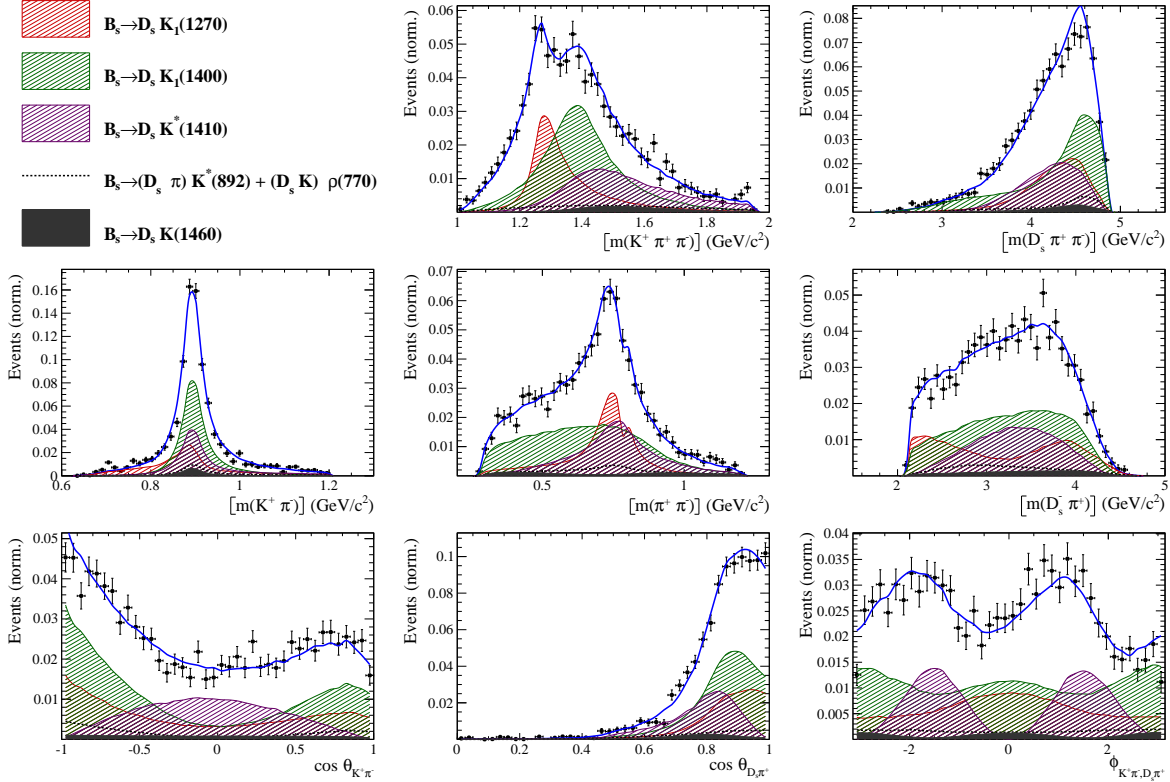


Figure 11.2: Projections of the fit result to the time-integrated and flavour averaged phase-space distribution of $B_s \rightarrow D_s K\pi\pi$ decays. The incoherent contributions of the selected decay channels are plotted as well.

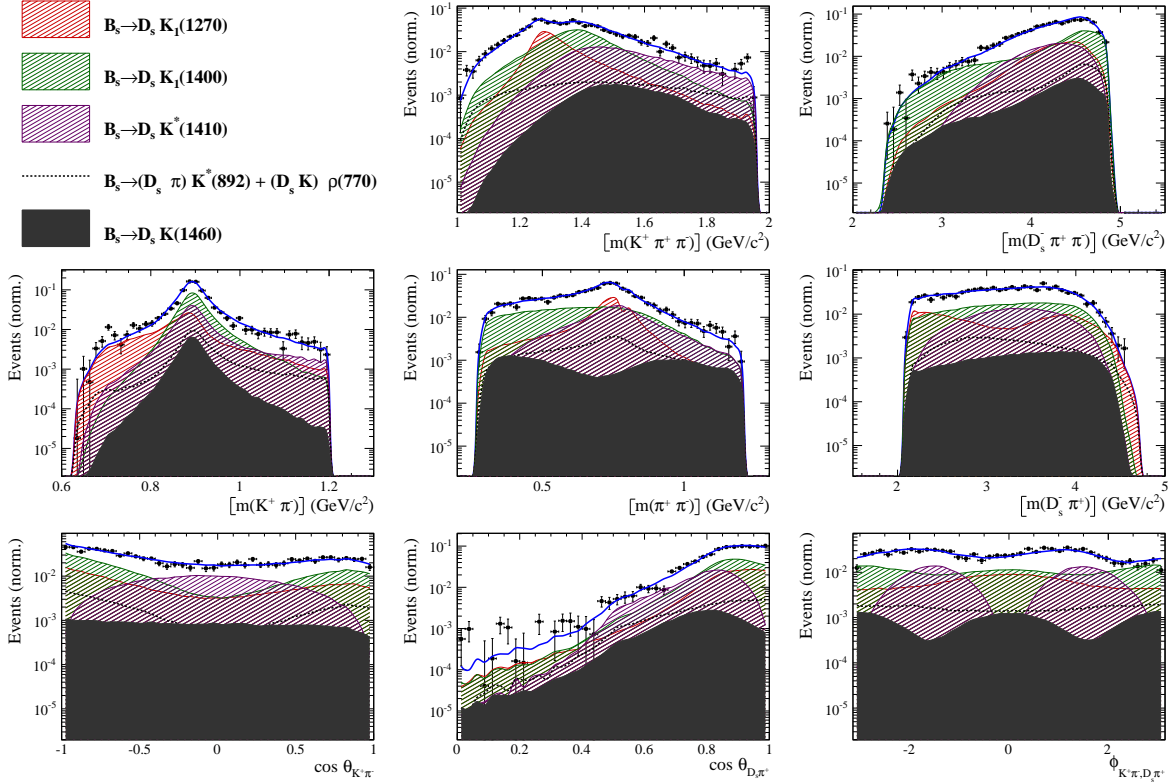


Figure 11.3: Projections of the fit result to the time-integrated and flavour averaged phase-space distribution of $B_s \rightarrow D_s K\pi\pi$ decays in logarithmic scale. The incoherent contributions of the selected decay channels are plotted as well.

891 11.2 Results

892 Table 11.2 lists the modulus and phases of the complex amplitude coefficients a_i^c and a_i^u ,
 893 obtained by fitting the LASSO model to the data. The corresponding fit fractions for the
 894 $b \rightarrow c$ and $b \rightarrow u$ amplitudes are individually normalized

$$F_i^{c,u} \equiv \frac{\int |a_i^{c,u} A_i(\mathbf{x})|^2 d\Phi_4}{\int |\mathcal{A}_f^{c,u}(\mathbf{x})|^2 d\Phi_4} \quad (11.8)$$

895 and shown in Table 11.3. The statistical significances of the three smallest contributions
 896 are: 4.5σ for $B_s \rightarrow (D_s K)_P \rho(770)$; 6.2σ for $B_s \rightarrow D_s (K(1460) \rightarrow K^*(892) \pi)$ and
 897 8.2σ for $B_s \rightarrow (D_s \pi)_P K^*(892)$. These are calculated from the likelihood difference
 898 $\sqrt{\Delta(-2LL)}$ between a fit with and without the respective component assuming Wilk's
 899 theorem. In addition to the amplitude coefficients, the amplitude ratio and the strong and
 900 weak phase differences between the $b \rightarrow c$ and $b \rightarrow u$ decays are determined. Moreover,
 901 the masses and widths of the $K_1(1400)$ and $K^*(1410)$ resonances are fitted.

902 Figure 11.4 shows the distributions of selected phase space observables, which demon-
 903 strate reasonable agreement between data and the fit model. We also project into the
 904 transversity basis to demonstrate good description of the overall angular structure (see
 905 11.4 bottom row). The acoplanarity angle χ , is the angle between the two decay planes
 906 formed by the $K^+ \pi^-$ system and the $D_s^- \pi^+$ system in the B_s rest frame; boosting into the
 907 rest frames of the two-body systems defining these decay planes, the two helicity variables
 908 are defined as the cosine of the angle, θ , of the K^+ or D_S^- momentum with the B_s flight
 909 direction.

910 In order to quantify the quality of the fit in the five-dimensional phase space, a χ^2
 911 value is determined by binning the data;

$$\chi^2 = \sum_{b=1}^{N_{\text{bins}}} \frac{(N_b - N_b^{\text{exp}})^2}{N_b^{\text{exp}}}, \quad (11.9)$$

912 where N_b is the number of data events in a given bin, N_b^{exp} is the event count predicted
 913 by the fitted PDF and N_{bins} is the number of bins. An adaptive binning is used to ensure
 914 sufficient statistics in each bin for a robust χ^2 calculation [47]. At least 25 events per
 915 bin are required. The number of degrees of freedom ν , in an unbinned fit is bounded by
 916 $N_{\text{bins}} - 1$ and $(N_{\text{bins}} - 1) - N_{\text{par}}$, where N_{par} is the number of free fit parameters. We use
 917 the χ^2 value divided by $\nu = (N_{\text{bins}} - 1) - N_{\text{par}}$ as a conservative estimate. For the LASSO
 918 model, this amounts to $\chi^2/\nu = 1.40$ with $\nu = 137$, indicating a decent fit quality.

Table 11.2: Modulus and phases of the amplitudes contributing to $b \rightarrow c$ and $b \rightarrow u$ decays. In case of multiple decay modes of three-body resonances, the amplitude coefficients are defined relative to the one listed first. Additional fit parameters are listed below. The first quoted uncertainty is statistical, while the second arises from systematic sources. The third uncertainty arises from the alternative models considered.

Decay Channel	$A_{b \rightarrow c}$		$A_{b \rightarrow u}$	
	$ a_i $	$\arg(a_i)[^\circ]$	$ a_i $	$\arg(a_i)[^\circ]$
$B_s \rightarrow D_s (K_1(1270) \rightarrow K \rho(770))$	1.0	0.0	1.0	0.0
$K_1(1270) \rightarrow K^*(892) \pi$	$0.72 \pm 0.11 \pm 0.09$	$50.1 \pm 8.4 \pm 5.9$		
$K_1(1270) \rightarrow K_0^*(1430) \pi$	$0.52 \pm 0.04 \pm 0.06$	$128.9 \pm 5.0 \pm 18.0$		
$B_s \rightarrow D_s (K_1(1400) \rightarrow K^*(892) \pi)$	$1.98 \pm 0.08 \pm 0.19$	$10.5 \pm 9.3 \pm 6.2$	$0.74 \pm 0.20 \pm 0.16$	$-64.3 \pm 12.9 \pm 13.2$
$B_s \rightarrow D_s (K^*(1410) \rightarrow K^*(892) \pi)$	$1.14 \pm 0.08 \pm 0.09$	$55.0 \pm 4.6 \pm 5.1$		
$K^*(1410) \rightarrow K \rho(770)$	$0.63 \pm 0.05 \pm 0.04$	$-164.1 \pm 5.3 \pm 3.2$		
$B_s \rightarrow D_s (K(1460) \rightarrow K^*(892) \pi)$			$0.87 \pm 0.10 \pm 0.10$	$-96.3 \pm 11.5 \pm 11.3$
$B_s \rightarrow (D_s \pi)_P K^*(892)$	$0.72 \pm 0.10 \pm 0.13$	$-17.2 \pm 12.4 \pm 13.0$	$1.13 \pm 0.12 \pm 0.15$	$-16.8 \pm 14.3 \pm 16.8$
$B_s \rightarrow (D_s K)_P \rho(770)$			$0.53 \pm 0.08 \pm 0.07$	$33.6 \pm 10.6 \pm 11.2$
Fit parameter	Value			
$m_{K_1(1400)}$ [MeV]	$1397 \pm 10 \pm 5 \pm 7$			
$\Gamma_{K_1(1400)}$ [MeV]	$205 \pm 15 \pm 11 \pm 8$			
$m_{K^*(1410)}$ [MeV]	$1432 \pm 10 \pm 17 \pm 8$			
$\Gamma_{K^*(1410)}$ [MeV]	$345 \pm 25 \pm 37 \pm 17$			
r	$0.50 \pm 0.05 \pm 0.03 \pm 0.02$			
$\delta [^\circ]$	$46 \pm 14 \pm 7 \pm 8$			
$\gamma - 2\beta_s [^\circ]$	$61 \pm 15 \pm 6 \pm 6$			

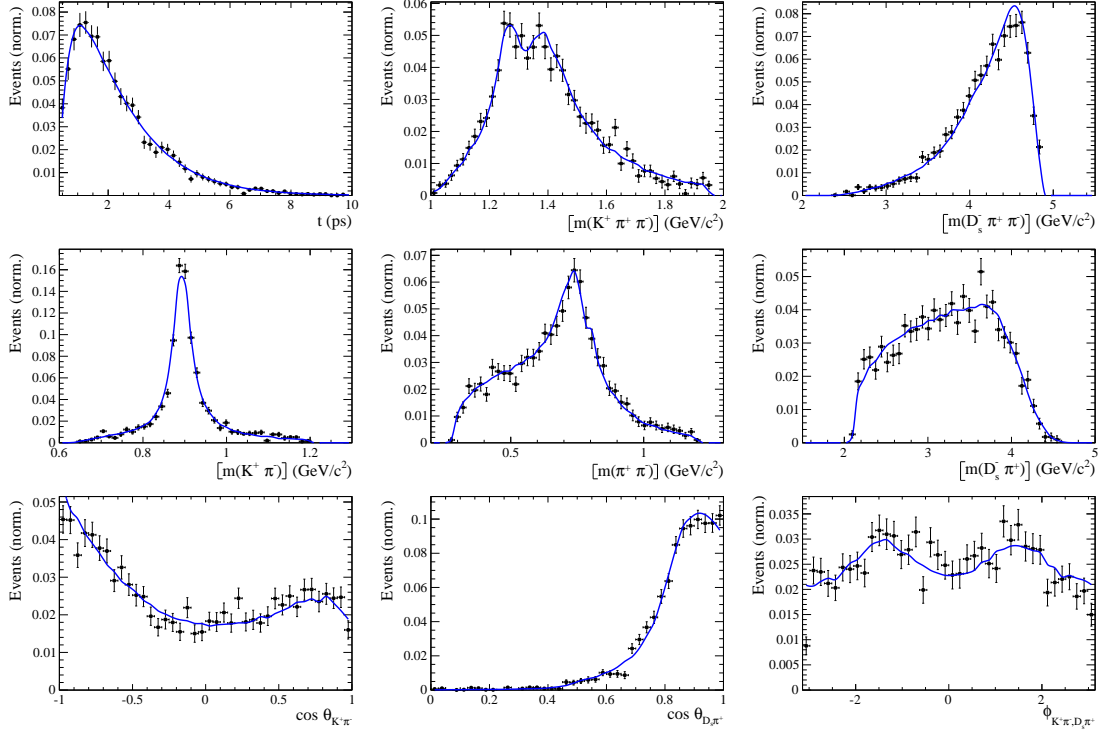


Figure 11.4: Projections of the full time-dependent amplitude fit.

Table 11.3: Fit fractions of the amplitudes contributing to $b \rightarrow c$ and $b \rightarrow u$ decays.

Decay Channel	$F_{b \rightarrow c} [\%]$	$F_{b \rightarrow u} [\%]$
$B_s \rightarrow D_s (K_1(1270) \rightarrow K^*(892) \pi)$	$6.3 \pm 1.6 \pm 1.7 \pm 0.8$	$14.9 \pm 4.5 \pm 4.6 \pm 4.3$
$B_s \rightarrow D_s (K_1(1270) \rightarrow K \rho(770))$	$12.3 \pm 1.4 \pm 1.4 \pm 1.9$	$29.1 \pm 6.1 \pm 6.6 \pm 6.2$
$B_s \rightarrow D_s (K_1(1270) \rightarrow K_0^*(1430) \pi)$	$3.4 \pm 0.5 \pm 0.9 \pm 0.5$	$8.0 \pm 2.1 \pm 2.5 \pm 1.7$
$B_s \rightarrow D_s (K_1(1400) \rightarrow K^*(892) \pi)$	$48.3 \pm 4.5 \pm 7.2 \pm 4.5$	$17.2 \pm 8.6 \pm 7.6 \pm 6.4$
$B_s \rightarrow D_s (K^*(1410) \rightarrow K^*(892) \pi)$	$15.5 \pm 1.0 \pm 1.4 \pm 1.1$	
$B_s \rightarrow D_s (K^*(1410) \rightarrow K \rho(770))$	$6.7 \pm 0.6 \pm 0.8 \pm 0.5$	
$B_s \rightarrow D_s (K(1460) \rightarrow K^*(892) \pi)$		$21.0 \pm 4.6 \pm 4.2 \pm 5.1$
$B_s \rightarrow (D_s \pi)_P K^*(892)$	$6.8 \pm 1.5 \pm 2.4 \pm 2.3$	$36.0 \pm 8.0 \pm 10.9 \pm 13.2$
$B_s \rightarrow (D_s K)_P \rho(770)$		$9.7 \pm 4.0 \pm 4.2 \pm 3.5$
Sum	$99.3 \pm 4.7 \pm 7.2 \pm 4.0$	$135.9 \pm 12.9 \pm 13.5 \pm 11.7$

919 12 Systematic uncertainties

920 The systematic uncertainties on the measured observables are summarized in Table 12.3 for
921 the decay-time fit to $B_s \rightarrow D_s \pi\pi\pi$, in Table 12.4 for the decay-time fit to $B_s \rightarrow D_s K\pi\pi$
922 and in Table 12.5 for the full time-dependent amplitude fit to $B_s \rightarrow D_s K\pi\pi$ decays. A
923 description of each systematic effect is given in the following subsections starting with the
924 ones common to all fits. Afterwards, systematic effect specific to the amplitude description
925 are discussed. Systematic uncertainties estimated from pseudo-experiments (toys) are
926 calculated relative to the statistical error.

927 12.1 Fit bias

928 Pseudo-experiments are performed, where a signal toy sample of the same size as the
929 number of observed signal data events is generated according to the nominal fit model and
930 subsequently fitted with the same model. The means of the pull distributions are taken
931 as systematic uncertainties of the fit parameters. The width of the pull distributions are
932 compatible with unity.

933 As the determination of the mixing frequency is a high precision measurement, a
934 closure test is performed to further validate the fit procedure. A fit to the decay-time
935 distribution of the high-statistics fully simulated signal $B_s \rightarrow D_s \pi\pi\pi$ and $B_s \rightarrow D_s K\pi\pi$
936 candidates (using the **TRUEID** of the candidates for the tagging information) is performed
937 to extract the mixing frequency resulting in $\Delta m_s = 17.8027 \pm 0.0009 \text{ ps}^{-1}$ and $\Delta m_s =$
938 $17.8017 \pm 0.0009 \text{ ps}^{-1}$, respectively. The larger shift with respect to the generated value of
939 $\Delta m_s = 17.800 \text{ ps}^{-1}$ is assigned as additional systematic uncertainty (even though it could,
940 at least to some extent, be explained by statistical fluctuations of the MC sample).

941 12.2 Background subtraction

942 The statistical subtraction of the residual background [43], left after the full selection,
943 relies on the correct description of the invariant B_s^0 mass distribution. Since the choice of
944 signal and background models is not unique, alternative parameterizations are tested:

- 945 • The Johnson's SU function which is used as nominal signal model is replaced by the
946 sum of two Crystal Ball functions [48].
- 947 • For the combinatorial background, the nominal second order polynomial is replaced
948 by an exponential function.
- 949 • For the description of the partially reconstructed background, a combination of the
950 **RooHILLdini** and **RooHORNsdini** model [49] is used instead of the nominal model of
951 three bifurcated gaussians.
- 952 • For the shape of the mis-ID background, the nominal approach is to use a simulated
953 sample of $B_s^0 \rightarrow D_s^- \pi^+ \pi^- \pi^+$ or $B_s^0 \rightarrow D_s^{*-} \pi^+ \pi^- \pi^+$ decays and flip the mass
954 hypothesis of the π^+ with the higher misidentification probability (see Sec. 5).
955 Two alternative approaches are considered: we flip the mass hypothesis of the π^+
956 candidate with the lower probability of being misidentified; we randomly flip the
957 mass hypothesis of a π^+ candidate. To account for the systematic of the $\pi \rightarrow K$
958 fake rate, we vary the default PIDK cut ($\text{PIDK} > 10$) by ± 2 when calculating the
959 misID weights from **PIDCalib**.

In total 10 (7) different combinations of the modifications discussed above are tested
 for the fit to the $D_s K\pi\pi$ ($D_s \pi\pi\pi$) mass distribution. For each case, new signal **sWeights**
 are calculated and the **sFits** to data are repeated. The sample variance of the obtained
 differences to the nominal fit value are used as systematic uncertainty due to the background
 modelling.

The subtraction of the background via the sPlot technique relies on the assumption of
 no correlation between the reconstructed mass and the observables that are used in the
 final fit. To assess the impact of ignoring the small correlation between reconstructed mass
 and decay-time ($\rho \approx -0.04$) observed for the combinatorial background, we perform a toy
 study including signal and background candidates. The two-dimensional reconstructed
 mass vs. decay-time distribution for background candidates, shown in Fig. 12.1, is taken
 from a (same-sign) $D_s^+ K^+ \pi^+ \pi^-$ data sample. For simplicity, a flat phase-space distribution
 is assumed for the background. The toy study including the small correlation in the
 generation of the background candidates is contrasted to one where uncorrelated masses
 and decay-times are generated. The difference of the pull means is assigned as systematic
 for each fit parameter.

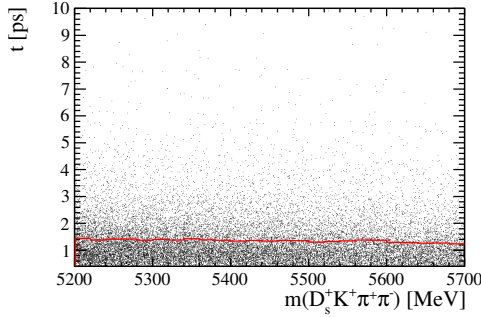


Figure 12.1: Scatter plot of reconstructed mass against decay-time for (same-sign) $D_s^+ K^+ \pi^+ \pi^-$ candidates. The average decay-time in a given mass bin is overlaid in red.

12.3 Decay-time acceptance

The systematic uncertainty related to the decay-time efficiency as well as Γ_s and $\Delta\Gamma_s$ are
 studied simultaneously. We generate toys in the nominal configuration and fit back in
 both this nominal configuration and a configuration in which we have randomized the
 acceptance parameters together with Γ_s and $\Delta\Gamma_s$ within their uncertainties. For each toy,
 a pull is calculated by dividing the difference between the fitted values of the nominal
 and shifted configurations by the uncertainty in the nominal toy. We add the bias in the
 mean of this pull to its width, in quadrature, in order to arrive at the final systematic
 uncertainty.

To improve the coverage of the multi-dimensional parameter space, a Cholesky decom-
 position [50] is used to generate a set of uncorrelated vectors from the covariance matrix
 $\text{cov}(\lambda_i, \lambda_j)$, where the vector λ includes the parameters Γ_s , $\Delta\Gamma_s$ and the $N = 4$ spline
 coefficients for each category of the simultaneous fit. The correlations between Γ_s ($\Delta\Gamma_s$)
 and the spline coefficients are measured by rerunning the acceptance fits described in
 Sec. 7.2 with the values of Γ_s ($\Delta\Gamma_s$) varied by $\pm 1\sigma$ and measuring the shift in the spline
 coefficients as a fraction of their uncertainty. For the correlation between Γ_s and $\Delta\Gamma_s$ we
 use the HFLAV value [35].

993 12.4 Decay-time resolution and tagging

994 To study systematic effects originating from the scaling of the decay-time error estimate,
 995 two different approaches which either slightly overestimate or underestimate the resolution
 996 are used:

- 997 • A double Gaussian is fit to the decay-time distributions of fake B_s^0 candidates, but
 998 only the width of the core Gaussian is considered to represent the time resolution in
 999 the respective bin. Therefore the resolution is slightly underestimated in this case.
- 1000 • A single Gaussian is fit to the decay-time distributions of fake B_s^0 candidates in a
 1001 wide range of $[-3\sigma_t : 1.5\sigma_t]$. Due to the tails of the distribution, which broaden the
 1002 width of the Gaussian function, this method slightly overestimates the decay-time
 1003 resolution.

1004 For each case, a new scaling function is derived:

$$\sigma_{eff,Data,16}^{core-Gauss}(\sigma_t) = (6.8 \pm 1.9) \text{ fs} + (0.797 \pm 0.050) \sigma_t \quad (12.1)$$

$$\sigma_{eff,Data,16}^{single-Gauss}(\sigma_t) = (10.1 \pm 1.5) \text{ fs} + (0.950 \pm 0.039) \sigma_t \quad (12.2)$$

$$\sigma_{eff,Data,17}^{core-Gauss}(\sigma_t) = (0.1 \pm 1.5) \text{ fs} + (0.957 \pm 0.037) \sigma_t \quad (12.3)$$

$$\sigma_{eff,Data,17}^{single-Gauss}(\sigma_t) = (5.6 \pm 1.2) \text{ fs} + (1.012 \pm 0.031) \sigma_t \quad (12.4)$$

1005 They are compared to the nominal result in Fig. 12.2. In addition, the impact of performing
 1006 a three-dimensional reweighting in $p_T(B_s)$, σ_t and $\chi^2_{FD}(D_s)$ (as done for the decay-time
 1007 bias extraction, see Section 6.3) is studied. The resulting variation from the baseline
 1008 is much smaller than with the two alternative approaches discussed above and thus no
 1009 additional systematic is assigned.

1010 Due to the high correlation between the decay-time resolution and the tagging calibration,
 1011 their systematic uncertainty has to be studied simultaneously. First, the decay-time
 1012 fits to $B_s \rightarrow D_s \pi \pi \pi$ data are repeated using the alternative decay-time error scaling
 1013 functions. New tagging calibration parameters are obtained which are then used (together
 1014 with the respective decay-time error scaling function) in the fits to $B_s \rightarrow D_s K \pi \pi$ data to
 1015 define the Gaussian-constraints as discussed in Sec. 10. For the width of the Gaussians
 1016 only the statistical error of the tagging calibration parameters are used since systematic
 1017 uncertainties (except the systematic arising from the decay-time resolution which is already
 1018 included by the procedure described above) are found to be negligible, see Table 12.3.
 1019 Finally, we take the biggest change in fit central value as the systematic for each parameter
 1020 of the $B_s \rightarrow D_s K \pi \pi$ fits.

1021 A systematic uncertainty due to the limited knowledge of the decay-time bias which is
 1022 fixed in the fit is evaluated by means of a toy study, where the value is randomized within
 1023 its uncertainty. This source of systematic uncertainty is only relevant for the measurement
 1024 of Δm_s (to which it contributes a systematic error of 0.0058 ps^{-1}), while the impact on
 1025 all parameters extracted from the fit to $B_s \rightarrow D_s K \pi \pi$ data is negligible.

1026 The procedure of accounting for the VELO misalignment with a constant decay-time
 1027 bias in the resolution model (*i.e.* ignoring the event-per-event dependency on the decay-
 1028 time error estimate) is validated with a $B_s^0 \rightarrow D_s \pi$ MC sample processed with a realistic
 1029 VELO misalignment. A fit to the decay-time distribution (using the TRUEID of the

1033 candidates for the tagging information) is performed to extract Δm_s , where a constant
 1034 decay-time bias is included in the resolution model. The result differs by 0.003 ps^{-1} from
 1035 the result obtained by fitting simulated $B_s^0 \rightarrow D_s\pi$ candidates processed without VELO
 1036 misalignment. This difference is added as additional systematic uncertainty on Δm_s due
 1037 to the decay-time bias correction method.

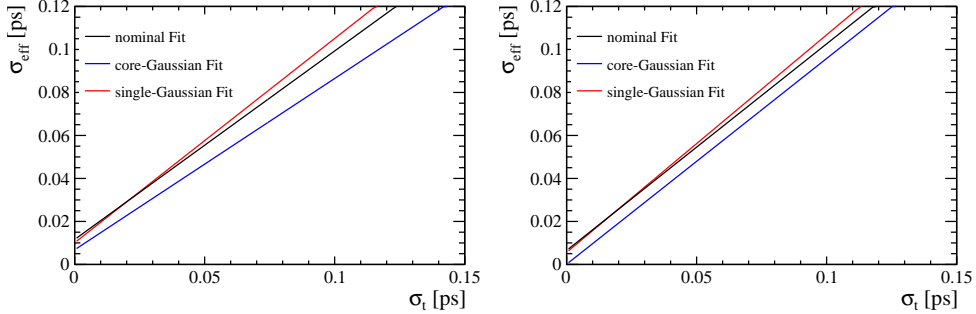


Figure 12.2: The measured resolution scaling function of the per-event decay time error estimate σ_t for fake B_s candidates (Run-II data) for (black line) the nominal scaling, (blue line) only using the narrow gaussian width of the double gaussian fit model or (red line) when determining the resolution using a single gaussian model. Data taken in (left) 2016 and (right) 2017.

1038 12.5 Production, detection asymmetries and mixing frequency

1039 The systematic from the production, detection asymmetries and Δm_s (in case of $B_s \rightarrow$
 1040 $D_s K\pi\pi$ decays) which are fixed in the fit are evaluated by means of a toy study similar
 1041 to the procedure performed for the time-acceptance. The parameters are assumed to be
 1042 uncorrelated.

1043 12.6 Multiple candidates

1044 The fraction of events with multiple candidates has been found to be very small, it is
 1045 1.6% for $D_s K\pi\pi$ and 1.5% for $D_s\pi\pi\pi$. Thus the nominal result is obtained keeping all
 1046 candidates, while a systematic uncertainty is assigned by repeating the fit randomly
 1047 keeping only one candidate when multiple ones are founds. No shifts in the fit central
 1048 values are observed.

1049 12.7 Length and momentum scales

1050 The uncertainty on the LHCb length scale is estimated to be at most 0.020% [51, 52],
 1051 which translates directly in an uncertainty on Δm_s of 0.020% with other parameters
 1052 being unaffected. The momentum scale uncertainty is at most 0.022%. In the fit to
 1053 $B_s \rightarrow D_s K\pi\pi$ data, the scale uncertainties are then implicitly included in the systematic
 1054 due to Δm_s which we vary within its uncertainties, see above.

1055 12.8 Phase space acceptance

1056 For the phase space acceptance we rely on simulated data. The integration error due to
1057 the limited size of the MC sample used to normalize the signal PDF is below 0.2% and
1058 thus negligible small.

1059 To assess the uncertainty due to possible data-simulation differences, we determine
1060 alternative phase space efficiencies by varying the selection requirements on quantities
1061 that are expected not to be well described by the simulation. In particular, we consider
1062 the following variations:

- 1063 • No BDT cut is applied
- 1064 • A tighter BDT requirement is used ($\text{BDTG} > 0.6$)
- 1065 • No reweighting is applied
- 1066 • Instead of the PID responses obtained from the `PIDCorr` tool, we use the `PIDGen`
1067 tool to resample the PID variables [34]
- 1068 • The raw MC PID variables are used
- 1069 • Candidates with `BKGCAT`= 60 are removed
- 1070 • A tight cut on the B_s transverse momentum is applied ($p_T > 10 \text{ GeV}$)
- 1071 • We require `L0Hadron-TOS` instead of (`L0Hadron-TOS` || `L0Global-TIS`)
- 1072 • We require `L0Global-TIS` instead of (`L0Hadron-TOS` || `L0Global-TIS`)

1073 We assign the sample variance of the fitted values using the alternative phase space
1074 acceptances as systematic.

1075 It is assumed that the phase space acceptance is independent of the decay-time. This
1076 assumption is tested by using only simulated candidates within specific decay-time intervals
1077 to calculate the MC normalization integrals described in Sec. 7.3. Four approximately
1078 equally populated decay-time bins are chosen and the sample variance of the fitted values
1079 is assigned as systematic.

1080 12.9 Resonance description

1081 The following alternative line shape parameterizations are considered as part of the
1082 systematic studies:

- 1083 • The Lass description for the $K\pi$ S -wave is replaced by a more general model
1084 (Glass [53, 54])
- 1085 • The Gounaris-Sakurai description for the $\rho(770)$ is replaced by a relativistic Breit-
1086 Wigner propagator (Equation 2.16)
- 1087 • The ω contribution to the decay channel $K_1(1270) \rightarrow K \rho(770)/\omega$ is set to zero
- 1088 • For the decay channel $K^*(1410) \rightarrow K \rho(770)$, we include $\rho(770) - \omega$ mixing with a
1089 relative magnitude and phase determined from data

- 1090 • Instead of taking the energy-dependent widths of the three-body resonances from
 1091 Refs. [12, 23], we derive them from Equation 2.17 taking only the dominant $K\pi\pi$
 1092 decay mode into account

1093 The data fits are repeated for each alternative model and the RMS of the central values
 1094 are taken as systematic uncertainties.

1095 The uncertainties due to fixed masses and widths of resonances are evaluated from
 1096 toys where we vary them one-by-one within their quoted errors. In our nominal fit, the
 1097 Blatt-Weisskopf radial parameter is set to $r_{BW} = 1.5 \text{ GeV}^{-1}$. Again, toys are generated
 1098 according to this nominal configuration and then fitted whereby the radial parameter is
 1099 uniformly varied within the interval $[0, 3] \text{ GeV}^{-1}$.

1100 12.10 Alternative amplitude models

1101 We tested several modifications of the LASSO model to assign an additional model
 1102 uncertainty to the measured observables r, δ and $\gamma - 2\beta_s$ as well as to the measured
 1103 masses and widths of the $K_1(1400)$ and $K^*(1410)$ resonances. The amplitude coefficients
 1104 are by definition parameters of a given model which is why we do not evaluate a model
 1105 uncertainty for them. The fit results of the following alternative models (Alt. 1 - Alt. 12)
 1106 are summarized in Tables 12.1 and 12.2.

- 1107 • All amplitudes selected by Stage 1 of the model selection are included for both $b \rightarrow c$ and
 1108 $b \rightarrow u$ transitions (Alt. 1)
- 1109 • The decay channel $K_1(1270)[D] \rightarrow K^*(892)\pi$, where the $K^*(892)\pi$ system is in relative a
 1110 D-wave state, is added (Alt. 2)
- 1111 • The decay channel $K_1(1400) \rightarrow K\rho(770)$ is added (Alt. 12)
- 1112 • The decay channels $K(1460) \rightarrow K\rho(770)$ and $K(1460) \rightarrow K\sigma$ are added (Alt. 3)
- 1113 • The decay channels $K^*(1680) \rightarrow K\rho(770)$ and $K^*(1680) \rightarrow K^*(892)\pi$ are added (Alt. 9)
- 1114 • The decay channel $K_2(1770) \rightarrow K^*(892)\pi$ is added (Alt. 10)
- 1115 • The amplitude $B_s \rightarrow (D_s K)_P \rho(770)$ is replaced by $B_s \rightarrow (D_s K)_S \rho(770)$ (Alt. 11)
- 1116 • Higher orbital angular momentum states are added for the amplitudes: $B_s \rightarrow (D_s \pi)_P K^*(892)$ and $B_s \rightarrow (D_s K)_P \rho(770)$ (Alt. 4 and Alt. 5)
- 1117 • The amplitudes $B_s \rightarrow (D_s K)\sigma$, $B_s \rightarrow (D_s K)f_0(980)$, $B_s \rightarrow (D_s K)f_2(1270)$ and
 1119 $B_s \rightarrow (D_s K)f_0(1370)$ are added in different combinations and angular momentum
 1120 configurations (Alt. 6, Alt. 7 and Alt. 8)
- 1121 • The decay channels $K_2^*(1430) \rightarrow K\rho(770)$ and $K_2^*(1430) \rightarrow K^*(892)\pi$ are added (not
 1122 used)
- 1123 • The amplitudes $B_s \rightarrow (D_s \pi)_P K_0^*(1430)$ and $B_s \rightarrow (D_s K)_S K_2^*(1430)$ are added (not
 1124 used)
- 1125 • A flat non-resonant $B_s \rightarrow D_s K\pi\pi$ component is added (not used)

₁₁₂₆ In total 15 different sets of amplitudes are fitted. In some cases, the fit fractions of
₁₁₂₇ additionally added amplitudes turn out to be exactly zero. These model are effectively
₁₁₂₈ not distinguishable from the baseline LASSO model and are not considered further. From
₁₁₂₉ the remaining 12 models, we compute the sample variance for each observable and take it
₁₁₃₀ as model uncertainty.

Table 12.1: Fit fractions in percent for the baseline and several alternative amplitude models (Alt. 1 - Alt. 6). Resonance parameters and the physical observables $r, \kappa, \delta, \gamma - 2\beta_s$ are also given. The values of the physical observables are given relative to the baseline result. The uncertainties are statistical only.

	Baseline	Alt.1	Alt.2	Alt.3	Alt.4	Alt.5	Alt.6
$B_s \rightarrow D_s (K_1(1270) \rightarrow K^*(892) \pi)$	6.2	6.5	6.7	5.2	5.4	6.1	6.0
$B_s \rightarrow D_s (K_1(1270)[D] \rightarrow K^*(892) \pi)$			1.3				
$B_s \rightarrow D_s (K_1(1270) \rightarrow K \rho(770))$	12.3	10.3	9.8	9.4	13.9	11.2	12.9
$B_s \rightarrow D_s (K_1(1270) \rightarrow K \rho(1450))$							
$B_s \rightarrow D_s (K_1(1270) \rightarrow K_0^*(1430) \pi)$	3.3	2.5	2.3	2.6	3.5	2.8	3.5
$B_s \rightarrow D_s (K_1(1400) \rightarrow K^*(892) \pi)$	47.9	54.3	53.5	58.8	47.0	53.7	43.7
$B_s \rightarrow D_s (K_1(1400) \rightarrow K \rho(770))$							
$B_s \rightarrow D_s (K^*(1410) \rightarrow K^*(892) \pi)$	15.9	15.0	15.6	15.7	17.6	15.7	16.1
$B_s \rightarrow D_s (K^*(1410) \rightarrow K \rho(770))$	6.5	5.5	6.2	6.3	6.5	6.5	6.6
$B_s \rightarrow D_s (K(1460) \rightarrow K^*(892) \pi)$		0.8					
$B_s \rightarrow D_s (K(1460) \rightarrow K \rho(770))$							
$B_s \rightarrow D_s (K(1460) \rightarrow K \sigma)$							
$B_s \rightarrow D_s (K^*(1680) \rightarrow K^*(892) \pi)$							
$B_s \rightarrow D_s (K^*(1680) \rightarrow K \rho(770))$							
$b \rightarrow c$							
$B_s \rightarrow (D_s \pi)_S K^*(892)$							
$B_s \rightarrow (D_s \pi)_P K^*(892)$		6.7	9.2	7.9	10.3	13.9	6.8
$B_s[P] \rightarrow (D_s \pi)_P K^*(892)$						0.1	
$B_s[D] \rightarrow (D_s \pi)_P K^*(892)$						0.9	
$B_s \rightarrow (D_s K)_S \sigma$							
$B_s \rightarrow (D_s K)_P \sigma$							
$B_s \rightarrow (D_s K)_S f_0(980)$							
$B_s \rightarrow (D_s K)_S f_2(1270)$							0.0
$B_s \rightarrow (D_s K)_P f_2(1270)$							
$B_s \rightarrow (D_s K)_S f_0(1370)$							
$B_s \rightarrow (D_s K)_S \rho(770)$							
$B_s \rightarrow (D_s K)_P \rho(770)$			0.7			0.1	
$B_s[P] \rightarrow (D_s K)_P \rho(770)$							
$B_s[D] \rightarrow (D_s K)_P \rho(770)$							
Sum	98.9	104.7	103.2	108.3	108.8	103.1	95.2
$b \rightarrow u$							
$B_s \rightarrow D_s (K_1(1270) \rightarrow K^*(892) \pi)$	15.0	20.9	21.0	18.2	11.5	19.1	13.8
$B_s \rightarrow D_s (K_1(1270)[D] \rightarrow K^*(892) \pi)$			4.0				
$B_s \rightarrow D_s (K_1(1270) \rightarrow K \rho(770))$	29.5	33.3	30.8	33.0	29.8	35.2	29.6
$B_s \rightarrow D_s (K_1(1270) \rightarrow K \rho(1450))$							
$B_s \rightarrow D_s (K_1(1270) \rightarrow K_0^*(1430) \pi)$	8.0	8.2	7.2	9.2	7.5	8.9	8.2
$B_s \rightarrow D_s (K_1(1400) \rightarrow K^*(892) \pi)$	15.5	29.5	21.2	22.1	23.5	15.4	19.6
$B_s \rightarrow D_s (K_1(1400) \rightarrow K \rho(770))$							
$B_s \rightarrow D_s (K^*(1410) \rightarrow K^*(892) \pi)$		2.2					
$B_s \rightarrow D_s (K^*(1410) \rightarrow K \rho(770))$		0.8					
$B_s \rightarrow D_s (K(1460) \rightarrow K^*(892) \pi)$	22.3	19.1	12.9	17.2	15.1	21.7	21.9
$B_s \rightarrow D_s (K(1460) \rightarrow K \rho(770))$				3.5			
$B_s \rightarrow D_s (K(1460) \rightarrow K \sigma)$				2.3			
$B_s \rightarrow D_s (K^*(1680) \rightarrow K^*(892) \pi)$							
$B_s \rightarrow D_s (K^*(1680) \rightarrow K \rho(770))$							
$B_s \rightarrow D_s (K_2(1770) \rightarrow K^*(892) \pi)$							
$B_s \rightarrow (D_s \pi)_S K^*(892)$							
$B_s \rightarrow (D_s \pi)_P K^*(892)$		37.6	16.3	23.1	17.3	61.2	29.3
$B_s[P] \rightarrow (D_s \pi)_P K^*(892)$						0.6	
$B_s[D] \rightarrow (D_s \pi)_P K^*(892)$						3.8	
$B_s \rightarrow (D_s K)_S \sigma$							
$B_s \rightarrow (D_s K)_P \sigma$							
$B_s \rightarrow (D_s K)_S f_0(980)$							
$B_s \rightarrow (D_s K)_S f_2(1270)$							0.2
$B_s \rightarrow (D_s K)_P f_2(1270)$							
$B_s \rightarrow (D_s K)_S f_0(1370)$							
$B_s \rightarrow (D_s K)_S \rho(770)$							
$B_s \rightarrow (D_s K)_P \rho(770)$	8.4	8.2	4.8	13.3	8.4	12.6	7.5
$B_s[P] \rightarrow (D_s K)_P \rho(770)$						0.9	
$B_s[D] \rightarrow (D_s K)_P \rho(770)$						0.8	
Sum	136.4	138.7	124.9	136.0	161.5	143.8	142.6
$m_{K_1(1400)} [\text{MeV}]$	1397	1389	1389	1394	1410	1392	1403
$\Gamma_{K_1(1400)} [\text{MeV}]$	205	210	207	220	222	207	205
$m_{K^*(1410)} [\text{MeV}]$	1432	1435	1436	1429	1435	1428	1432
$\Gamma_{K^*(1410)} [\text{MeV}]$	345	351	348	347	360	346	347
r	0.50	0.46	0.48	0.49	0.51	0.49	0.51
κ	0.52	0.61	0.54	0.30	0.53	0.51	0.51
$\delta [{}^\circ]$	46	58	57	46	42	55	45
$\gamma - 2\beta_s [{}^\circ]$	61	70	57	60	54	67	62

Table 12.2: Fit fractions in percent for several alternative amplitude models (Alt. 7 - Alt. 12). Resonance parameters and the physical observables $r, \kappa, \delta, \gamma - 2\beta_s$ are also given. The values of the physical observables are given relative to the baseline result. The uncertainties are statistical only.

		Alt.7	Alt.8	Alt.9	Alt.10	Alt.11	Alt.12
$B_s \rightarrow D_s (K_1(1270) \rightarrow K^*(892) \pi)$ & 6.9 & 7.6 & 6.1 & 6.7 & 8.1 & 6.3 $B_s \rightarrow D_s (K_1(1270)[D] \rightarrow K^*(892) \pi)$ $B_s \rightarrow D_s (K_1(1270) \rightarrow K \rho(770))$ & 13.8 & 12.8 & 13.2 & 11.0 & 14.7 & 14.9 $B_s \rightarrow D_s (K_1(1270) \rightarrow K \rho(1450))$ $B_s \rightarrow D_s (K_1(1270) \rightarrow K_0^*(1430) \pi)$ & 3.8 & 3.1 & 3.3 & 3.3 & 4.0 & 3.3 $B_s \rightarrow D_s (K_1(1400) \rightarrow K^*(892) \pi)$ & 47.8 & 45.7 & 49.8 & 52.6 & 46.4 & 49.9 $B_s \rightarrow D_s (K_1(1400) \rightarrow K \rho(770))$ $B_s \rightarrow D_s (K_1(1400) \rightarrow K \rho(770))$ & 0.6 $B_s \rightarrow D_s (K^*(1410) \rightarrow K^*(892) \pi)$ & 15.4 & 15.5 & 18.8 & 15.2 & 15.5 & 15.9 $B_s \rightarrow D_s (K^*(1410) \rightarrow K \rho(770))$ & 5.8 & 6.0 & 5.2 & 6.3 & 6.2 & 6.3 $B_s \rightarrow D_s (K(1460) \rightarrow K^*(892) \pi)$ $B_s \rightarrow D_s (K(1460) \rightarrow K \rho(770))$ $B_s \rightarrow D_s (K(1460) \rightarrow K \sigma)$ $B_s \rightarrow D_s (K^*(1680) \rightarrow K^*(892) \pi)$ & 0.8 $B_s \rightarrow D_s (K^*(1680) \rightarrow K \rho(770))$ & 0.9 $b \rightarrow c$ $B_s \rightarrow D_s (K_2(1770) \rightarrow K^*(892) \pi)$ & 0.7 $B_s \rightarrow (D_s \pi)_S K^*(892)$ $B_s \rightarrow (D_s \pi)_P K^*(892)$ & 7.8 & 5.7 & 7.7 & 7.3 & 7.1 & 6.5 $B_s [P] \rightarrow (D_s \pi)_P K^*(892)$ $B_s [D] \rightarrow (D_s \pi)_P K^*(892)$ $B_s \rightarrow (D_s K)_S \sigma$ & 1.6 & 0.4 $B_s \rightarrow (D_s K)_P \sigma$ & 2.9 $B_s \rightarrow (D_s K)_S f_0(980)$ $B_s \rightarrow (D_s K)_S f_2(1270)$ $B_s \rightarrow (D_s K)_P f_2(1270)$ $B_s \rightarrow (D_s K)_S f_0(1370)$ $B_s \rightarrow (D_s K)_S \rho(770)$ $B_s \rightarrow (D_s K)_P \rho(770)$ $B_s [P] \rightarrow (D_s K)_P \rho(770)$ $B_s [D] \rightarrow (D_s K)_P \rho(770)$ Sum & 105.7 & 97.4 & 105.8 & 103.1 & 102.0 & 103.8 <hr/> $B_s \rightarrow D_s (K_1(1270) \rightarrow K^*(892) \pi)$ & 9.7 & 14.3 & 14.4 & 19.3 & 8.0 & 13.3 $B_s \rightarrow D_s (K_1(1270)[D] \rightarrow K^*(892) \pi)$ $B_s \rightarrow D_s (K_1(1270) \rightarrow K \rho(770))$ & 19.3 & 24.1 & 31.3 & 31.7 & 14.5 & 31.5 $B_s \rightarrow D_s (K_1(1270) \rightarrow K \rho(1450))$ $B_s \rightarrow D_s (K_1(1270) \rightarrow K_0^*(1430) \pi)$ & 5.3 & 5.9 & 7.8 & 9.5 & 4.0 & 7.1 $B_s \rightarrow D_s (K_1(1400) \rightarrow K^*(892) \pi)$ & 6.8 & 14.3 & 12.0 & 18.7 & 8.9 & 15.7 $B_s \rightarrow D_s (K_1(1400) \rightarrow K \rho(770))$ $B_s \rightarrow D_s (K^*(1410) \rightarrow K^*(892) \pi)$ $B_s \rightarrow D_s (K^*(1410) \rightarrow K \rho(770))$ $B_s \rightarrow D_s (K(1460) \rightarrow K^*(892) \pi)$ & 29.4 & 27.0 & 23.1 & 22.6 & 28.9 & 22.8 $B_s \rightarrow D_s (K(1460) \rightarrow K \rho(770))$ $B_s \rightarrow D_s (K(1460) \rightarrow K \sigma)$ $B_s \rightarrow D_s (K^*(1680) \rightarrow K^*(892) \pi)$ $b \rightarrow u$ $B_s \rightarrow D_s (K^*(1680) \rightarrow K \rho(770))$ $B_s \rightarrow D_s (K_2(1770) \rightarrow K^*(892) \pi)$ & 0.8 $B_s \rightarrow (D_s \pi)_S K^*(892)$ $B_s \rightarrow (D_s \pi)_P K^*(892)$ & 45.5 & 40.9 & 39.3 & 27.0 & 46.6 & 35.3 $B_s [P] \rightarrow (D_s \pi)_P K^*(892)$ $B_s [D] \rightarrow (D_s \pi)_P K^*(892)$ $B_s \rightarrow (D_s K)_S \sigma$ & 0.3 & 0.7 $B_s \rightarrow (D_s K)_P \sigma$ & 0.6 $B_s \rightarrow (D_s K)_S f_0(980)$ $B_s \rightarrow (D_s K)_S f_2(1270)$ $B_s \rightarrow (D_s K)_P f_2(1270)$ $B_s \rightarrow (D_s K)_S f_0(1370)$ $B_s \rightarrow (D_s K)_S \rho(770)$ $B_s \rightarrow (D_s K)_P \rho(770)$ & 4.6 & 8.4 & 8.6 & 7.9 & 4.1 & 7.3 $B_s [P] \rightarrow (D_s K)_P \rho(770)$ $B_s [D] \rightarrow (D_s K)_P \rho(770)$ Sum & 121.6 & 136.5 & 136.5 & 137.5 & 115.0 & 133.1 <hr/> $m_{K_1(1400)} [\text{MeV}]$ & 1401 & 1393 & 1399 & 1394 & 1400 & 1393 $\Gamma_{K_1(1400)} [\text{MeV}]$ & 195 & 199 & 200 & 208 & 194 & 205 $m_{K^*(1410)} [\text{MeV}]$ & 1444 & 1438 & 1413 & 1432 & 1435 & 1433 $\Gamma_{K^*(1410)} [\text{MeV}]$ & 329 & 342 & 400 & 351 & 337 & 346 r & 0.44 & 0.46 & 0.49 & 0.46 & 0.46 & 0.49 κ & 0.46 & 0.51 & 0.51 & 0.54 & 0.56 & 0.44 $\delta [\circ]$ & 34 & 49 & 47 & 49 & 34 & 44 $\gamma - 2\beta_s [\circ]$ & 54 & 69 & 57 & 68 & 51 & 61							

Table 12.3: Systematic uncertainties on the fit parameters of the fit to $B_s \rightarrow D_s\pi\pi$ data in units of statistical standard deviations.

Fit Parameter	Fit-bias	Closure	Bkg.	Correlations	Acceptance	Resolution	Decay-time bias	VELO-Misalign.	Asymmetries	Mon./z-Scale	Total
p_0^{OS} Run-I	0.05	0.09	0.03	0.01	1.00	0.02			0.00		1.00
p_1^{OS} Run-I	0.01	0.13	0.06	0.01	1.04	0.02			0.01		1.05
Δp_0^{OS} Run-I	0.14	0.03	0.03	0.00	0.02	0.01			0.15		0.21
Δp_1^{OS} Run-I	0.07	0.06	0.16	0.00	0.03	0.01			0.15		0.24
ϵ_{tag}^{OS} Run-I	0.06	0.17	0.12	0.00	0.00	0.00			0.01		0.22
$\Delta \epsilon_{tag}^{OS}$ Run-I	0.04	0.01	0.05	0.00	0.06	0.02			0.01		0.09
p_0^{SS} Run-I	0.03	0.03	0.15	0.01	0.56	0.02			0.00		0.58
p_1^{SS} Run-I	0.10	0.03	0.04	0.01	0.60	0.01			0.01		0.61
Δp_0^{SS} Run-I	0.04	0.01	0.07	0.00	0.00	0.00			0.10		0.13
Δp_1^{SS} Run-I	0.03	0.04	0.04	0.00	0.01	0.00			0.12		0.14
ϵ_{tag}^{SS} Run-I	0.02	0.02	0.10	0.00	0.00	0.00			0.01		0.11
$\Delta \epsilon_{tag}^{SS}$ Run-I	0.04	0.03	0.02	0.00	0.04	0.03			0.01		0.07
p_0^{OS} Run-II	0.02	0.20	0.01	0.02	0.97	0.04			0.00		0.99
p_1^{OS} Run-II	0.02	0.08	0.10	0.01	0.60	0.04			0.00		0.61
Δp_0^{OS} Run-II	0.07	0.08	0.13	0.00	0.22	0.01			0.00		0.27
Δp_1^{OS} Run-II	0.02	0.03	0.16	0.00	0.08	0.01			0.00		0.18
ϵ_{tag}^{OS} Run-II	0.01	0.16	0.04	0.00	0.11	0.00			0.00		0.20
$\Delta \epsilon_{tag}^{OS}$ Run-II	0.05	0.05	0.10	0.00	0.03	0.03			0.00		0.13
p_0^{SS} Run-II	0.10	0.06	0.05	0.01	0.61	0.02			0.00		0.62
p_1^{SS} Run-II	0.01	0.07	0.06	0.02	0.63	0.04			0.00		0.64
Δp_0^{SS} Run-II	0.07	0.02	0.01	0.00	0.04	0.01			0.00		0.09
Δp_1^{SS} Run-II	0.11	0.05	0.14	0.00	0.04	0.01			0.00		0.19
ϵ_{tag}^{SS} Run-II	0.03	0.03	0.09	0.00	1.68	0.00			0.00		1.68
$\Delta \epsilon_{tag}^{SS}$ Run-II	0.01	0.03	0.01	0.00	0.21	0.03			0.00		0.21
A_P Run-II	0.04	0.02	0.17	0.00	0.19	0.03			0.01		0.26
Δm_s	0.01	0.32	0.11	0.02	0.00	0.13	0.69	0.36	0.02	0.67	1.09

Table 12.4: Systematic uncertainties on the fit parameters of the phase-space integrated fit to $B_s \rightarrow D_s K\pi\pi$ data in units of statistical standard deviations.

Fit Parameter	Fit bias	Background	Correlations	Acceptance	Resolution	Decay-time bias	Asymmetries	Δm_s	Total
C	0.15	0.03	0.06	0.11	0.04	0.15	0.04	0.06	0.26
D	0.00	0.18	0.10	0.31	0.05	0.01	0.00	0.01	0.38
\bar{D}	0.05	0.20	0.13	0.28	0.04	0.02	0.00	0.01	0.37
S	0.05	0.01	0.06	0.06	0.04	0.07	0.07	0.10	0.18
\bar{S}	0.07	0.02	0.03	0.05	0.04	0.05	0.05	0.10	0.16

Table 12.5: Systematic uncertainties on the fit parameters of the full time-dependent amplitude fit to $B_s \rightarrow D_s K\pi\pi$ data in units of statistical standard deviations.

Fit Parameter	Fit bias	Background	Correlations	Time-Acc.	Resolution	Decay-time bias	Asymmetries	Δm_s	Phsp-Acc.	Acc. Factor.	Lineshapes	Resonances m, Γ	Form-Factors	Ampl. Model	Total
$B_s \rightarrow D_s (K_1(1270) \rightarrow K^*(892)\pi)$ Mag	0.10	0.12	0.01	0.03	0.01	0.00	0.01	0.07	0.44	0.42	0.21	0.46	0.46	0.82	
$B_s \rightarrow D_s (K_1(1270) \rightarrow K^*(892)\pi)$ Phase	0.07	0.08	0.09	0.01	0.04	0.00	0.01	0.25	0.29	0.33	0.30	0.36	0.36	0.70	
$B_s \rightarrow D_s (K_1(1270) \rightarrow K_0^*(1430)\pi)$ Mag	0.04	0.25	0.26	0.01	0.01	0.00	0.00	0.06	0.36	1.11	0.11	0.18	0.18	1.25	
$B_s \rightarrow D_s (K_1(1270) \rightarrow K_0^*(1430)\pi)$ Phase	0.04	0.15	0.17	0.00	0.02	0.01	0.00	0.01	0.46	3.53	0.15	0.50	0.50	3.60	
$B_s \rightarrow D_s (K_1(1400) \rightarrow K^*(892)\pi)$ Mag($b \rightarrow c$)	0.13	0.51	0.05	0.04	0.25	0.04	0.03	0.09	0.48	1.00	1.67	0.55	1.18	2.46	
$B_s \rightarrow D_s (K_1(1400) \rightarrow K^*(892)\pi)$ Phase($b \rightarrow c$)	0.14	0.14	0.13	0.01	0.08	0.02	0.01	0.02	0.21	0.25	0.36	0.21	0.32	0.67	
$B_s \rightarrow D_s (K_1(1400) \rightarrow K^*(892)\pi)$ Mag($b \rightarrow u$)	0.10	0.28	0.00	0.04	0.04	0.02	0.03	0.10	0.22	0.07	0.29	0.18	0.62	0.82	
$B_s \rightarrow D_s (K_1(1400) \rightarrow K^*(892)\pi)$ Phase($b \rightarrow u$)	0.02	0.10	0.28	0.05	0.04	0.03	0.03	0.11	0.29	0.47	0.68	0.24	0.35	1.02	
$B_s \rightarrow D_s (K^*(1410) \rightarrow K^*(892)\pi)$ Mag($b \rightarrow c$)	0.08	0.11	0.18	0.02	0.05	0.00	0.02	0.05	0.63	0.67	0.34	0.16	0.47	1.12	
$B_s \rightarrow D_s (K^*(1410) \rightarrow K^*(892)\pi)$ Phase($b \rightarrow c$)	0.35	0.15	0.00	0.02	0.07	0.02	0.01	0.12	0.30	0.57	0.22	0.80	0.80	1.12	
$B_s \rightarrow D_s (K^*(1410) \rightarrow K_\rho(770))$ Mag	0.35	0.13	0.00	0.01	0.01	0.00	0.00	0.01	0.07	0.41	0.44	0.09	0.26	0.76	
$B_s \rightarrow D_s (K^*(1410) \rightarrow K_\rho(770))$ Phase	0.18	0.24	0.19	0.00	0.01	0.01	0.00	0.01	0.15	0.25	0.32	0.09	0.21	0.61	
$B_s \rightarrow D_s (K(1460) \rightarrow K^*(892)\pi)$ Mag($b \rightarrow u$)	0.14	0.34	0.20	0.03	0.05	0.01	0.02	0.05	0.11	0.44	0.39	0.24	0.55	0.94	
$B_s \rightarrow D_s (K(1460) \rightarrow K^*(892)\pi)$ Phase($b \rightarrow u$)	0.13	0.16	0.30	0.03	0.08	0.02	0.02	0.05	0.42	0.60	0.38	0.36	0.36	0.98	
$B_s \rightarrow (D_s \pi)_P K^*(892)$ Mag($b \rightarrow c$)	0.03	0.29	0.26	0.02	0.07	0.02	0.01	0.03	0.23	0.44	0.98	0.14	0.67	1.35	
$B_s \rightarrow (D_s \pi)_P K^*(892)$ Phase($b \rightarrow c$)	0.20	0.34	0.25	0.01	0.09	0.02	0.01	0.01	0.34	0.47	0.64	0.12	0.35	1.05	
$B_s \rightarrow (D_s \pi)_P K^*(892)$ Mag($b \rightarrow u$)	0.14	0.14	0.28	0.04	0.09	0.02	0.02	0.08	0.37	0.27	0.88	0.29	0.66	1.28	
$B_s \rightarrow (D_s \pi)_P K^*(892)$ Phase($b \rightarrow u$)	0.24	0.27	0.10	0.03	0.11	0.02	0.02	0.03	0.28	0.51	0.87	0.16	0.34	1.18	
$B_s \rightarrow (D_s K)_P \rho(770)$ Mag($b \rightarrow u$)	0.35	0.22	0.00	0.03	0.02	0.02	0.02	0.05	0.21	0.16	0.50	0.26	0.51	0.91	
$B_s \rightarrow (D_s K)_P \rho(770)$ Phase($b \rightarrow u$)	0.12	0.58	0.00	0.02	0.04	0.01	0.02	0.05	0.11	0.40	0.39	0.33	0.57	1.06	
$m_{K_1(1400)}$	0.09	0.12	0.07	0.01	0.07	0.01	0.00	0.01	0.20	0.09	0.17	0.11	0.32	0.64	
$\Gamma_{K_1(1400)}$	0.01	0.12	0.22	0.01	0.01	0.01	0.01	0.16	0.27	0.42	0.12	0.40	0.57	0.91	
$m_{K^*(1410)}$	0.05	0.10	0.07	0.01	0.02	0.00	0.00	0.01	0.28	0.74	0.31	0.05	1.56	1.94	
$\Gamma_{K^*(1410)}$	0.25	0.13	0.18	0.00	0.02	0.00	0.00	0.01	0.31	0.15	0.04	1.38	0.69	1.62	
r	0.11	0.28	0.22	0.03	0.05	0.03	0.02	0.07	0.30	0.03	0.35	0.07	0.15	0.46	0.78
δ	0.19	0.10	0.17	0.04	0.07	0.03	0.05	0.11	0.10	0.09	0.30	0.03	0.11	0.55	0.72
$\gamma - 2\beta_s$	0.10	0.13	0.11	0.07	0.13	0.01	0.02	0.07	0.04	0.02	0.28	0.03	0.11	0.42	0.59

1131 13 Summary

1132 The B_s^0 oscillation frequency Δm_s is measured from the time-dependent fit to $B_s^0 \rightarrow D_s\pi\pi\pi$
 1133 data to be

$$\Delta m_s = 17.7537 \pm 0.0084 \pm 0.0092,$$

1134 where the errors are statistical and systematic, respectively. Table 13.1 summarizes the
 1135 values for the ratio of the $b \rightarrow u$ and $b \rightarrow c$ transition amplitudes (r) and their strong
 1136 (δ) and weak phase ($\gamma - 2\beta_s$) difference obtained from the phase-space integrated, as
 1137 well as the time-dependent amplitude fit to $B_s^0 \rightarrow D_s K\pi\pi$ data. Their comparison is
 1138 not so straightforward as the results are obtained from the same data set. We define a
 1139 measure of their compatibility as follows: For the statistical error we take the difference
 1140 of the statistical uncertainties of both fits: $\Delta\sigma_{stat} = \sigma_{stat}^{MI} - \sigma_{stat}^{Full}$, where σ_{stat}^{MI} is the
 1141 statistical uncertainty of the phase-space integrated (model-independent) fit and σ_{stat}^{Full}
 1142 is the statistical uncertainty of the full time-dependent amplitude fit. In the limit of
 1143 equal statistical uncertainties, $\Delta\sigma_{stat} = 0$, and the results should agree perfectly. For
 1144 the systematic error we assume that the model-dependent error (including resonance
 1145 line shapes, form factors and alternative amplitude models) of the full time-dependent
 1146 amplitude fit, σ_{model}^{Full} , is uncorrelated to the phase-space integrated results. The remaining
 1147 systematics (including time-acceptance, resolution, tagging, etc.) are assumed to be 100%
 1148 correlated such that their effect should cancel. Hence, the results should agree within
 1149 a spread given by: $\Delta\sigma = \sqrt{\Delta\sigma_{stat}^2 + (\sigma_{model}^{Full})^2}$. The physical parameters agree within a
 1150 range of 0.4 to 1.4 $\Delta\sigma$.

Table 13.1: Parameters determined from the two fits performed to the $B_s^0 \rightarrow D_s K\pi\pi$ data sample. Statistical and systematic uncertainties are combined.

Parameter	Phase-space integrated fit	Time-dependent amplitude fit	Difference [$\Delta\sigma$]
r	0.41 ± 0.10	0.50 ± 0.05	1.4
κ	0.65 ± 0.21	0.52 ± 0.11	0.8
δ [°]	40 ± 18	46 ± 18	0.6
$\gamma - 2\beta_s$ [°]	65 ± 21	61 ± 17	0.4

1151 A Parametrization of Amplitude Lineshapes

1152 Bugg model for σ resonance

1153 For the broad scalar resonance σ , the model from Bugg is used [55]:

$$T(s) = [M^2 - s - g_1^2 \frac{s - s_A}{M^2 - s_A} z(s) - iM\Gamma_{tot}(s)]^{-1}, \quad (1.1)$$

$$M\Gamma_1(s) = g_1^2 \frac{s - s_A}{M^2 - s_A} \rho_1(s), \quad (1.2)$$

$$g_1^2(s) = M(b_1 + b_2 s) \exp[-(s - M^2)A^{-1}], \quad (1.3)$$

$$j_1(s) = \frac{1}{\pi} [2 + \rho_1 \ln_e \frac{1 - \rho_1}{1 + \rho_1}], \quad (1.4)$$

$$z(s) = j_1(s) - j_1(M^2), \quad (1.5)$$

$$M\Gamma_2(s) = 0.6g_1^2(s) \frac{s}{M^2} \exp(-\alpha|s - 4m_K^2|) \rho_2(s), \quad (1.6)$$

$$M\Gamma_3(s) = 0.2g_1^2(s) \frac{s}{M^2} \exp(-\alpha|s - 4m_\eta^2|) \rho_3(s), \quad (1.7)$$

$$M\Gamma_4(s) = Mg_4 \frac{\rho_{4\pi}(s)}{\rho_{4\pi}(M^2)}, \quad (1.8)$$

$$\rho_2(s) = \sqrt{1 - 4m_\pi^2/s}, \quad (1.9)$$

$$\rho_{4\pi}(s) = 1.0[1 + \exp(7.082 - 2.845s)]^{-1}, \quad (1.10)$$

1154 where the numerical values for the parameters are [55] $M = 0.953 \text{ GeV}$, $b_1 = 1.302 \text{ GeV}$,
 1155 $b_2 = 0.340 \text{ GeV}^{-1}$, $A = 2.426 \text{ GeV}^2$, $g_{4\pi} = 0.011 \text{ GeV}$ and $s_A = 0.41m_\pi^2$.

1156 Model for $K\pi$ -S-wave

1157 The LASS parameterization is used to model the $K\pi$ S-wave contribution. It consists of
 1158 the $K_0^*(1430)$ resonance together with an effective range non-resonant component [56–58]:

$$T_{LASS}(s) = \frac{\sqrt{s}}{q \cot \delta_L - iq} + e^{2i\delta_L} \frac{m_0 \Gamma_0 \frac{m_0}{q_0}}{m_0^2 - s - i m_0 \Gamma_0 \frac{m_0}{\sqrt{s}} \frac{q}{q_0}} \quad (1.11)$$

1159 with $\cot \delta_L = \frac{1}{aq} + \frac{1}{2}rq$. We use the values for the scattering length $a = 2.07 \pm 0.1 \text{ GeV}$
 1160 and effective range parameter $r = 3.32 \pm 0.34 \text{ GeV}$ from Ref. [56, 57].

1161 For systematic studies, the GLASS shape is used:

$$T_{GLASS}(s) = F \sin(\phi_B) e^{i\phi_B} + R \sin(\phi_R) e^{i\phi_R} e^{2i\phi_B} \quad (1.12)$$

$$\phi_B = \psi_B + \tan^{-1} \left(\frac{2aq(s)}{2 + arq^2(s)} \right) \quad (1.13)$$

$$\phi_R = \psi_R + \tan^{-1} \left(\frac{m\Gamma(s)}{m_0^2 - s} \right), \quad (1.14)$$

1162 with $F = 0.62 \pm 0.04$, $\phi_F = -0.100 \pm 0.010$, $R = 1$, $\phi_R = 1.10 \pm 0.02$, $a = 0.224 \pm$
 1163 0.003 GeV^{-1} and $r = -15.01 \pm 0.13 \text{ GeV}^{-1}$.

₁₁₆₄ **Model for $\rho^0(770)$ resonance**

₁₁₆₅ We use the Gounaris-Sakurai parametrization for the $\rho(770)^0 \rightarrow \pi\pi$ propagator [59]:

$$T_{GS}(m) = \frac{1 + f(0)/m_0^2}{m_0^2 + f(m) - m^2 - i m_0 \Gamma(m)}, \quad (1.15)$$

₁₁₆₆ where $\Gamma(m)$ takes on the same form as in Eq. 2.16 and the function $f(m)$ is defined as

$$f(m) = \Gamma_0 \frac{m_0^2}{q_0^3} \left[q^2 (h(m) - h(m_0)) + (m^2 - m_0^2) q_0^2 \frac{dh}{dm} \Big|_{m_0} \right] \quad (1.16)$$

$$h(m) = \frac{2}{\pi} \frac{q}{m} \ln \left(\frac{m + 2q}{2m_\pi} \right). \quad (1.17)$$

₁₁₆₇ For the decay chain $K_1(1270) \rightarrow \rho(770)K$, we include $\rho - \omega$ mixing [60]:

$$T(s) = T_{GS}(s) \cdot \left(1 + \delta \frac{s}{m_\omega^2} T_\omega(s) \right) \quad (1.18)$$

₁₁₆₈ where T_ω is the relativistic Breit-Wigner propagator (Eq. 2.16) of the ω and the relative
₁₁₆₉ magnitude and phase between ρ and ω fixed to the values determined in Ref. [61, 62]:
₁₁₇₀ $|\delta| = 0.159 \pm 0.012 \pm 0.011$ and $\arg(\delta) = 1.36 \pm 0.07 \pm 0.06$.

₁₁₇₁ Running width distributions for 3-body resonances

₁₁₇₂ For the resonances $K_1(1270)$ and $K(1460)$, the energy-dependent widths are reproduced
₁₁₇₃ from Ref. [23]. We further use the energy-dependent widths for the $K_1(1400)$, $K^*(1410)$
₁₁₇₄ and $K^*(1680)$ mesons from Ref. [12]. For all other resonances decaying into a three-
₁₁₇₅ body final state, an energy-dependent width distribution is derived from Equation 2.17
₁₁₇₆ assuming an uniform phase space population. The running width distributions of the
₁₁₇₇ 3-body resonances included in the baseline model are shown in Fig. A.1.

₁₁₇₈ Additional models

₁₁₇₉ Lineshape models for resonances which are not part of the nominal model, can be found
₁₁₈₀ in the References. The energy-dependent width of the $f_0(980)$ resonance is given by the
₁₁₈₁ sum of the partial widths into the $\pi\pi$ and KK channels (*i.e.* the Flatté lineshape [63]),
₁₁₈₂ where the coupling constants as well as the mass and width are taken from a measurement
₁₁₈₃ performed by the BES Collaboration [64]. For the $f_2(1270)$ and the $f_0(1370)$ mesons we
₁₁₈₄ use the total decay widths calculated in Ref. [12] which take the channels $\pi\pi$, KK , $\eta\eta$ and
₁₁₈₅ $\pi\pi\pi\pi$ into account.

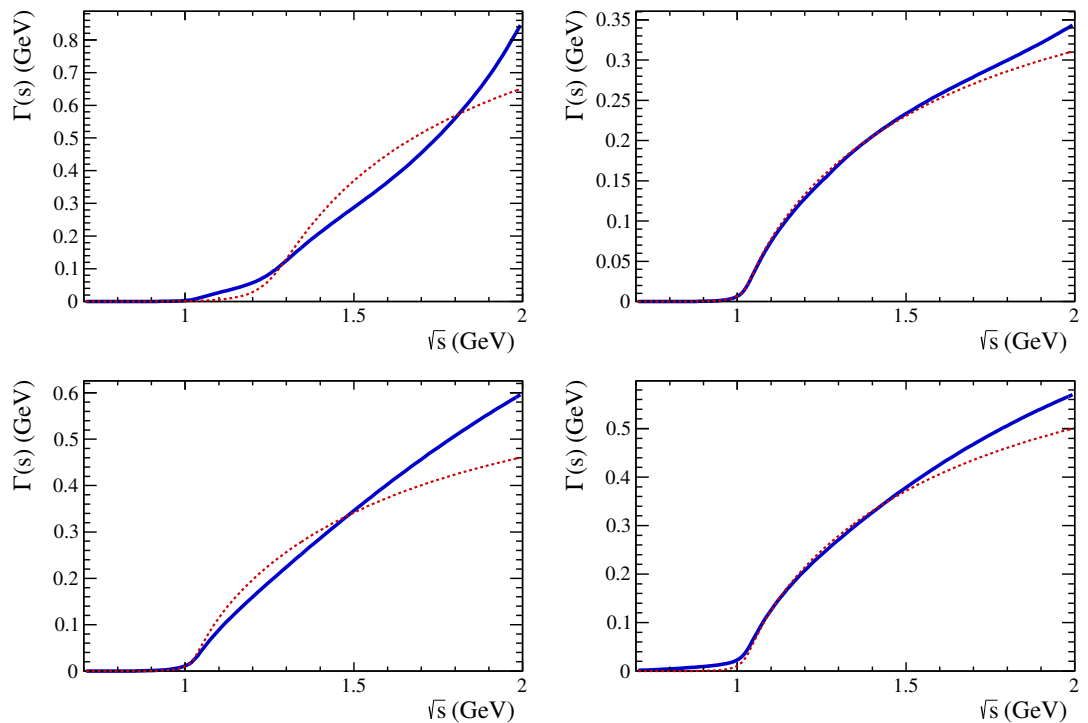


Figure A.1: Running width distributions of the 3-body resonances included in the baseline model: $K_1(1270)$ (top-left), $K_1(1400)$ (top-right), $K(1460)$ (bottom-left) and $K^*(1410)$ (bottom-right). The nominal models are shown in blue, alternative models used for systematic studies in red.

1186 B Stripping and Trigger cuts

1187 The following text describes variables which are used in Table B.1 and might be ambiguous,
 1188 or which benefits are not straight forward. Where noted, different cut values are applied
 1189 for Run-I and Run-II data. In Table B.1, DOCA is the abbreviation for distance of closest
 1190 approach. This variable is used to ensure that all D_s and $X_{s,d}$ daughters originate from
 1191 the same vertex. DIRA is the abbreviation for the cosine of the angle θ between the
 hadron's flight direction \vec{x} and it's corresponding momentum vector \vec{p} , $\cos \theta_{\vec{x}-\vec{p}}$.

Table B.1: Summary of the stripping selections for $B_s^0 \rightarrow D_s K \pi \pi$ decays. The requirements for Run-II are only given if they have been changed.

Variable	Stripping Cut (Run-I)	Stripping Cut (Run-II)
Track χ^2/nDoF	< 3	
Track p	$> 1000 \text{ MeV}/c$	
Track p_T	$> 100 \text{ MeV}/c$	
Track IP χ^2	> 4	
Track ghost-prob.	< 0.4	
D_s mass	$m_{D_s} \pm 100 \text{ MeV}$	$m_{D_s} \pm 80 \text{ MeV}$
D_s Daughter p_T	$\sum_{i=1}^3 p_{t,i} > 1800 \text{ MeV}/c$	
D_s Daughter DOCA	$< 0.5 \text{ mm}$	
D_s Vertex χ^2/nDoF	< 10	
D_s χ^2 -separation from PV	> 36	
D_s daughter PID(π)	< 20	
D_s daughter PID(K)	> -10	
$X_{s,d}$ mass	$< 4000 \text{ MeV}$	$< 3500 \text{ MeV}$
$X_{s,d}$ Daughter p	$> 2 \text{ GeV}/c$	
$X_{s,d}$ Daughter DOCA	$< 0.4 \text{ mm}$	
$X_{s,d}$ Daughter p_T	$\sum_{i=1}^3 p_{t,i} > 1250 \text{ MeV}/c$	
$X_{s,d}$ Vertex χ^2/nDoF	< 8	
$X_{s,d}$ χ^2 -separation from PV	> 16	
$X_{s,d}$ DIRA	> 0.98	
$X_{s,d}$ $\Delta\rho$	$> 0.1 \text{ mm}$	
$X_{s,d}$ Δz	$> 2.0 \text{ mm}$	
$X_{s,d}$ daughter PID(π)	< 10	
X_s daughter PID(K)	> -2	> 4
B_s^0 mass	$[4750, 7000] \text{ MeV}/c^2$	$[5000, 6000] \text{ MeV}/c^2$
B_s^0 DIRA	> 0.98	> 0.99994
B_s^0 min IP χ^2	< 25	< 20
B_s^0 Vertex χ^2/nDoF	< 10	< 8
$B_s^0 \tau_{B_s^0}$	$> 0.2 \text{ ps}$	

1192

1193 Table B.2 summarizes the trigger requirements imposed by the Hlt1 line used in this
1194 analysis for Run-I. At least one of the six decay particles must pass the listed requirements
1195 in order for the event to be stored for further analysis. For Run-II, this trigger line was
1196 updated and uses a multivariate classifier which takes the variables listed in Table B.2 as
1197 input, rather than directly cutting on them.

1198 The Hlt2 2, 3 and 4-body topological lines use a Boosted Decision Tree based on the
1199 b-hadron p_T , its flight distance χ^2 from the nearest PV and the sum of the B_s^0 and D_s
1200 vertex χ^2 divided by the sum of their number of degrees of freedom. Table B.3 summarizes
1201 the cuts applied by the inclusive ϕ trigger, which requires that a $\phi \rightarrow KK$ candidate can
be formed out of two tracks present in the event.

Table B.2: Summary of the cuts applied by the Hlt1TrackAllL0 trigger for Run-I. At least one of the six decay particles must pass this requirements, in order for the event to be accepted.

Quantity	Hlt1TrackAllL0 requirement
Track IP [mm]	> 0.1
Track IP χ^2	> 16
Track χ^2/nDoF	< 2.5
Track p_T	$> 1.7 \text{ GeV}/c$
Track p	$> 10 \text{ GeV}/c$
Number VELO hits/track	> 9
Number missed VELO hits/track	< 3
Number OT+IT $\times 2$ hits/track	> 16

Table B.3: Summary of the cuts applied by the Hlt2 inclusive ϕ trigger. A $\phi \rightarrow KK$ candidate, formed by two tracks in the event, must pass this requirements in order for the event to be accepted.

Quantity	Hlt2IncPhi requirement
ϕ mass	$m_\phi \pm 12 \text{ MeV}/c^2$ of PDG value
ϕp_T	$> 2.5 \text{ GeV}/c$
ϕ vertex χ^2/nDoF	< 20
ϕ IP χ^2 to any PV	> 5

1202

C Details of multivariate classifier

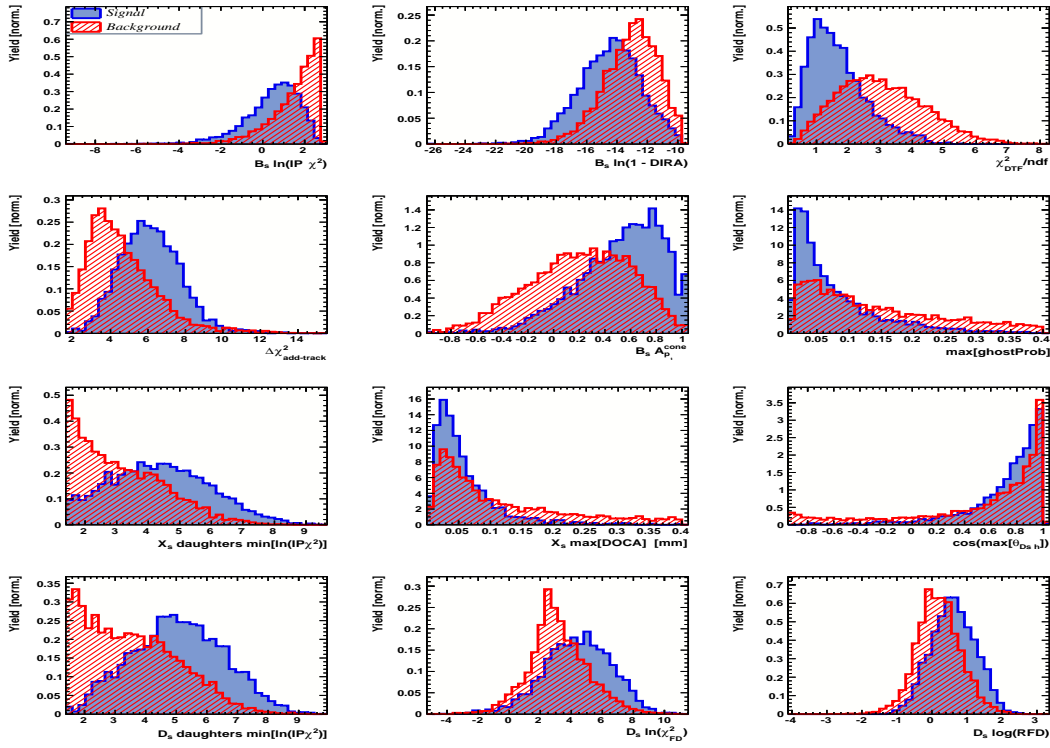


Figure C.1: Variables used to train the BDTG for category [Run-I,L0-TOS].

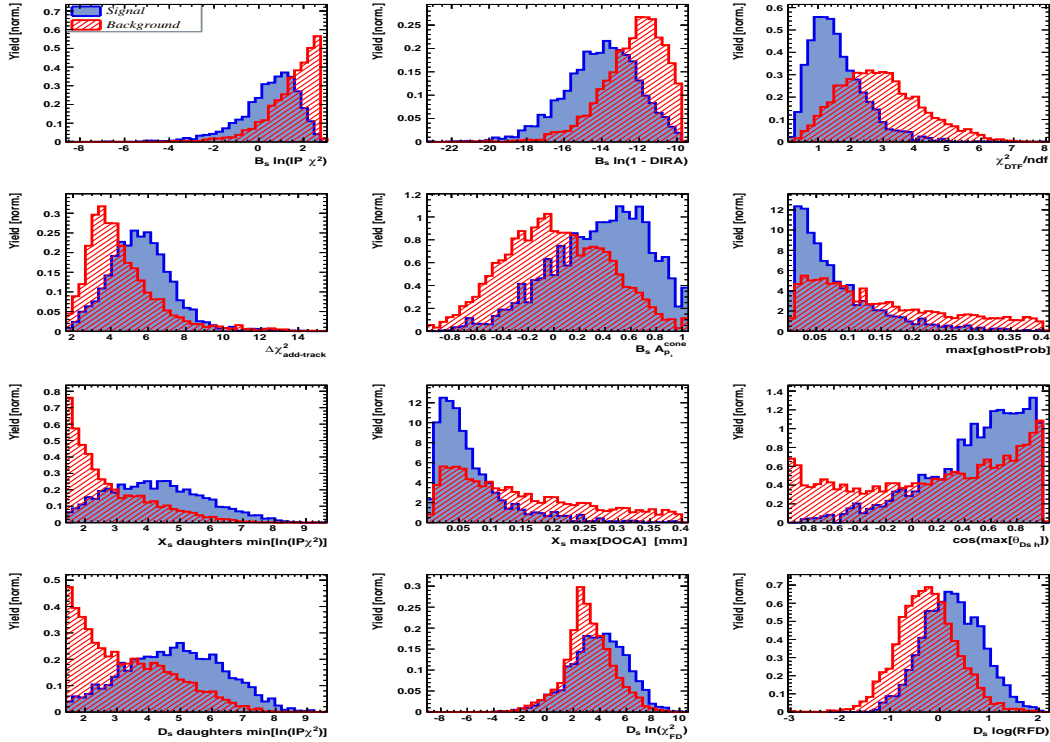


Figure C.2: Variables used to train the BDTG for category [Run-I,L0-TIS].

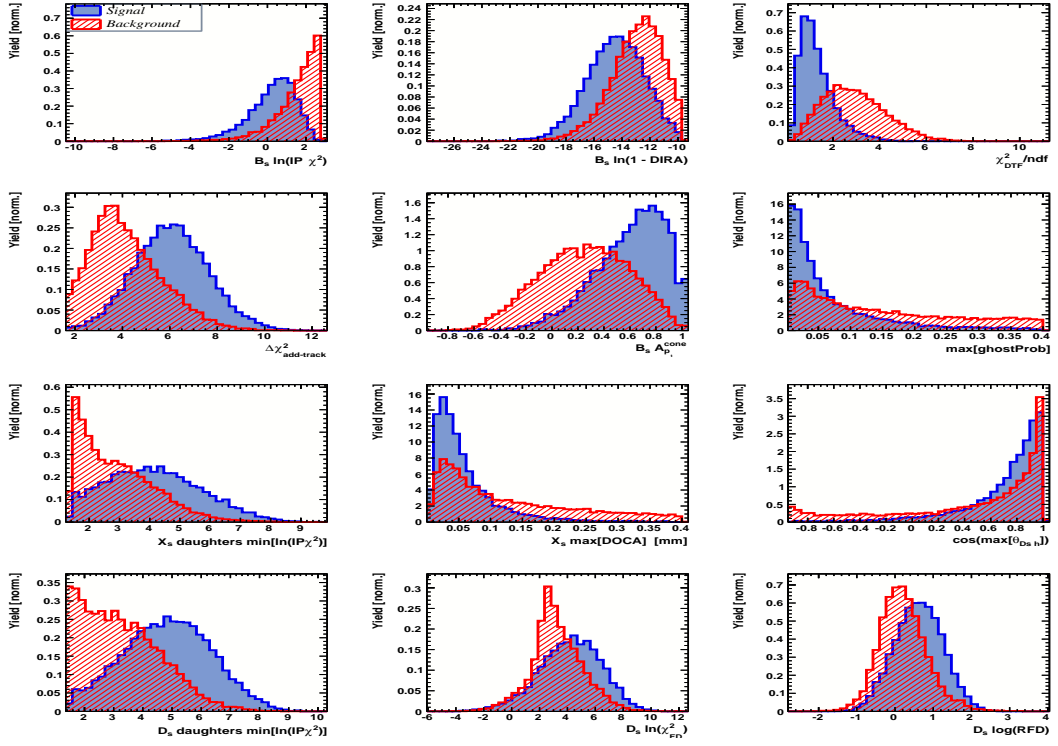


Figure C.3: Variables used to train the BDTG for category [Run-II,L0-TOS].

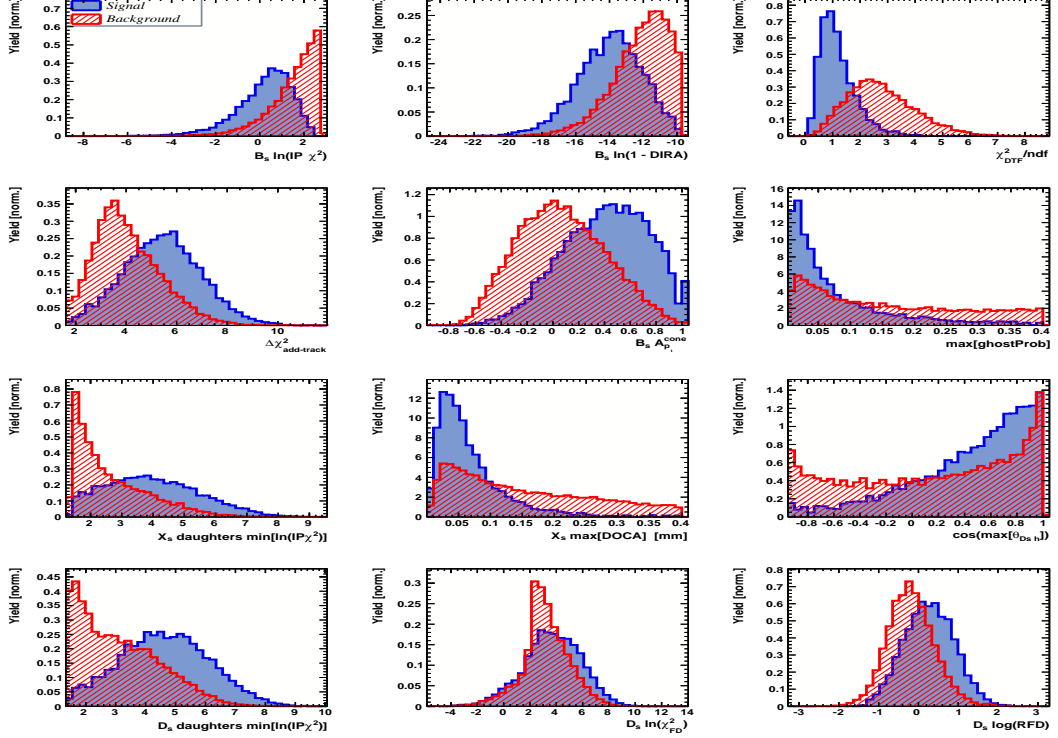


Figure C.4: Variables used to train the BDTG for category [Run-II,L0-TIS].

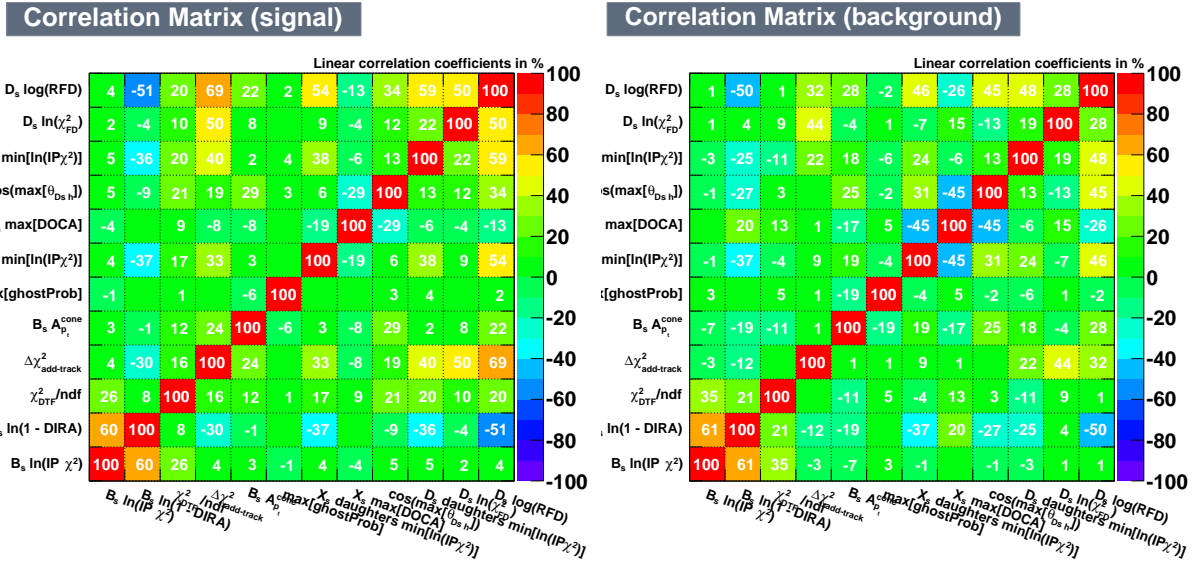


Figure C.5: Correlation matrix for the (left) signal and (right) background input distributions.

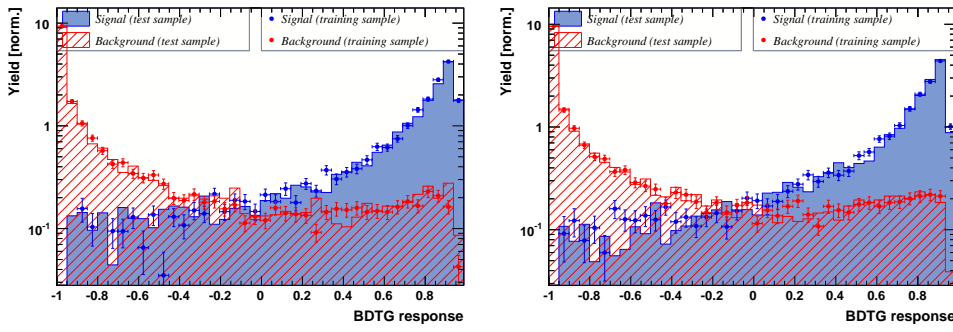


Figure C.6: Response of the classifier trained on the even and tested on the odd sample (left) and trained on the odd and tested on the even sample (right) for category [Run-I,L0-TOS].

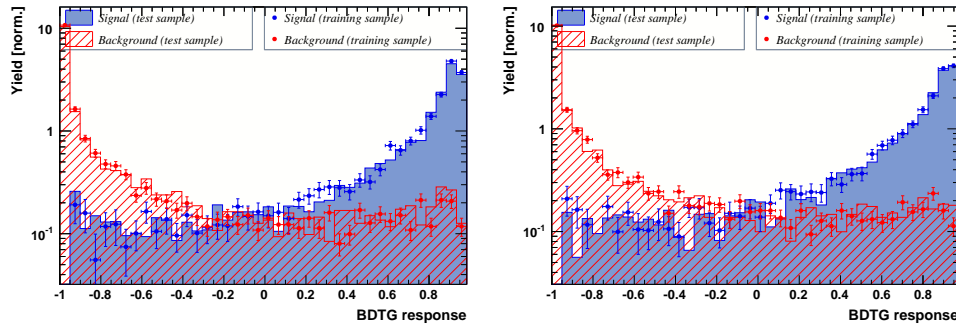


Figure C.7: Response of the classifier trained on the even and tested on the odd sample (left) and trained on the odd and tested on the even sample (right) for category [Run-I,L0-TIS].

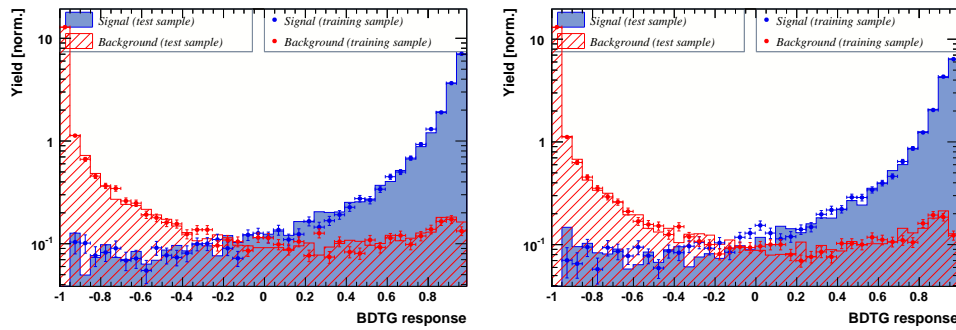


Figure C.8: Response of the classifier trained on the even and tested on the odd sample (left) and trained on the odd and tested on the even sample (right) for category [Run-II,L0-TOS].

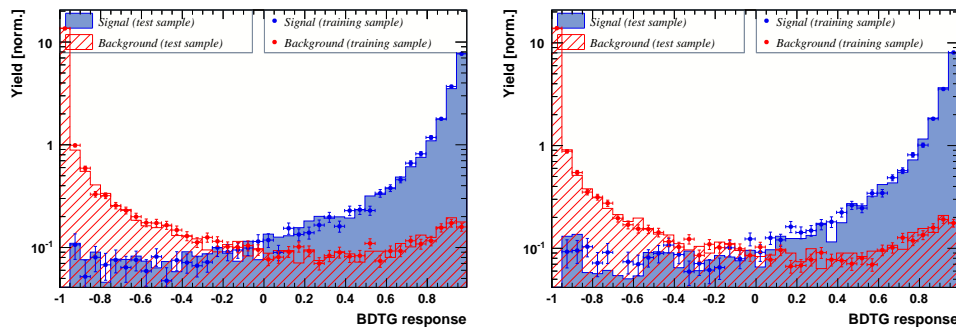


Figure C.9: Response of the classifier trained on the even and tested on the odd sample (left) and trained on the odd and tested on the even sample (right) for category [Run-II,L0-TIS].

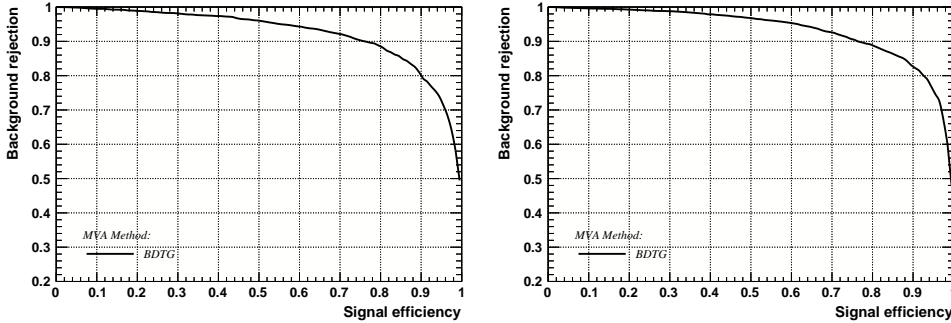


Figure C.10: Signal efficiency versus background rejection for the BDT trained on the even (left) and odd (right) sample for category [Run-I,L0-TOS].

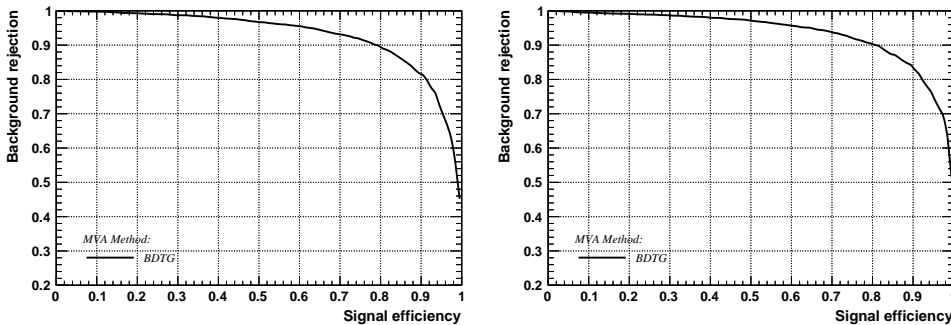


Figure C.11: Signal efficiency versus background rejection for the BDT trained on the even (left) and odd (right) sample for category [Run-I,L0-TIS].

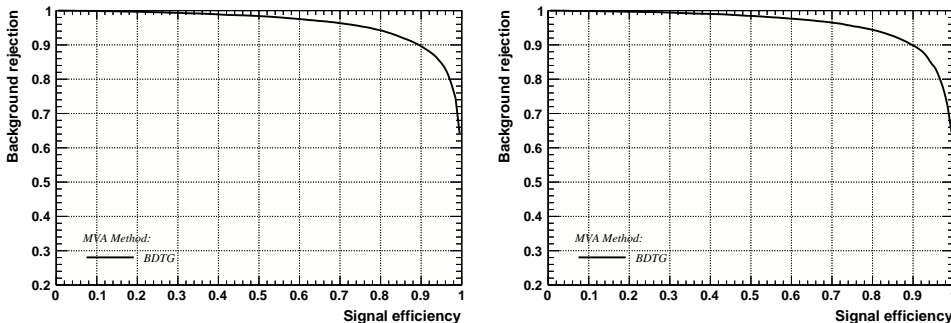


Figure C.12: Signal efficiency versus background rejection for the BDT trained on the even (left) and odd (right) sample for category [Run-II,L0-TOS].

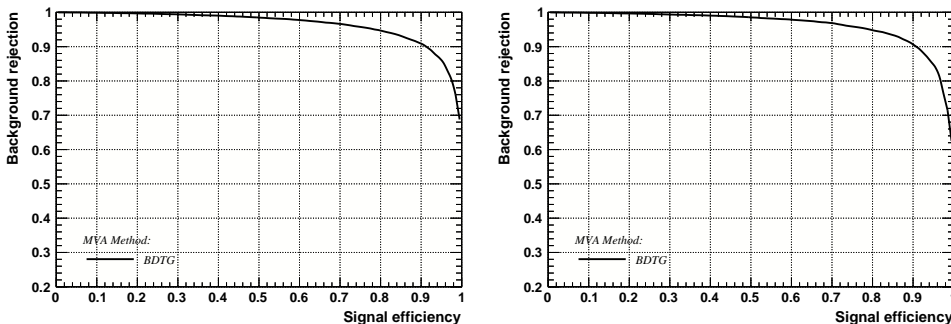


Figure C.13: Signal efficiency versus background rejection for the BDT trained on the even (left) and odd (right) sample for category [Run-II,L0-TIS].

1204 D Detailed mass fits

1205 In this section, all fits to the mass distribution of $B_s^0 \rightarrow D_s\pi\pi\pi$ and $B_s^0 \rightarrow D_sK\pi\pi$
 1206 candidates are shown. The fits are performed simultaneously in run period (Run-I, Run-
 1207 II), D_s final state ($D_s \rightarrow KK\pi$ non-resonant, $D_s \rightarrow \phi\pi$, $D_s \rightarrow K^*K$, or $D_s \rightarrow \pi\pi\pi$) and
 1208 L0 trigger category.

Table D.1: Signal and background yields for the $B_s \rightarrow D_s\pi\pi\pi$ sample split by data-taking period.

Component	Yield for Run I
$B_s \rightarrow D_s\pi\pi\pi$	21443 ± 122
$B^0 \rightarrow D_s\pi\pi\pi$	358 ± 53
Partially reconstructed bkg.	8657 ± 104
Combinatorial bkg.	9492 ± 120
Component	Yield for Run II
$B_s \rightarrow D_s\pi\pi\pi$	82711 ± 257
$B^0 \rightarrow D_s\pi\pi\pi$	1359 ± 1326
Partially reconstructed bkg.	34471 ± 937
Combinatorial bkg.	31574 ± 680

Table D.2: Signal and background yields for the $B_s \rightarrow D_sK\pi\pi$ sample split by data-taking period.

Component	Yield for Run I
$B_s \rightarrow D_sK\pi\pi$	1018 ± 56
$B^0 \rightarrow D_sK\pi\pi$	846 ± 43
Partially reconstructed bkg.	232 ± 137
Misidentified bkg.	426 ± 0
Combinatorial bkg.	2520 ± 324
Component	Yield for Run II
$B_s \rightarrow D_sK\pi\pi$	4153 ± 76
$B^0 \rightarrow D_sK\pi\pi$	3264 ± 86
Partially reconstructed bkg.	1592 ± 312
Misidentified bkg.	760 ± 0
Combinatorial bkg.	6653 ± 186

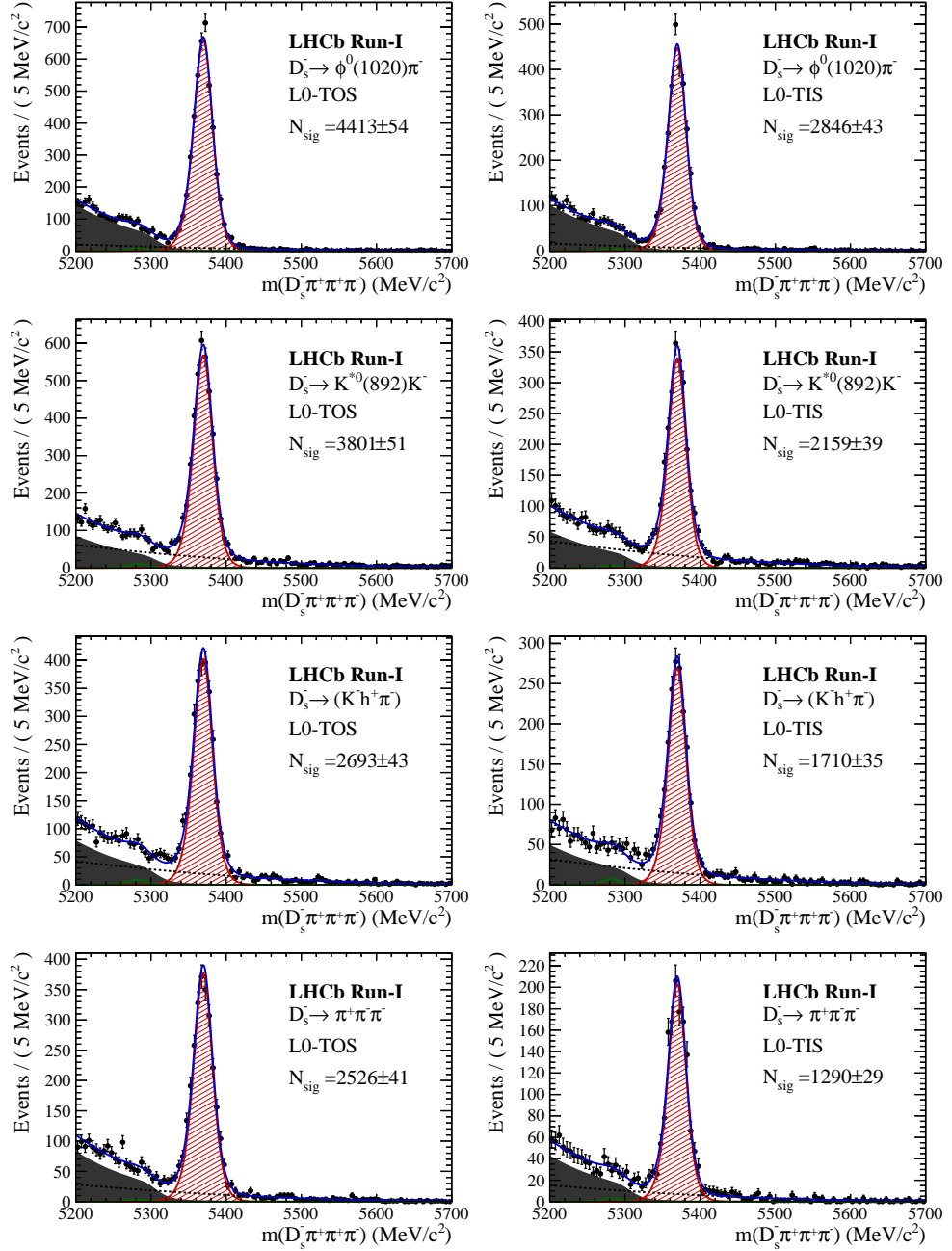


Figure D.1: Invariant mass distributions of $B_s^0 \rightarrow D_s \pi \pi \pi$ candidates for Run-I data.

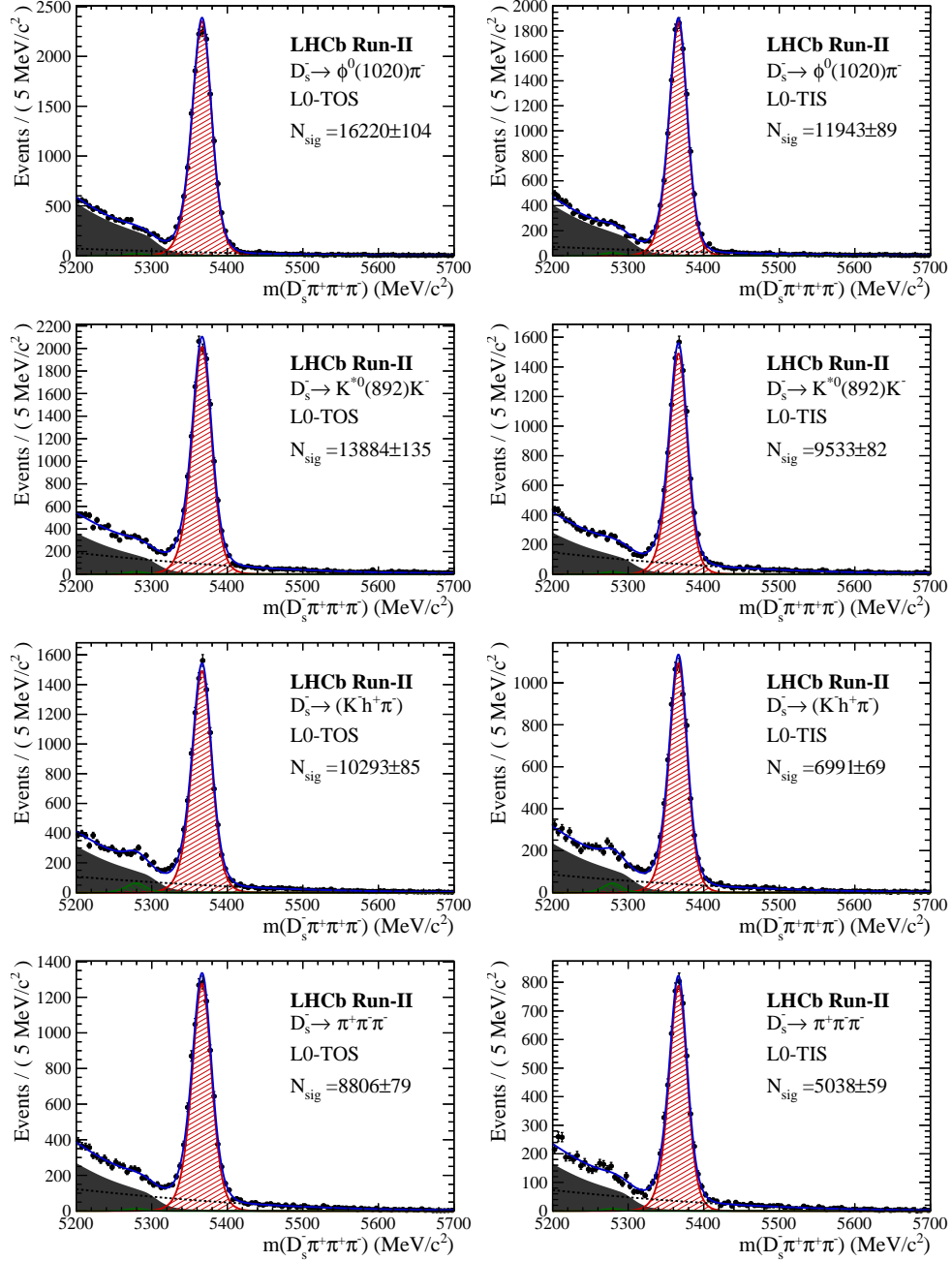


Figure D.2: Invariant mass distributions of $B_s^0 \rightarrow D_s \pi^+ \pi^- \pi^+ \pi^-$ candidates for Run-II data.

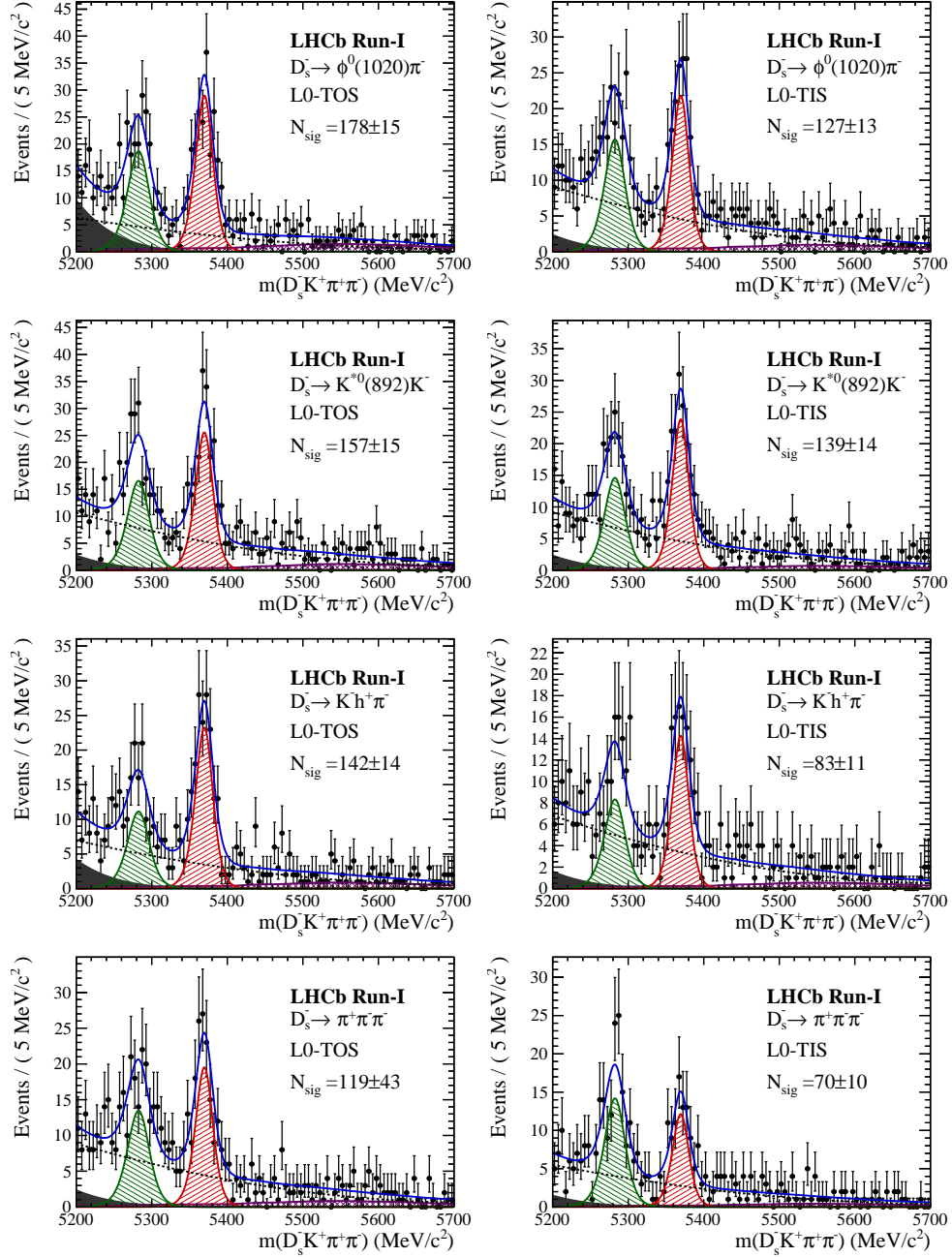


Figure D.3: Invariant mass distributions of $B_s^0 \rightarrow D_s K \pi \pi$ candidates for Run-I data.

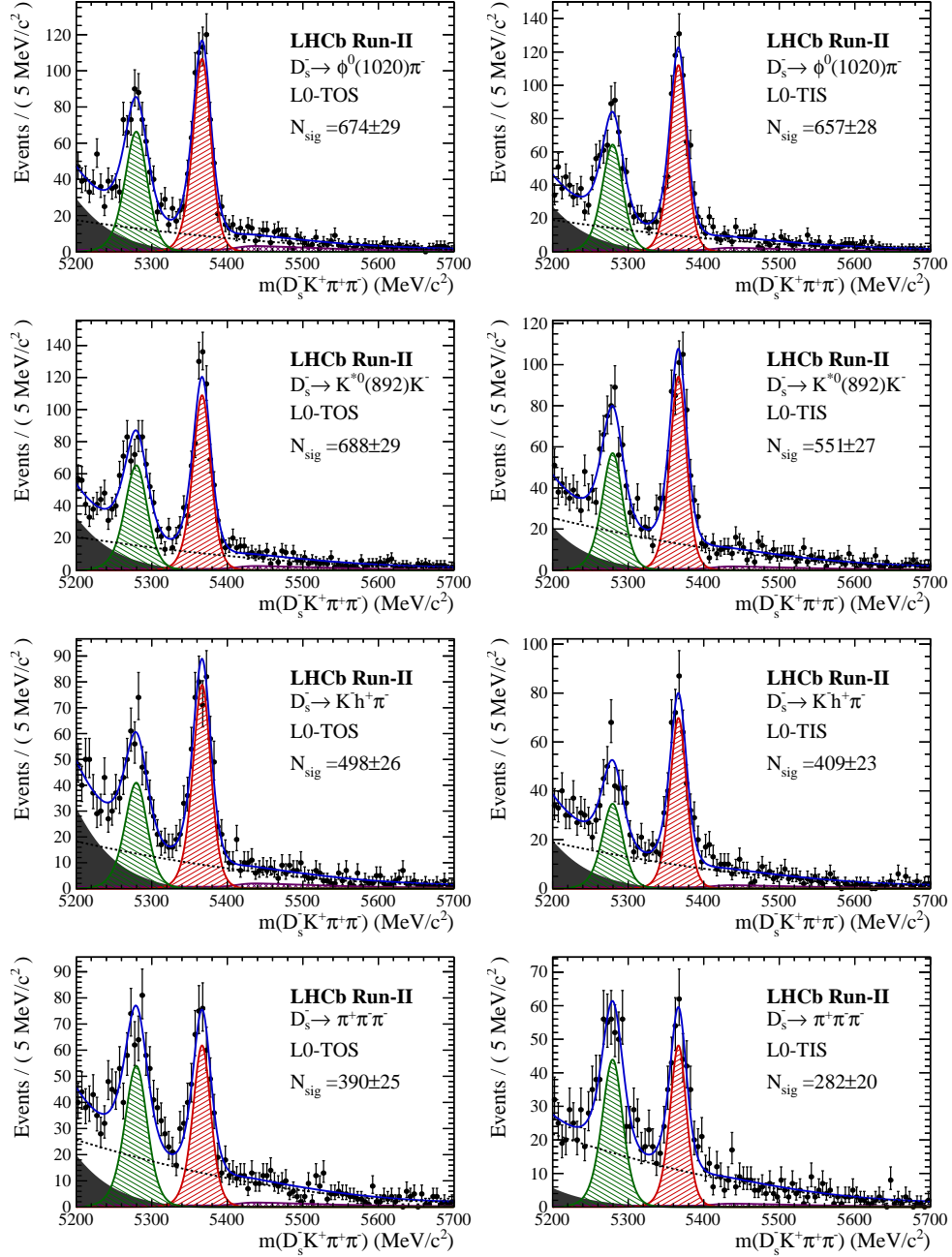


Figure D.4: Invariant mass distributions of $B_s^0 \rightarrow D_s K \pi \pi$ candidates for Run-II data.

1209 E Decay-time Resolution fits

1210 This section contains all fits to the distributions of the decay time difference Δt between
 1211 the true and the reconstructed decay time of the truth-matched B_s^0 candidates on MC.
 1212 The fits are performed in bins of the decay time error σ_t , where an adaptive binning
 1213 scheme is used to ensure that approximately the same number of events are found in each
 1214 bin.

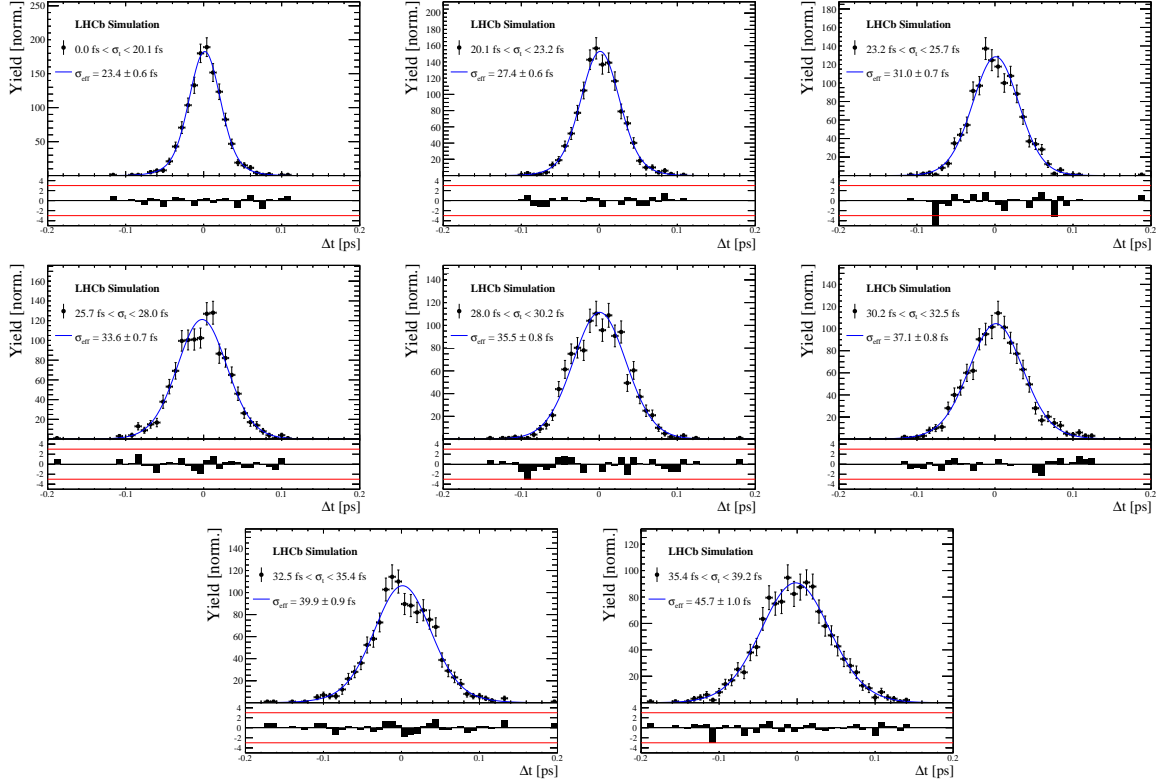


Figure E.1: Difference of the true and measured decay time of $B_s^0 \rightarrow D_s K\pi\pi$ MC candidates in bins of the per-event decay time error estimate..

Table E.1: Measured time resolution for $B_s \rightarrow D_s K\pi\pi$ MC in bins of the per-event decay time error estimate.

σ_t Bin [fs]	σ_1 [fs]	σ_2 [fs]	f_1	D	σ_{eff} [fs]
0.0 - 20.1	19 ± 0.675	33.8 ± 1.77	0.75 ± 0	0.917 ± 0.00406	23.4 ± 0.599
20.1 - 23.2	23.4 ± 0.86	37.4 ± 1.95	0.75 ± 0	0.888 ± 0.00477	27.4 ± 0.621
23.2 - 25.7	28.1 ± 1.02	38.7 ± 2.32	0.75 ± 0	0.86 ± 0.00563	31 ± 0.671
25.7 - 28.0	30.1 ± 1.12	43.2 ± 2.56	0.75 ± 0	0.837 ± 0.00651	33.6 ± 0.734
28.0 - 30.2	32.4 ± 1.12	44.2 ± 2.59	0.75 ± 0	0.819 ± 0.00694	35.5 ± 0.756
30.2 - 32.5	32.6 ± 1.38	49.2 ± 3.04	0.75 ± 0	0.805 ± 0.00792	37.1 ± 0.841
32.5 - 35.4	34.4 ± 1.19	54.7 ± 2.85	0.75 ± 0	0.778 ± 0.0086	39.9 ± 0.879
35.4 - 39.2	41.9 ± 1.8	56.9 ± 4.18	0.75 ± 0	0.719 ± 0.00997	45.7 ± 0.962
39.2 - 44.7	42.2 ± 1.56	68.1 ± 4.01	0.75 ± 0	0.687 ± 0.0114	48.8 ± 1.08
44.7 - 120.0	55.5 ± 2.59	83 ± 14.7	0.75 ± 0	0.546 ± 0.0521	62 ± 4.89

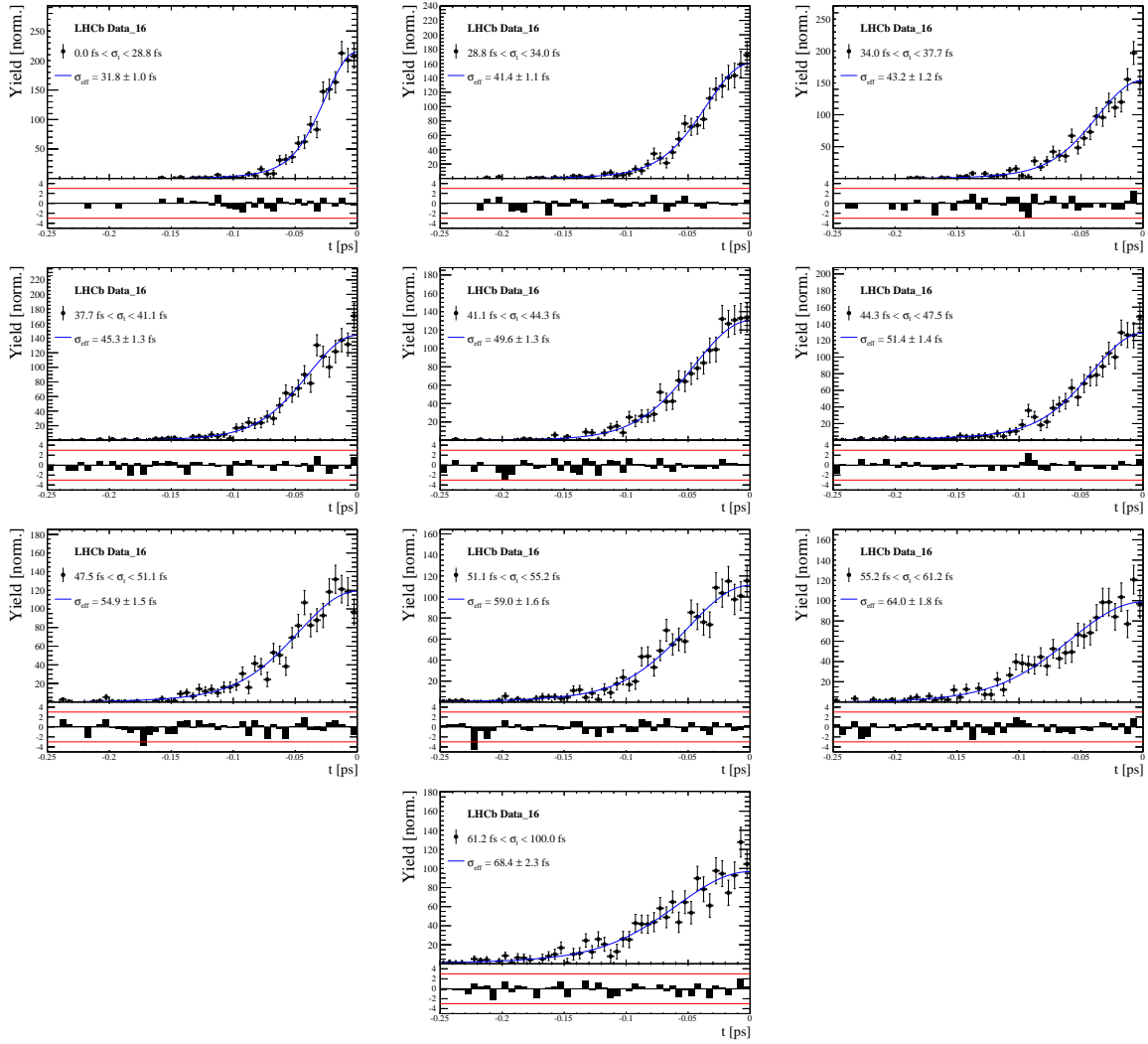


Figure E.2: Decay-time distribution for fake B_s candidates from promptly produced D_s candidates, combined with random prompt $K\pi\pi$ bachelor tracks, for bins in the per-event decay time error estimate. Data taken in 2016.

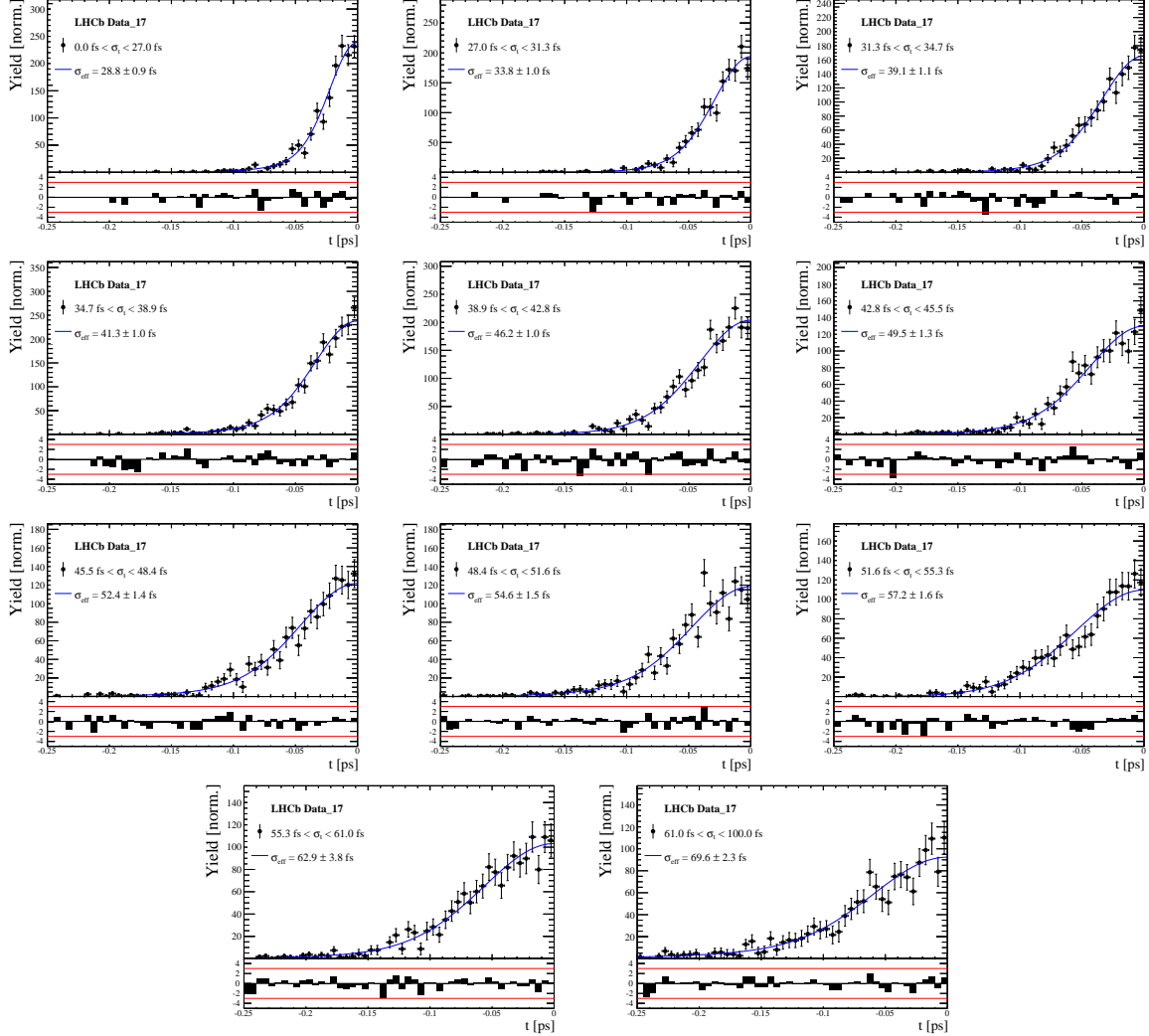


Figure E.3: Decay-time distribution for fake B_s candidates from promptly produced D_s candidates, combined with random prompt $K\pi\pi$ bachelor tracks, for bins in the per-event decay time error estimate. Data taken in 2017.

Table E.2: Measured time resolution for prompt- D_s data in bins of the per-event decay time error estimate. Data taken in 2016.

σ_t Bin [fs]	σ_1 [fs]	σ_2 [fs]	f_1	D	σ_{eff} [fs]
0.0 - 28.8	25.3 ± 1.05	47.8 ± 2.82	0.75 ± 0	0.853 ± 0.00827	31.8 ± 0.967
28.8 - 34.0	34.4 ± 1.38	60.4 ± 3.66	0.75 ± 0	0.763 ± 0.0114	41.4 ± 1.14
34.0 - 37.7	35.9 ± 1.7	63.1 ± 4.05	0.75 ± 0	0.745 ± 0.0122	43.2 ± 1.2
37.7 - 41.1	38.3 ± 1.63	65.3 ± 4.28	0.75 ± 0	0.723 ± 0.013	45.3 ± 1.26
41.1 - 44.3	43.6 ± 2.04	67.2 ± 4.78	0.75 ± 0	0.679 ± 0.0137	49.6 ± 1.3
44.3 - 47.5	40.4 ± 1.64	85.4 ± 5.28	0.75 ± 0	0.659 ± 0.0151	51.4 ± 1.41
47.5 - 51.1	46.1 ± 2.02	82.5 ± 5.61	0.75 ± 0	0.622 ± 0.0161	54.9 ± 1.5
51.1 - 55.2	49.2 ± 2.1	92.3 ± 6.57	0.75 ± 0	0.577 ± 0.0174	59 ± 1.62
55.2 - 61.2	56.6 ± 2.53	88.8 ± 7.84	0.75 ± 0	0.525 ± 0.0192	64 ± 1.82
61.2 - 100.0	57.6 ± 3.09	112 ± 14.5	0.75 ± 0	0.478 ± 0.0232	68.4 ± 2.25

Table E.3: Measured time resolution for prompt- D_s data in bins of the per-event decay time error estimate. Data taken in 2017.

σ_t Bin [fs]	σ_1 [fs]	σ_2 [fs]	f_1	D	σ_{eff} [fs]
0.0 - 27.0	22.1 ± 0.942	44.7 ± 2.65	0.75 ± 0	0.877 ± 0.00729	28.8 ± 0.914
27.0 - 31.3	28.3 ± 1.12	48.2 ± 2.98	0.75 ± 0	0.835 ± 0.00854	33.8 ± 0.959
31.3 - 34.7	32.8 ± 1.29	55.8 ± 3.39	0.75 ± 0	0.786 ± 0.0105	39.1 ± 1.08
34.7 - 38.9	33.4 ± 1.2	62.5 ± 3.04	0.75 ± 0	0.764 ± 0.00951	41.3 ± 0.956
38.9 - 42.8	40.3 ± 1.39	63 ± 3.58	0.75 ± 0	0.715 ± 0.0104	46.2 ± 1
42.8 - 45.5	42.2 ± 1.63	70.7 ± 4.35	0.75 ± 0	0.68 ± 0.0138	49.5 ± 1.3
45.5 - 48.4	44.7 ± 1.85	75.7 ± 4.91	0.75 ± 0	0.649 ± 0.0152	52.4 ± 1.42
48.4 - 51.6	46.3 ± 2.05	80.3 ± 5.66	0.75 ± 0	0.626 ± 0.0161	54.6 ± 1.5
51.6 - 55.3	53.2 ± 1.2	69.1 ± 3.03	0.75 ± 0	0.597 ± 0.0167	57.2 ± 1.55
55.3 - 61.0	54.8 ± 2.29	90.9 ± 12.2	0.75 ± 0	0.535 ± 0.0406	62.9 ± 3.82
61.0 - 100.0	58.4 ± 3.18	118 ± 15.6	0.75 ± 0	0.466 ± 0.0233	69.6 ± 2.28

1215 F Comparison of time-acceptance in subsamples

1216 Figure F.1 shows the spline coefficients obtained by fitting the decay-time distribution of
 1217 $B_s^0 \rightarrow D_s\pi\pi\pi$ data candidates in different subsamples. Sufficient agreement is observed
 1218 within a given data-taking period, while the acceptance shapes for Run-I and Run-II
 1219 data differ significantly. The fitted splines for the different D_s final states are in a good
 1220 agreement. The largest deviations are observed between the different L0 categories.

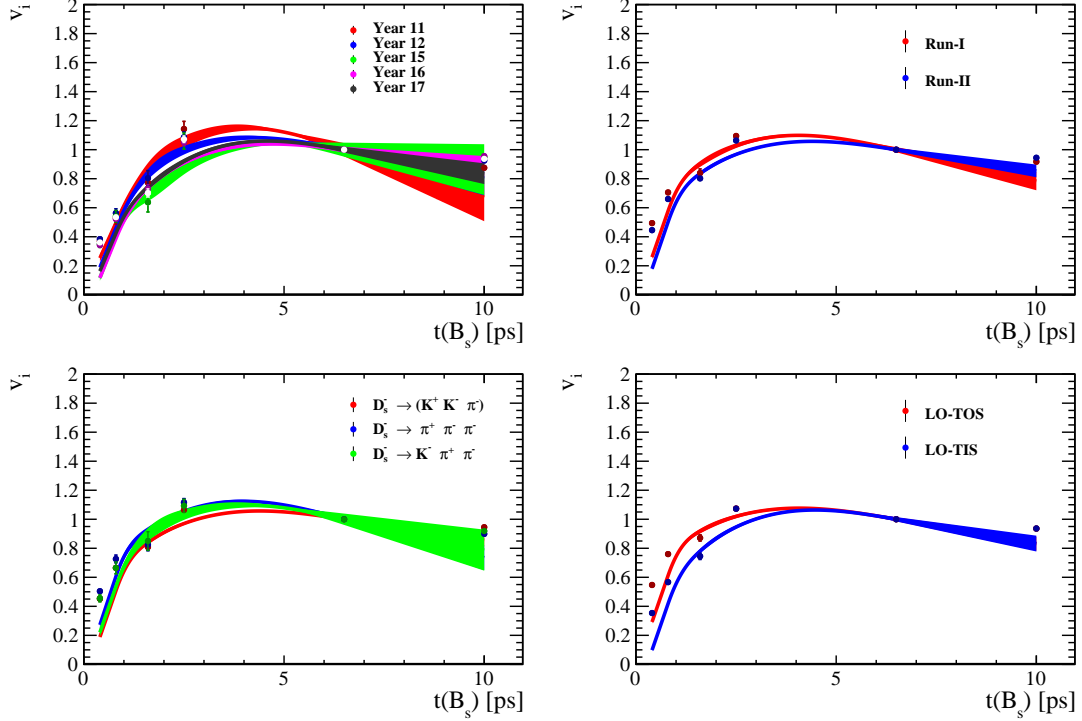


Figure F.1: Comparison of the spline coefficients (point with error bars) obtained from time-dependent fits to the $B_s^0 \rightarrow D_s\pi\pi\pi$ decay-time for different subsamples: (top-left) different years of data-taking; (top-right) different data-taking periods; (bottom-left) different D_s final states; (bottom-right) different trigger categories. The interpolated splines are overlaid.

1221 G Comparison of phase-space acceptance in subsam- 1222 ples

1223 Figures G.1, G.2 and G.3 compare the phase space-acceptance projections obtained from
 1224 $B_s \rightarrow D_s K\pi\pi$ MC in different subsamples. Sufficient agreement is observed between
 1225 different data-taking periods and D_s final states. The largest deviations are observed
 1226 between the different L0 categories.

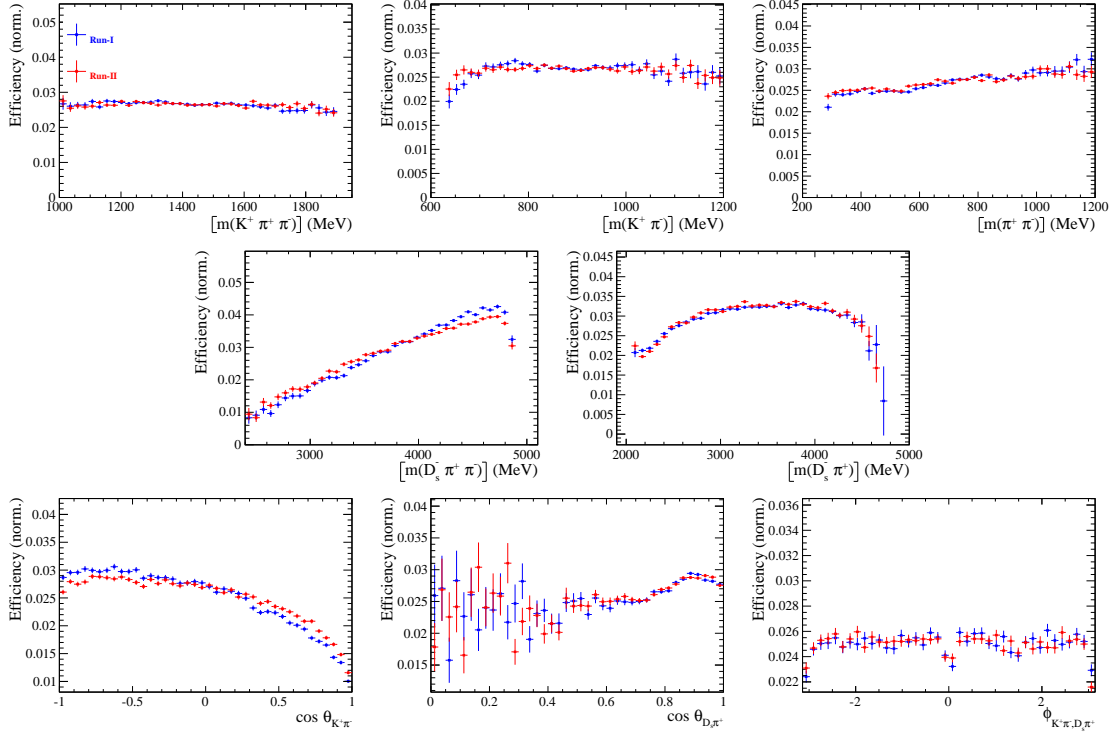


Figure G.1: Comparison of the phase space acceptance for different data-taking periods. A χ^2 -test between the samples yields $\chi^2/\nu = 1.10$ (with $\nu = 533$) using an adaptive 5D binning.

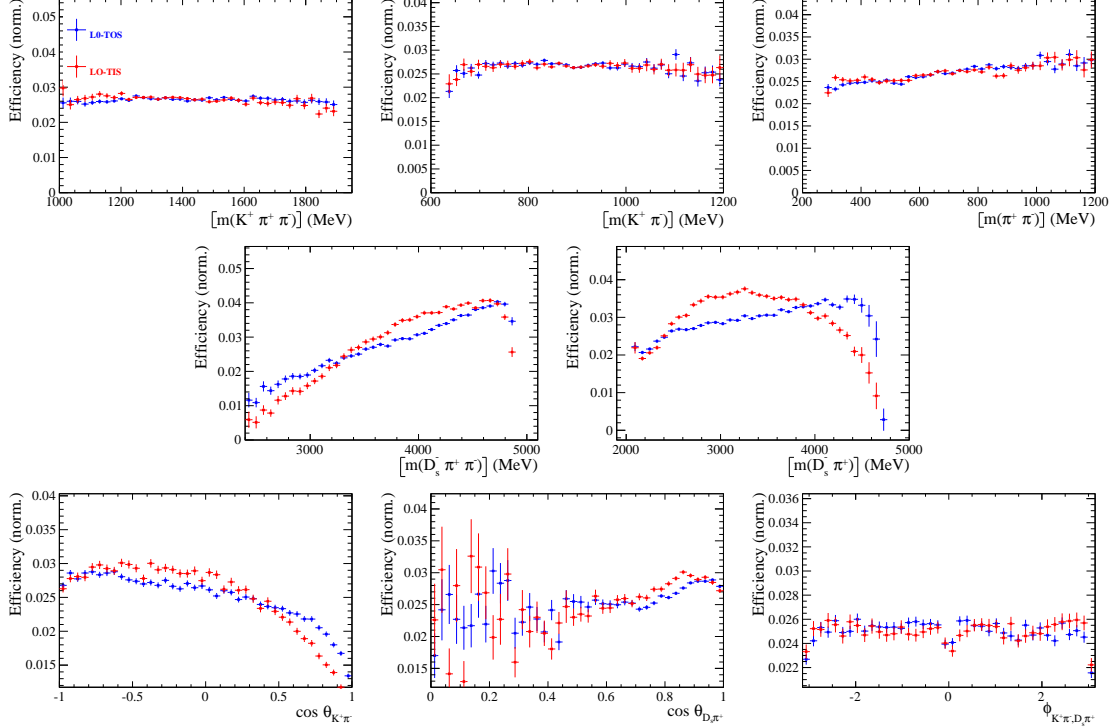


Figure G.2: Comparison of the phase space acceptance for different trigger categories. A χ^2 -test between the samples yields $\chi^2/\nu = 1.62$ (with $\nu = 1211$) using an adaptive 5D binning.

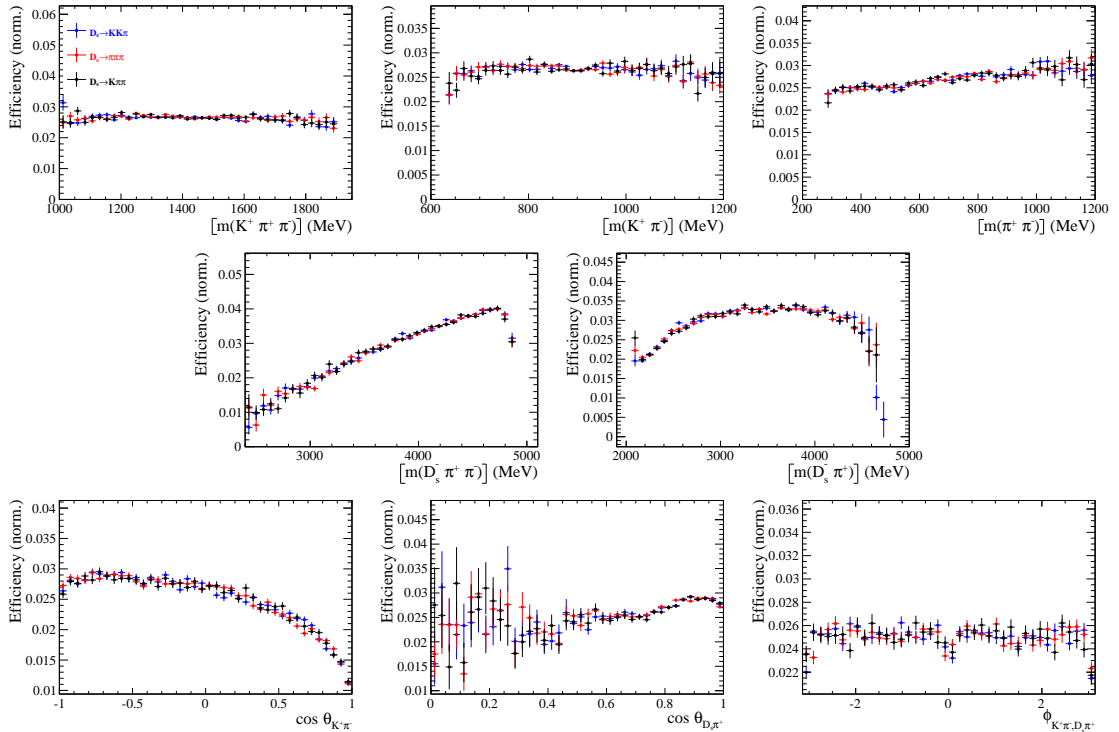


Figure G.3: Comparison of the phase space acceptance for different D_s final states. A χ^2 -test using an adaptive 5D binning between the $D_s \rightarrow KK\pi$ and $D_s \rightarrow K\pi\pi$ samples yields $\chi^2/\nu = 1.01$ (with $\nu = 728$), $\chi^2/\nu = 0.96$ (with $\nu = 988$) between $D_s \rightarrow KK\pi$ and $D_s \rightarrow \pi\pi\pi$ and $\chi^2/\nu = 1.00$ (with $\nu = 728$) between $D_s \rightarrow \pi\pi\pi$ and $D_s \rightarrow K\pi\pi$.

₁₂₂₇ **H OS tagger calibration parameters**

tagger	$\langle \eta \rangle$	$p_0 - \langle \eta \rangle$	p_1	$\rho(p_0, p_1)$
OS μ	0.30	0.010 ± 0.023	1.02 ± 0.26	0.03
OS e	0.29	0.042 ± 0.036	1.87 ± 0.59	0.08
OS K	0.42	0.020 ± 0.010	1.22 ± 0.15	0.03
OS Vtx charge	0.38	-0.011 ± 0.015	1.05 ± 0.23	-0.01

Table H.1: Calibration parameters of the OS taggers for Run-I.

tagger	$\langle \eta \rangle$	$p_0 - \langle \eta \rangle$	p_1	$\rho(p_0, p_1)$
OS μ	0.33	-0.001 ± 0.014	1.24 ± 0.21	0.06
OS e	0.36	0.014 ± 0.020	1.16 ± 0.27	0.06
OS K	0.40	-0.011 ± 0.010	1.51 ± 0.21	0.03
OS Vtx charge	0.39	-0.011 ± 0.010	1.25 ± 0.15	0.03
OS charm	0.36	-0.030 ± 0.019	0.96 ± 0.37	0.04

Table H.2: Calibration parameters of the OS taggers for Run-II.

₁₂₂₈ **I Spin Amplitudes**

₁₂₂₉ The spin factors used for $B \rightarrow P_1 P_2 P_3 P_4$ decays are given in Table I.1.

Table I.1: Spin factors for all topologies considered in this analysis. In the decay chains, S , P , V , A , T and PT stand for scalar, pseudoscalar, vector, axial vector, tensor and pseudotensor, respectively. If no angular momentum is specified, the lowest angular momentum state compatible with angular momentum conservation and, where appropriate, parity conservation, is used.

Number	Decay chain	Spin amplitude
1	$B \rightarrow (P P_1)$, $P \rightarrow (S P_2)$, $S \rightarrow (P_3 P_4)$	1
2	$B \rightarrow (P P_1)$, $P \rightarrow (V P_2)$, $V \rightarrow (P_3 P_4)$	$L_{(1)\alpha}(P) L_{(1)}^\alpha(V)$
3	$B \rightarrow (A P_1)$, $A \rightarrow (V P_2)$, $V \rightarrow (P_3 P_4)$	$L_{(1)\alpha}(B) P_{(1)}^{\alpha\beta}(A) L_{(1)\beta}(V)$
4	$B \rightarrow (A P_1)$, $A[D] \rightarrow (P_2 V)$, $V \rightarrow (P_3 P_4)$	$L_{(1)\alpha}(B) L_{(2)}^{\alpha\beta}(A) L_{(1)\beta}(V)$
5	$B \rightarrow (A P_1)$, $A \rightarrow (S P_2)$, $S \rightarrow (P_3 P_4)$	$L_{(1)\alpha}(B) L_{(1)}^\alpha(A)$
6	$B \rightarrow (A P_1)$, $A \rightarrow (T P_2)$, $T \rightarrow (P_3 P_4)$	$L_{(1)\alpha}(B) L_{(1)\beta}(A) L_{(2)}^{\alpha\beta}(T)$
7	$B \rightarrow (V_1 P_1)$, $V_1 \rightarrow (V_2 P_2)$, $V_2 \rightarrow (P_3 P_4)$	$L_{(1)\mu}(B) P_{(1)}^{\mu\alpha}(V_1) \epsilon_{\alpha\beta\gamma\delta} L_{(1)}^\beta(V_1) p_{V_1}^\gamma L_{(1)}^\delta(V_2)$
8	$B \rightarrow (PT P_1)$, $PT \rightarrow (V P_2)$, $V \rightarrow (P_3 P_4)$	$L_{(2)\alpha\beta}(B) P_{(2)}^{\alpha\beta\gamma\delta}(PT) L_{(1)\gamma}(PT) L_{(1)\delta}(V)$
9	$B \rightarrow (PT P_1)$, $PT \rightarrow (S P_2)$, $S \rightarrow (P_3 P_4)$	$L_{(2)\alpha\beta}(B) L_{(2)}(PT)^{\alpha\beta}$
10	$B \rightarrow (PT P_1)$, $PT \rightarrow (T P_2)$, $T \rightarrow (P_3 P_4)$	$L_{(2)\alpha\beta}(B) P_{(2)}^{\alpha\beta\gamma\delta}(PT) L_{(2)\gamma\delta}(T)$
11	$B \rightarrow (T P_1)$, $T \rightarrow (V P_2)$, $V \rightarrow (P_3 P_4)$	$L_{(2)\mu\nu}(B) P_{(2)}^{\mu\nu\rho\alpha}(T) \epsilon_{\alpha\beta\gamma\delta} L_{(2)\rho}^\beta(T) p_T^\gamma P_{(1)}^{\delta\sigma}(T) L_{(1)\sigma}(V)$
12	$B \rightarrow (T_1 P_1)$, $T_1 \rightarrow (T_2 P_2)$, $T_2 \rightarrow (P_3 P_4)$	$L_{(2)\mu\nu}(B) P_{(2)}^{\mu\nu\rho\alpha}(T_1) \epsilon_{\alpha\beta\gamma\delta} L_{(1)}^\beta(T_1) p_{T_1}^\gamma L_{(2)\rho}^\delta(T_2)$
13	$B \rightarrow (S_1 S_2)$, $S_1 \rightarrow (P_1 P_2)$, $S_2 \rightarrow (P_3 P_4)$	1
14	$B \rightarrow (V S)$, $V \rightarrow (P_1 P_2)$, $S \rightarrow (P_3 P_4)$	$L_{(1)\alpha}(B) L_{(1)}^\alpha(V)$
15	$B \rightarrow (V_1 V_2)$, $V_1 \rightarrow (P_1 P_2)$, $V_2 \rightarrow (P_3 P_4)$	$L_{(1)\alpha}(V_1) L_{(1)}^\alpha(V_2)$
16	$B[P] \rightarrow (V_1 V_2)$, $V_1 \rightarrow (P_1 P_2)$, $V_2 \rightarrow (P_3 P_4)$	$\epsilon_{\alpha\beta\gamma\delta} L_{(1)}^\alpha(B) L_{(1)}^\beta(V_1) L_{(1)}^\gamma(V_2) p_B^\delta$
17	$B[D] \rightarrow (V_1 V_2)$, $V_1 \rightarrow (P_1 P_2)$, $V_2 \rightarrow (P_3 P_4)$	$L_{(2)\alpha\beta}(B) L_{(1)}^\alpha(V_1) L_{(1)}^\beta(V_2)$
18	$B \rightarrow (T S)$, $T \rightarrow (P_1 P_2)$, $S \rightarrow (P_3 P_4)$	$L_{(2)\alpha\beta}(B) L_{(2)}^{\alpha\beta}(T)$
19	$B \rightarrow (V T)$, $T \rightarrow (P_1 P_2)$, $V \rightarrow (P_3 P_4)$	$L_{(1)\alpha}(B) L_{(2)}^{\alpha\beta}(T) L_{(1)\beta}(V)$
20	$B[D] \rightarrow (TV)$, $T \rightarrow (P_1 P_2)$, $V \rightarrow (P_3 P_4)$	$\epsilon_{\alpha\beta\delta\gamma} L_2^{\alpha\mu}(B) L_{2\mu}^\beta L_{(1)}^\gamma(V) p_B^\delta$
21	$B \rightarrow (T_1 T_2)$, $T_1 \rightarrow (P_1 P_2)$, $T_2 \rightarrow (P_3 P_4)$	$L_{(2)\alpha\beta}(T_1) L_{(2)}^{\alpha\beta}(T_2)$
22	$B[P] \rightarrow (T_1 T_2)$, $T_1 \rightarrow (P_1 P_2)$, $T_2 \rightarrow (P_3 P_4)$	$\epsilon_{\alpha\beta\gamma\delta} L_{(1)}^\alpha(B) L_{(2)}^{\beta\mu}(T_1) L_{(2)\mu}^\gamma(T_2) p_B^\delta$
23	$B[D] \rightarrow (T_1 T_2)$, $T_1 \rightarrow (P_1 P_2)$, $T_2 \rightarrow (P_3 P_4)$	$L_{(2)\alpha\beta}(B) L_{(2)}^{\alpha\gamma}(T_1) L_{(2)\gamma}^\beta(T_2)$

1230 J Considered Decay Chains

1231 The various decay channels considered in the model building are listed in Table J.1.

Table J.1: Decays considered in the LASSO model building.

Decay channel
$B_s \rightarrow D_s^- [K_1(1270)^+ [S, D] \rightarrow \pi^+ K^*(892)^0]$
$B_s \rightarrow D_s^- [K_1(1270)^+ \rightarrow \pi^+ K^*(1430)^0]$
$B_s \rightarrow D_s^- [K_1(1270)^+ [S, D] \rightarrow K^+ \rho(770)^0]$
$B_s \rightarrow D_s^- [K_1(1270)^+ [S, D] \rightarrow K^+ \omega(782)]$
$B_s \rightarrow D_s^- [K_1(1400)^+ [S, D] \rightarrow \pi^+ K^*(892)^0]$
$B_s \rightarrow D_s^- [K_1(1400)^+ [S, D] \rightarrow K^+ \rho(770)^0]$
$B_s \rightarrow D_s^- [K(1460)^+ \rightarrow \pi^+ \kappa]$
$B_s \rightarrow D_s^- [K(1460)^+ \rightarrow K^+ \sigma]$
$B_s \rightarrow D_s^- [K(1460)^+ \rightarrow \pi^+ K^*(892)^0]$
$B_s \rightarrow D_s^- [K(1460)^+ \rightarrow K^+ \rho(770)^0]$
$B_s \rightarrow D_s^- [K^*(1410)^+ \rightarrow \pi^+ K^*(892)^0]$
$B_s \rightarrow D_s^- [K^*(1410)^+ \rightarrow K^+ \rho(770)^0]$
$B_s \rightarrow D_s^- [K_2^*(1430)^+ \rightarrow \pi^+ K^*(892)^0]$
$B_s \rightarrow D_s^- [K_2^*(1430)^+ \rightarrow K^+ \rho(770)^0]$
$B_s \rightarrow D_s^- [K^*(1680)^+ \rightarrow \pi^+ K^*(892)^0]$
$B_s \rightarrow D_s^- [K^*(1680)^+ \rightarrow K^+ \rho(770)^0]$
$B_s \rightarrow D_s^- [K_2(1770)^+ \rightarrow \pi^+ K^*(892)^0]$
$B_s \rightarrow D_s^- [K_2(1770)^+ \rightarrow K^+ \rho(770)^0]$
$B_s \rightarrow \sigma^0(D_s^- K^+)_S$
$B_s [S, P, D] \rightarrow \sigma^0(D_s^- K^+)_V$
$B_s \rightarrow \rho(770)^0(D_s^- K^+)_S$
$B_s [S, P, D] \rightarrow \rho(770)^0(D_s^- K^+)_V$
$B_s \rightarrow K^*(892)^0(D_s^- \pi^+)_S$
$B_s [S, P, D] \rightarrow K^*(892)^0(D_s^- \pi^+)_V$
$B_s \rightarrow (D_s^- K^+)_S (\pi^+ \pi^-)_S$

1232 K Additional information for the time-dependent 1233 amplitude fit

1234 Table K.1 summarizes the fixed parameters for the resonances included in the baseline
 1235 model. The parameters of the resonances $K_1^+(1400)$ and $K^{*+}(1410)$ are determined in
 1236 the fit and their PDG values are only shown for comparison. Interference fractions are
 1237 listed in Tables K.2 and K.3.

1238 Figure K.1 shows the distribution of likelihood values for 150 time-dependent amplitude
 1239 fits with randomized starting parameters. The majority of the fits (76%) converge to the
 1240 global minimum. Two well isolated local minima are detected at $\Delta(2NLL) = 13$ (3.3σ)
 1241 and $\Delta(2NLL) = 23$ (4.8σ) to which 5% and 11% of the fits converge, respectively. The
 1242 fits at $\Delta(2NLL) = 11$, $\Delta(2NLL) = 18$ and $\Delta(2NLL) = 33$ did not converge properly
 1243 to one of the nearby local minima. The remaining fits (5%) have $\Delta(2NLL) > 500$ and
 1244 are not shown. This procedure has been repeatedly performed during the development of
 1245 the analysis, for both LASSO stages and the final fit, to ensure we operate at the global
 1246 minimum.

Table K.1: Parameters of the resonances chosen at the model selection stage.

Resonance	m [MeV]	Γ [MeV]	Source
$\rho(770)$	775.26 ± 0.25	149.1 ± 0.8	[15]
$K^{*0}(892)$	895.55 ± 0.20	47.3 ± 0.5	[15]
$K_1^+(1270)$	1289.81 ± 1.75	116.11 ± 3.4	[23]
$K^+(1460)$	1482.4 ± 15.64	335.6 ± 10.64	[23]
$K_1^+(1400)$	1403 ± 7	174 ± 13	[15]
$K^{*+}(1410)$	1421 ± 9	236 ± 18	[15]
$K^{0*}(1430)$	1425 ± 50	270 ± 80	[15]

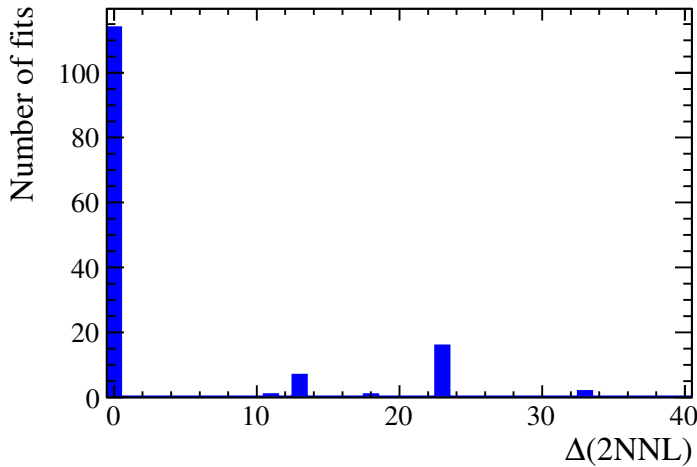


Figure K.1: Likelihood differences with respect to the smallest value obtained from 150 fits with randomized starting parameters.

Table K.2: Interference fractions of the amplitudes contributing to $b \rightarrow c$ decays.

Decay Channel i	Decay Channel j	$I_{ij}[\%]$
$B_s \rightarrow D_s (K_1(1400) \rightarrow K^*(892) \pi)$	$B_s \rightarrow (D_s \pi)_P K^*(892)$	-10.1 ± 4.2
$B_s \rightarrow D_s (K_1(1270) \rightarrow K^*(892) \pi)$	$B_s \rightarrow D_s (K_1(1400) \rightarrow K^*(892) \pi)$	8.8 ± 4.1
$B_s \rightarrow D_s (K_1(1270) \rightarrow K^*(892) \pi)$	$B_s \rightarrow (D_s \pi)_P K^*(892)$	-5.6 ± 1.3
$B_s \rightarrow D_s (K_1(1400) \rightarrow K^*(892) \pi)$	$B_s \rightarrow D_s (K_1(1270) \rightarrow K \rho(770))$	5.3 ± 0.5
$B_s \rightarrow D_s (K^*(1410) \rightarrow K^*(892) \pi)$	$B_s \rightarrow D_s (K^*(1410) \rightarrow K \rho(770))$	5.1 ± 0.3
$B_s \rightarrow D_s (K_1(1270) \rightarrow K_0^*(1430) \pi)$	$B_s \rightarrow D_s (K_1(1270) \rightarrow K \rho(770))$	-2.3 ± 0.8
$B_s \rightarrow (D_s \pi)_P K^*(892)$	$B_s \rightarrow D_s (K_1(1270) \rightarrow K \rho(770))$	0.5 ± 0.2
$B_s \rightarrow D_s (K_1(1270) \rightarrow K^*(892) \pi)$	$B_s \rightarrow D_s (K_1(1270) \rightarrow K \rho(770))$	-0.2 ± 0.4
$B_s \rightarrow D_s (K_1(1400) \rightarrow K^*(892) \pi)$	$B_s \rightarrow D_s (K_1(1270) \rightarrow K_0^*(1430) \pi)$	-0.1 ± 0.0
$B_s \rightarrow (D_s \pi)_P K^*(892)$	$B_s \rightarrow D_s (K_1(1270) \rightarrow K_0^*(1430) \pi)$	0.0 ± 0.0
$B_s \rightarrow D_s (K_1(1400) \rightarrow K^*(892) \pi)$	$B_s \rightarrow D_s (K^*(1410) \rightarrow K \rho(770))$	-0.0 ± 0.0
$B_s \rightarrow D_s (K_1(1400) \rightarrow K^*(892) \pi)$	$B_s \rightarrow D_s (K^*(1410) \rightarrow K^*(892) \pi)$	-0.0 ± 0.0
$B_s \rightarrow D_s (K^*(1410) \rightarrow K^*(892) \pi)$	$B_s \rightarrow D_s (K_1(1270) \rightarrow K \rho(770))$	0.0 ± 0.0
$B_s \rightarrow D_s (K^*(1410) \rightarrow K^*(892) \pi)$	$B_s \rightarrow D_s (K_1(1270) \rightarrow K_0^*(1430) \pi)$	-0.0 ± 0.0
$B_s \rightarrow D_s (K^*(1410) \rightarrow K \rho(770))$	$B_s \rightarrow D_s (K_1(1270) \rightarrow K \rho(770))$	-0.0 ± 0.0
$B_s \rightarrow D_s (K_1(1270) \rightarrow K^*(892) \pi)$	$B_s \rightarrow D_s (K_1(1270) \rightarrow K_0^*(1430) \pi)$	-0.0 ± 0.0
$B_s \rightarrow D_s (K^*(1410) \rightarrow K^*(892) \pi)$	$B_s \rightarrow (D_s \pi)_P K^*(892)$	-0.0 ± 0.0
$B_s \rightarrow (D_s \pi)_P K^*(892)$	$B_s \rightarrow D_s (K^*(1410) \rightarrow K \rho(770))$	0.0 ± 0.0
$B_s \rightarrow D_s (K^*(1410) \rightarrow K \rho(770))$	$B_s \rightarrow D_s (K_1(1270) \rightarrow K_0^*(1430) \pi)$	-0.0 ± 0.0
$B_s \rightarrow D_s (K_1(1270) \rightarrow K^*(892) \pi)$	$B_s \rightarrow D_s (K^*(1410) \rightarrow K^*(892) \pi)$	-0.0 ± 0.0
$B_s \rightarrow D_s (K_1(1270) \rightarrow K^*(892) \pi)$	$B_s \rightarrow D_s (K^*(1410) \rightarrow K \rho(770))$	0.0 ± 0.0

Table K.3: Interference fractions of the amplitudes contributing to $b \rightarrow u$ decays.

Decay Channel i	Decay Channel j	$I_{ij}[\%]$
$B_s \rightarrow D_s (K_1(1270) \rightarrow K^*(892) \pi)$	$B_s \rightarrow (D_s \pi)_P K^*(892)$	-20.7 ± 4.9
$B_s \rightarrow D_s (K_1(1270) \rightarrow K^*(892) \pi)$	$B_s \rightarrow D_s (K_1(1400) \rightarrow K^*(892) \pi)$	-20.0 ± 8.7
$B_s \rightarrow D_s (K_1(1400) \rightarrow K^*(892) \pi)$	$B_s \rightarrow (D_s \pi)_P K^*(892)$	18.9 ± 9.7
$B_s \rightarrow D_s (K(1460) \rightarrow K^*(892) \pi)$	$B_s \rightarrow (D_s \pi)_P K^*(892)$	-8.4 ± 1.2
$B_s \rightarrow (D_s K)_P \rho(770)$	$B_s \rightarrow D_s (K_1(1270) \rightarrow K_0^*(1430) \pi)$	-6.3 ± 1.2
$B_s \rightarrow D_s (K_1(1270) \rightarrow K_0^*(1430) \pi)$	$B_s \rightarrow D_s (K_1(1270) \rightarrow K \rho(770))$	-5.5 ± 1.7
$B_s \rightarrow (D_s \pi)_P K^*(892)$	$B_s \rightarrow (D_s K)_P \rho(770)$	3.1 ± 0.6
$B_s \rightarrow D_s (K_1(1400) \rightarrow K^*(892) \pi)$	$B_s \rightarrow (D_s K)_P \rho(770)$	2.0 ± 0.6
$B_s \rightarrow D_s (K_1(1400) \rightarrow K^*(892) \pi)$	$B_s \rightarrow D_s (K_1(1270) \rightarrow K \rho(770))$	2.0 ± 1.3
$B_s \rightarrow (D_s \pi)_P K^*(892)$	$B_s \rightarrow D_s (K_1(1270) \rightarrow K \rho(770))$	1.7 ± 0.8
$B_s \rightarrow D_s (K(1460) \rightarrow K^*(892) \pi)$	$B_s \rightarrow (D_s K)_P \rho(770)$	-1.5 ± 0.3
$B_s \rightarrow D_s (K_1(1270) \rightarrow K^*(892) \pi)$	$B_s \rightarrow (D_s K)_P \rho(770)$	-1.3 ± 0.4
$B_s \rightarrow D_s (K_1(1270) \rightarrow K^*(892) \pi)$	$B_s \rightarrow D_s (K_1(1270) \rightarrow K \rho(770))$	-0.6 ± 1.0
$B_s \rightarrow (D_s \pi)_P K^*(892)$	$B_s \rightarrow D_s (K_1(1270) \rightarrow K_0^*(1430) \pi)$	0.1 ± 0.0
$B_s \rightarrow (D_s K)_P \rho(770)$	$B_s \rightarrow D_s (K_1(1270) \rightarrow K \rho(770))$	-0.1 ± 2.9
$B_s \rightarrow D_s (K(1460) \rightarrow K^*(892) \pi)$	$B_s \rightarrow D_s (K_1(1270) \rightarrow K \rho(770))$	0.1 ± 0.0
$B_s \rightarrow D_s (K_1(1270) \rightarrow K^*(892) \pi)$	$B_s \rightarrow D_s (K(1460) \rightarrow K^*(892) \pi)$	0.0 ± 0.0
$B_s \rightarrow D_s (K_1(1400) \rightarrow K^*(892) \pi)$	$B_s \rightarrow D_s (K(1460) \rightarrow K^*(892) \pi)$	-0.0 ± 0.0
$B_s \rightarrow D_s (K_1(1270) \rightarrow K^*(892) \pi)$	$B_s \rightarrow D_s (K_1(1270) \rightarrow K_0^*(1430) \pi)$	-0.0 ± 0.0
$B_s \rightarrow D_s (K_1(1400) \rightarrow K^*(892) \pi)$	$B_s \rightarrow D_s (K_1(1270) \rightarrow K_0^*(1430) \pi)$	0.0 ± 0.0
$B_s \rightarrow D_s (K(1460) \rightarrow K^*(892) \pi)$	$B_s \rightarrow D_s (K_1(1270) \rightarrow K_0^*(1430) \pi)$	0.0 ± 0.0

L Data-simulation comparisson

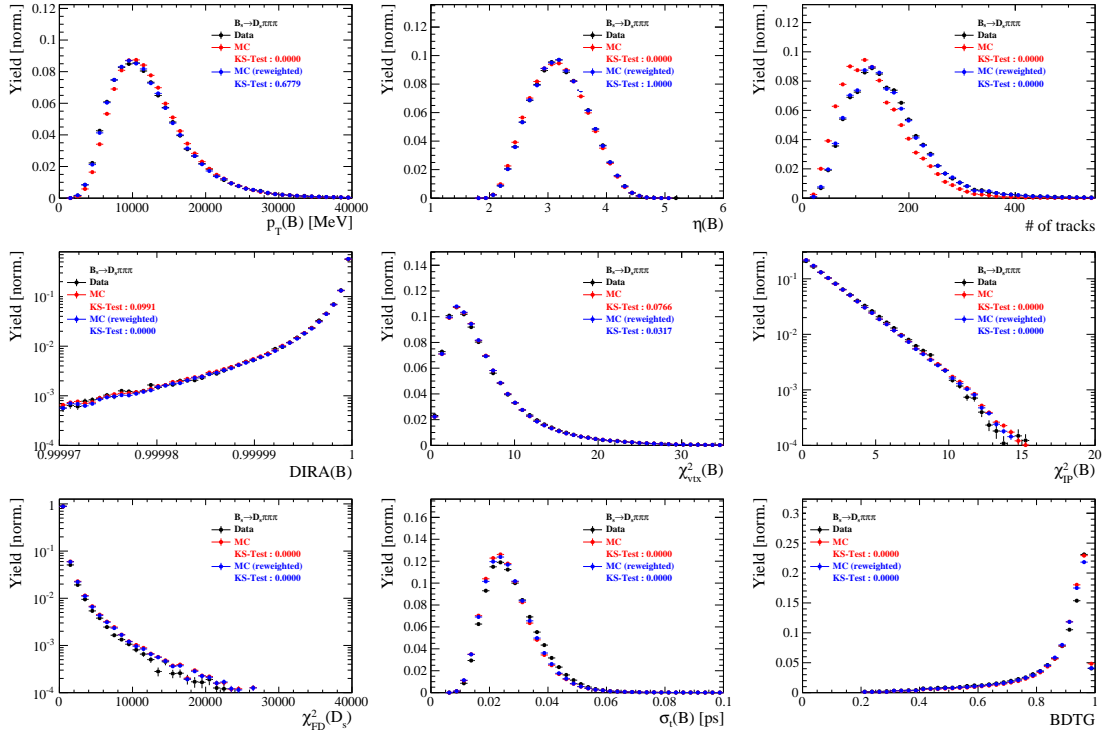


Figure L.1: Comparison between data and MC of selected variables for $B_s \rightarrow D_s \pi\pi\pi$ decays.

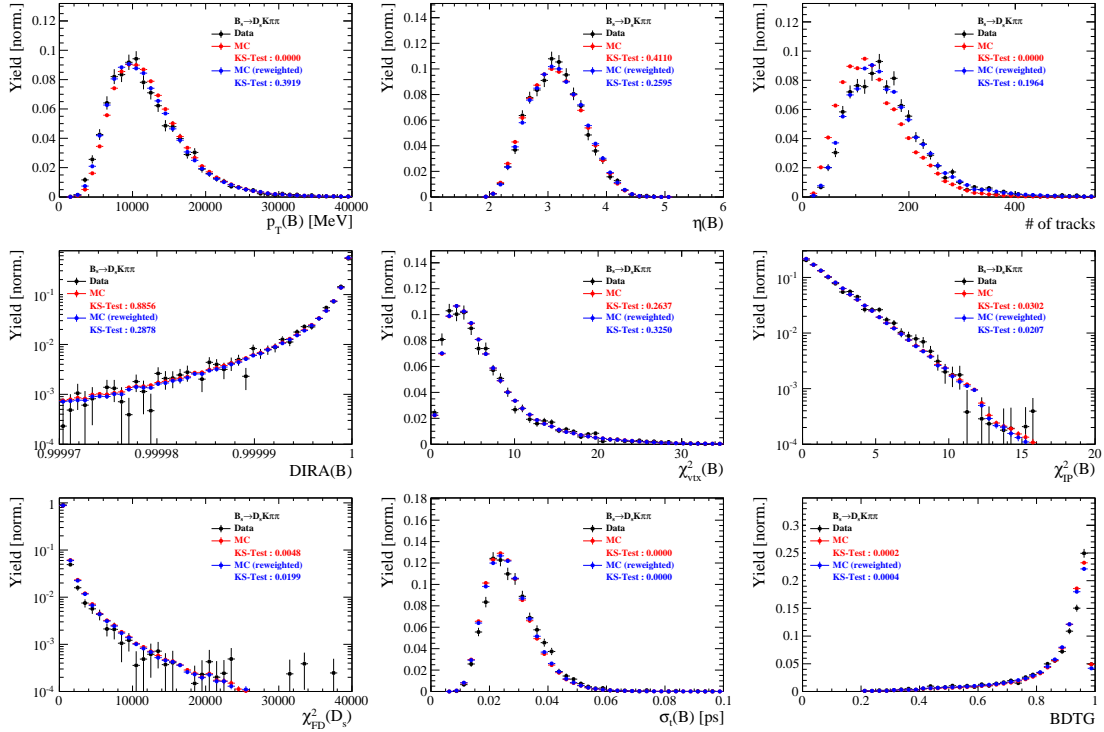


Figure L.2: Comparison between data and MC of selected variables for $B_s \rightarrow D_s K\pi\pi$ decays.

1248 M Data distributions

1249 Comparison of signal and calibration channels

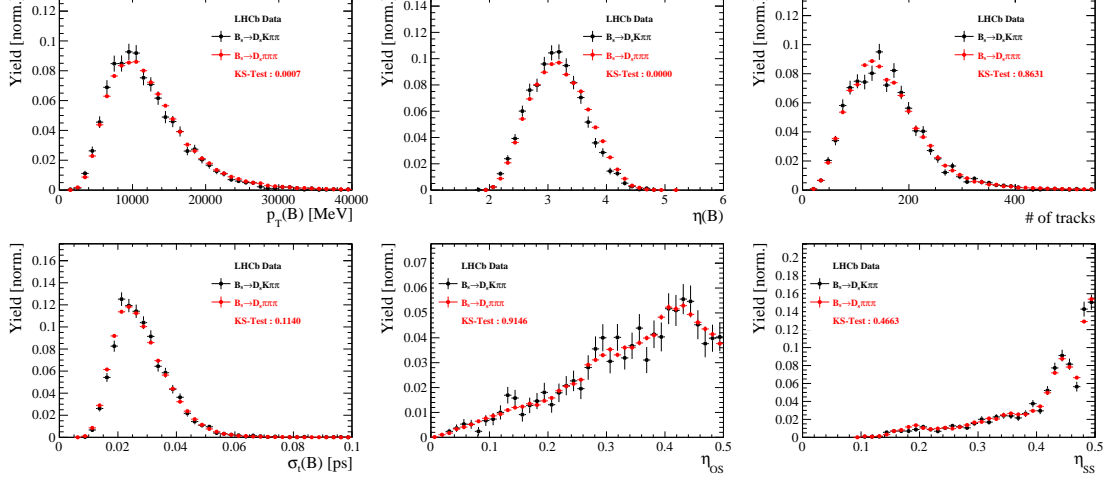


Figure M.1: Comparison between $B_s \rightarrow D_s K\pi\pi$ and $B_s \rightarrow D_s \pi\pi\pi$ decays for selected variables.

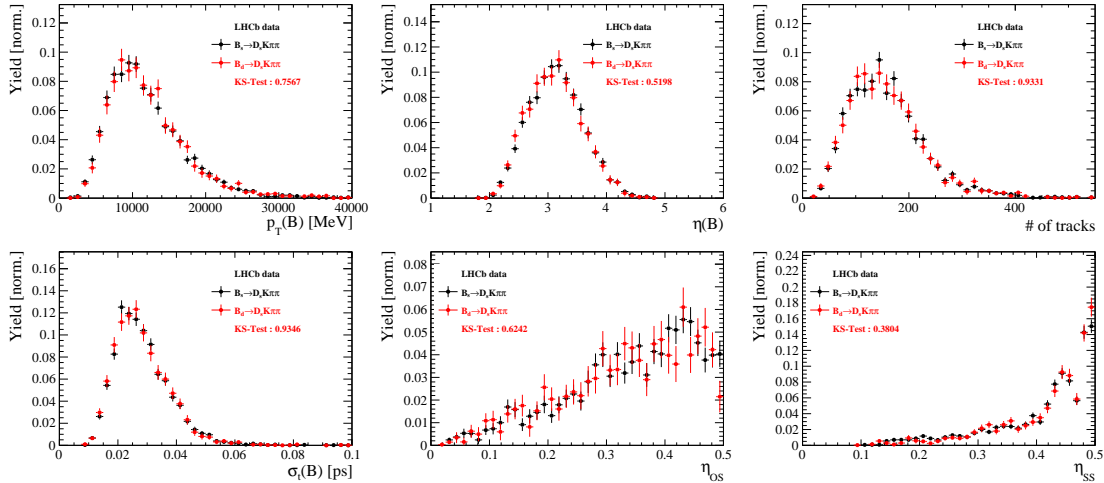


Figure M.2: Comparison between $B_s \rightarrow D_s K\pi\pi$ and $B_d \rightarrow D_s K\pi\pi$ decays for selected variables.

1250 Comparison of data taken in 2016 and 2017

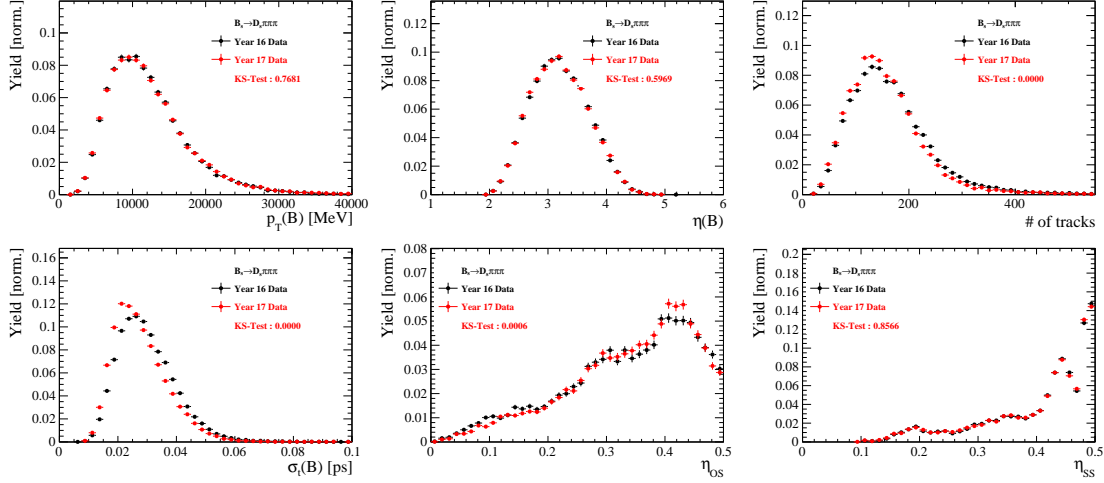


Figure M.3: Comparison of selected variables for $B_s \rightarrow D_s \pi\pi\pi$ data taken in 2016 and 2017.

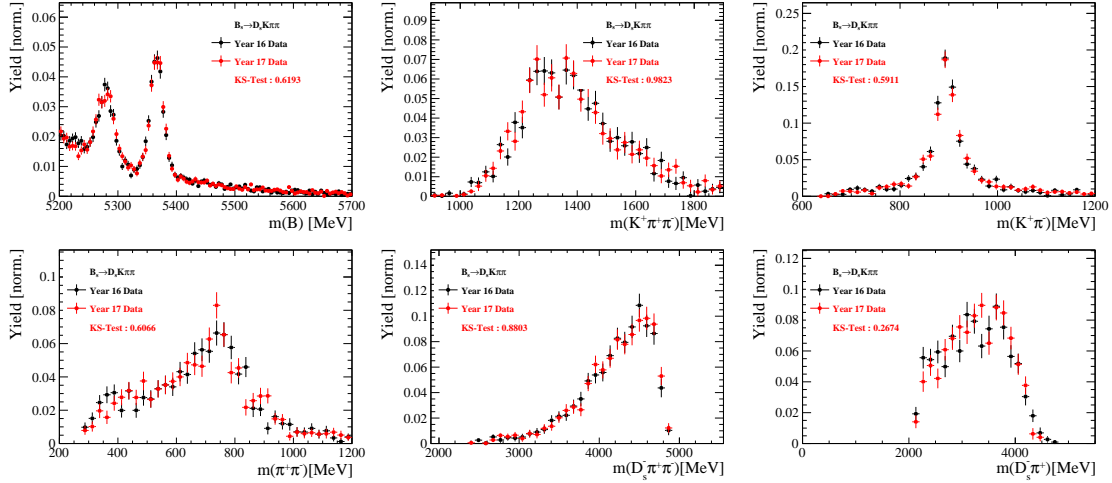


Figure M.4: Comparison of selected variables for $B_s \rightarrow D_s K\pi\pi$ data taken in 2016 and 2017.

1251 Comparison of Run-I and Run-II data

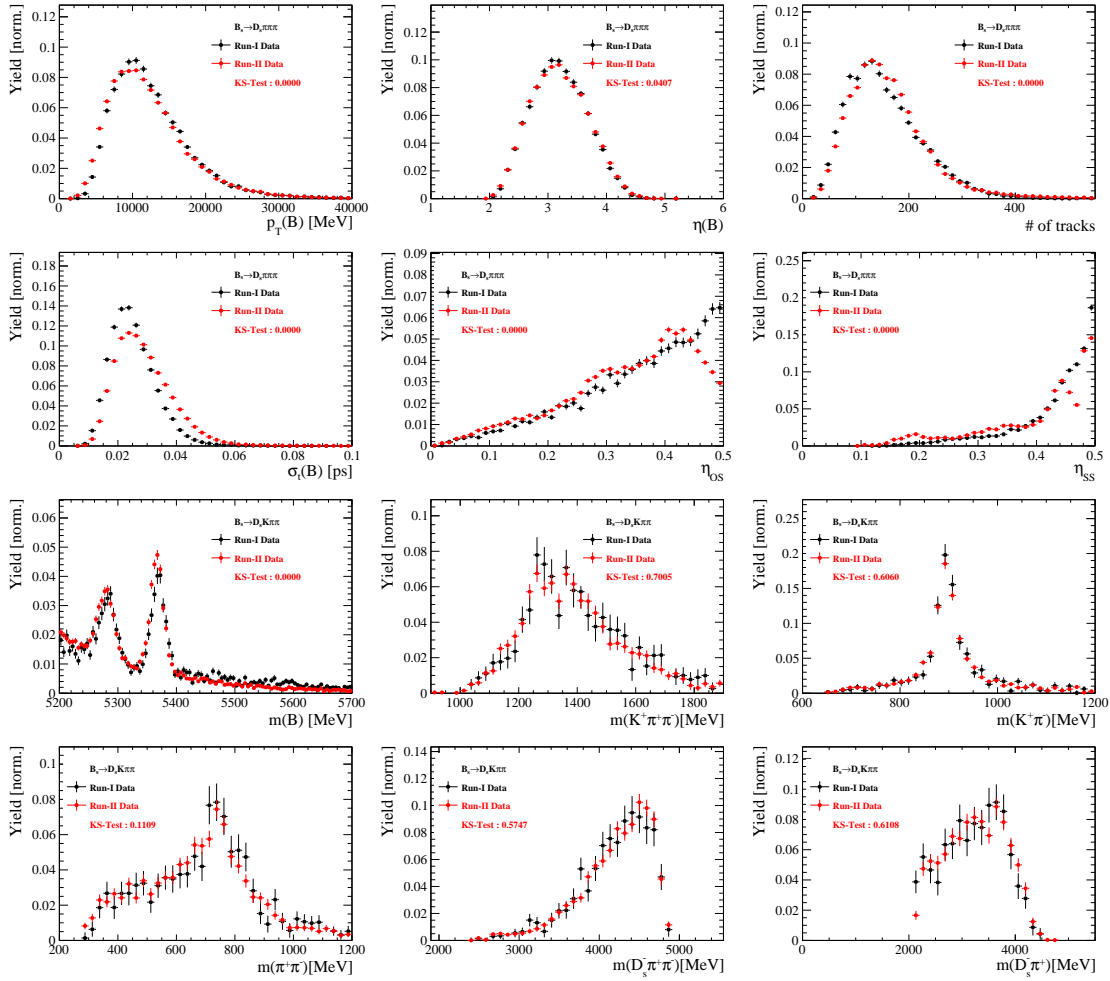


Figure M.5: Comparison of selected variables for Run-I and Run-II data.

1252 Comparison of D_s final states

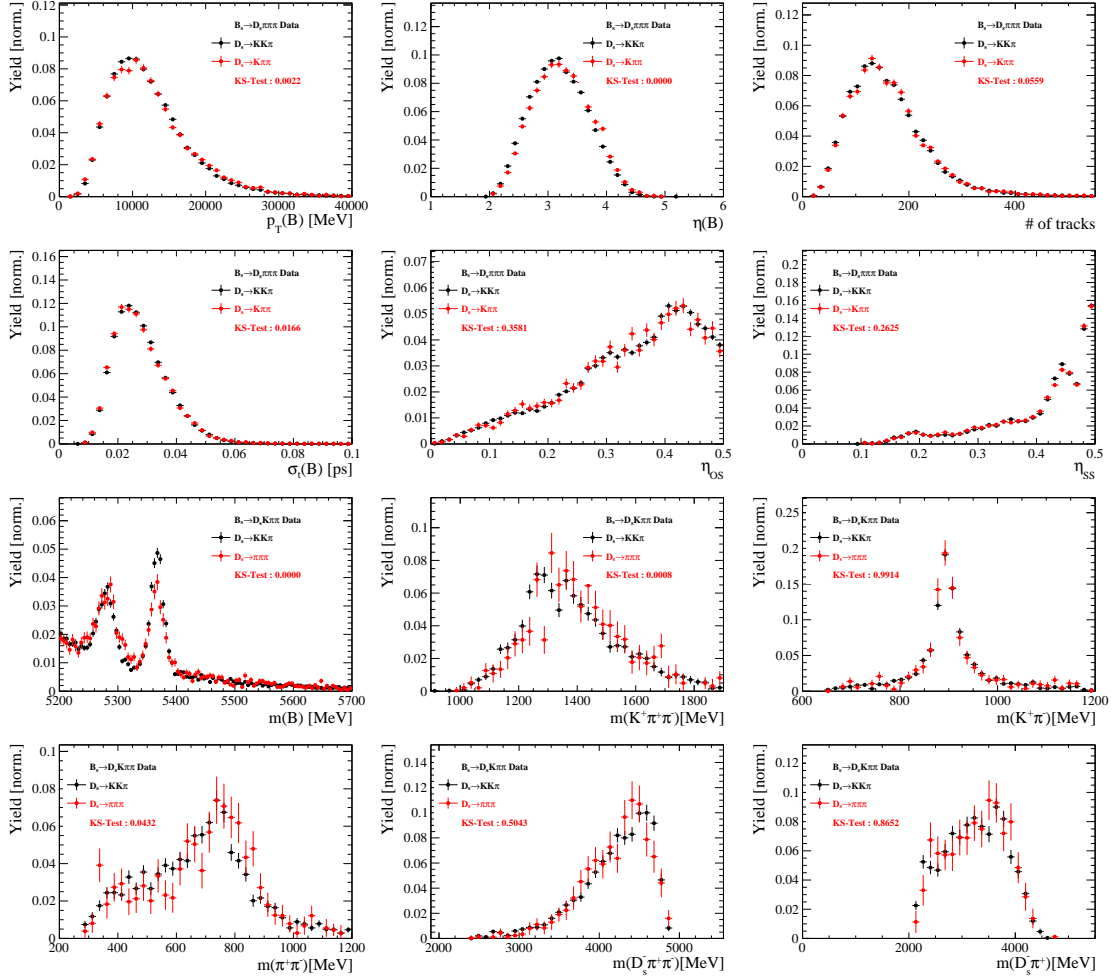


Figure M.6: Comparison of selected variables for different D_s final states.

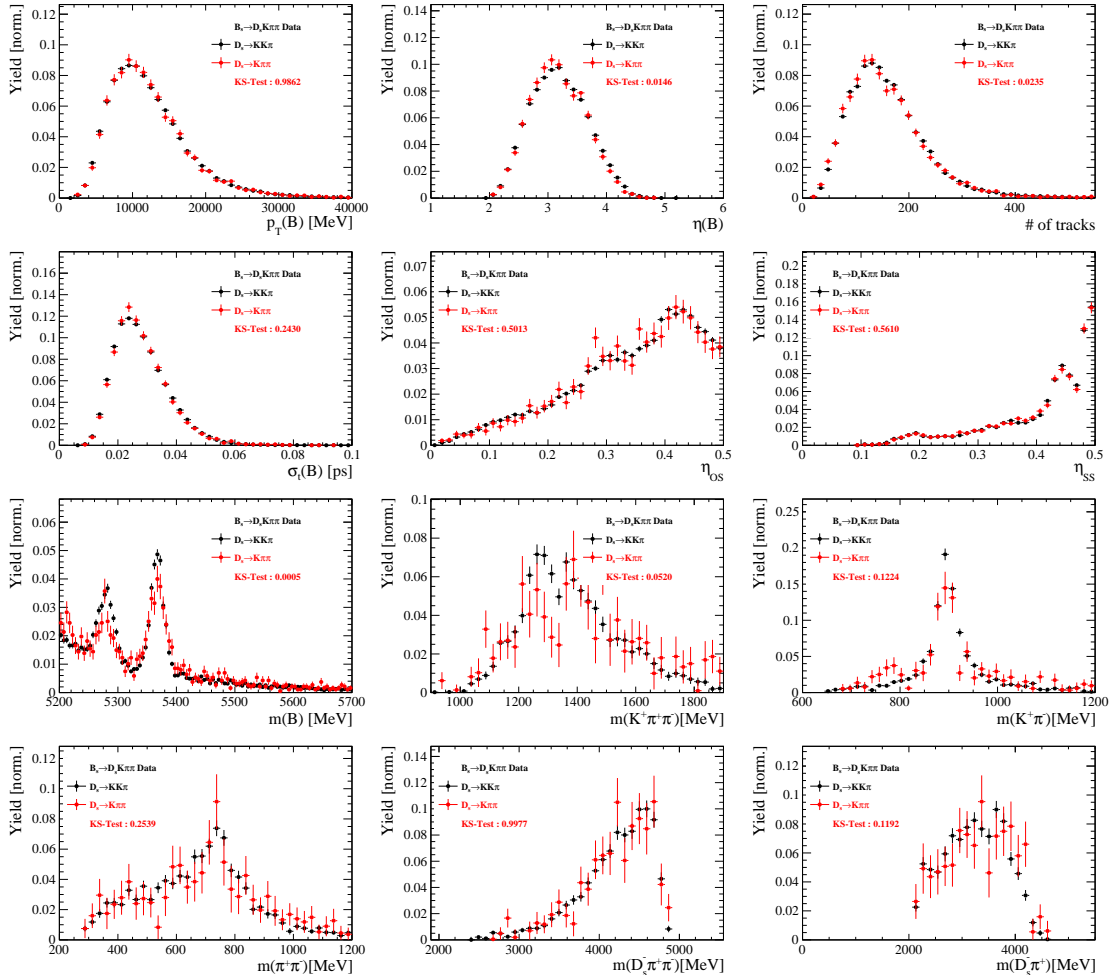


Figure M.7: Comparison of selected variables for different D_s final states.

1253 Comparison of trigger categories

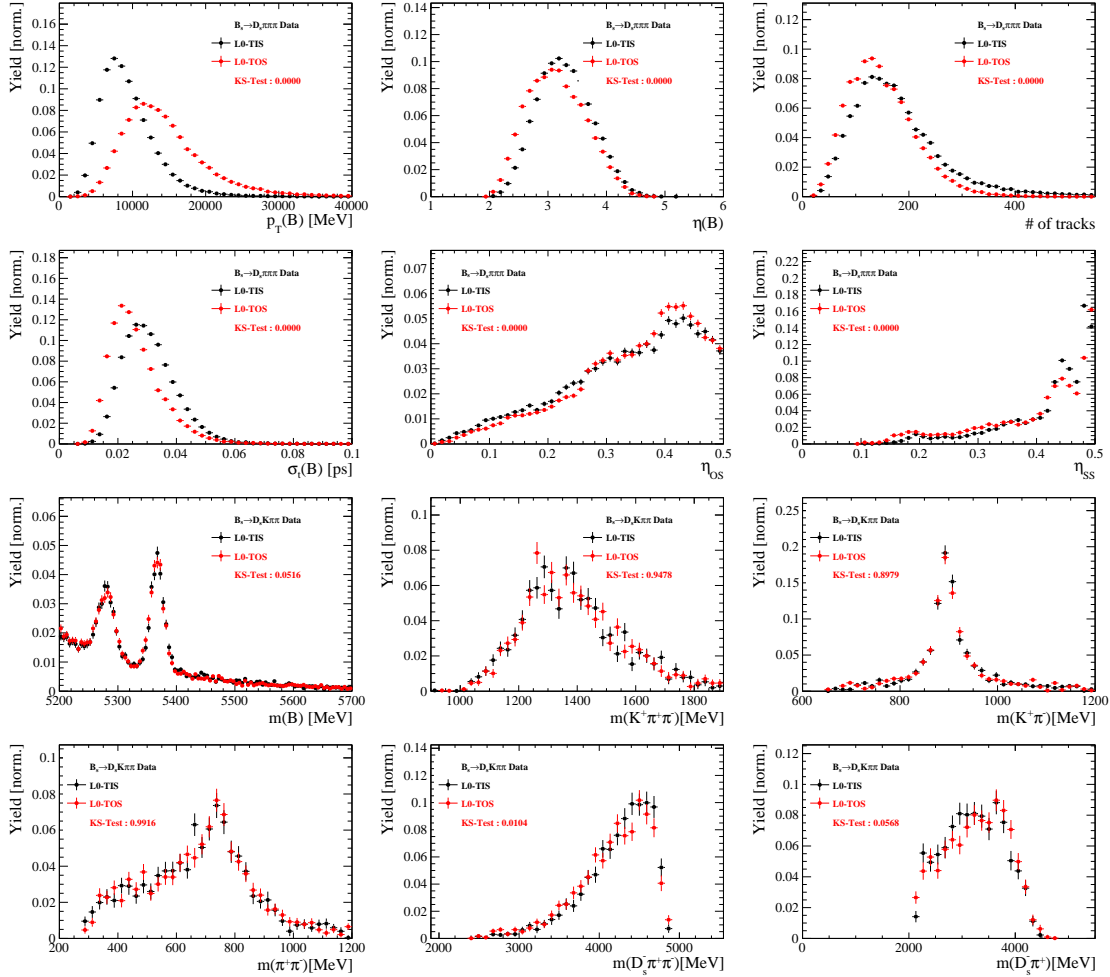


Figure M.8: Comparison of selected variables for different trigger categories.

1254 **References**

- 1255 [1] S. Blusk, *First observations and measurements of the branching fractions for the*
1256 *decays $\bar{B}_s^0 \rightarrow D_s^+ K^- \pi^+ \pi^-$ and $\bar{B}^0 \rightarrow D_s^+ K^- \pi^+ \pi^-$* , LHCb-ANA-2012-076.
- 1257 [2] LHCb, S. Blusk, *Measurement of the CP observables in $\bar{B}_s^0 \rightarrow D_s^+ K^-$ and first obser-*
1258 *vation of $\bar{B}_{(s)}^0 \rightarrow D_s^+ K^- \pi^+ \pi^-$ and $\bar{B}_s^0 \rightarrow D_{s1}(2536)^+ \pi^-$* , 2012. [arXiv:1212.4180](#).
- 1259 [3] LHCb collaboration, R. Aaij *et al.*, *First observation of the decays $\bar{B}_{(s)}^0 \rightarrow D_s^+ K^- \pi^+ \pi^-$*
1260 *and $\bar{B}_s^0 \rightarrow D_{s1}(2536)^+ \pi^-$* , Phys. Rev. **D86** (2012) 112005, [arXiv:1211.1541](#).
- 1261 [4] R. Fleischer, *New strategies to obtain insights into CP violation through $B_s \rightarrow$*
1262 *$D_s^\pm K^\mp, D_s^{*\pm} K^\mp, \dots$ and $B_d \rightarrow D^\pm \pi^\mp, D^{*\pm} \pi^\mp, \dots$ decays*, Nucl. Phys. **B671** (2003) 459,
1263 [arXiv:hep-ph/0304027](#).
- 1264 [5] K. De Bruyn *et al.*, *Exploring $B_s \rightarrow D_s^{(*)\pm} K^\mp$ Decays in the Presence of a Sizable*
1265 *Width Difference $\Delta\Gamma_s$* , Nucl. Phys. **B868** (2013) 351, [arXiv:1208.6463](#).
- 1266 [6] L. collaboration, *Measurement of time-dependent CP-violation observables in $B_s^0 \rightarrow$*
1267 *$D_s^\mp K^\pm$* , LHCb-ANA-2016-052.
- 1268 [7] LHCb, R. Aaij *et al.*, *Measurement of CP asymmetry in $B_s^0 \rightarrow D_s^\mp K^\pm$ decays*, JHEP
1269 **03** (2018) 059, [arXiv:1712.07428](#).
- 1270 [8] E. Byckling and K. Kajantie, *Particle Kinematics*, John Wiley & Sons, 1973.
- 1271 [9] S. Mandelstam, J. E. Paton, R. F. Peierls, and A. Q. Sarker, *Isobar approximation*
1272 *of production processes*, Annals of Physics **18** (1962), no. 2 198 .
- 1273 [10] D. J. Herndon, P. Söding, and R. J. Cashmore, *Generalized isobar model formalism*,
1274 Phys. Rev. D **11** (1975) 3165.
- 1275 [11] J. J. Brehm, *Unitarity and the isobar model: Two-body discontinuities*, Annals of
1276 Physics **108** (1977), no. 2 454 .
- 1277 [12] P. d'Argent *et al.*, *Amplitude Analyses of $D^0 \rightarrow \pi^+ \pi^- \pi^+ \pi^-$ and $D^0 \rightarrow K^+ K^- \pi^+ \pi^-$*
1278 *Decays*, JHEP **05** (2017) 143, [arXiv:1703.08505](#).
- 1279 [13] F. von Hippel and C. Quigg, *Centrifugal-barrier effects in resonance partial decay*
1280 *widths, shapes, and production amplitudes*, Phys. Rev. D **5** (1972) 624.
- 1281 [14] J. D. Jackson, *Remarks on the phenomenological analysis of resonances*, Il Nuovo
1282 Cimento Series 10 **34** (1964), no. 6 1644.
- 1283 [15] Particle Data Group, C. Patrignani *et al.*, *Review of Particle Physics*, Chin. Phys.
1284 **C40** (2016), no. 10 100001.
- 1285 [16] C. Zemach, *Use of angular momentum tensors*, Phys. Rev. **140** (1965) B97.
- 1286 [17] W. Rarita and J. Schwinger, *On a theory of particles with half integral spin*, Phys.
1287 Rev. **60** (1941) 61.

- 1288 [18] S. U. Chung, *General formulation of covariant helicity-coupling amplitudes*, Phys.
 1289 Rev. D **57** (1998) 431.
- 1290 [19] B. S. Zou and D. V. Bugg, *Covariant tensor formalism for partial wave analyses of*
 1291 ψ *decay to mesons*, Eur. Phys. J. **A16** (2003) 537, arXiv:hep-ph/0211457.
- 1292 [20] V. Filippini, A. Fontana, and A. Rotondi, *Covariant spin tensors in meson spec-*
 1293 *troscopy*, Phys. Rev. **D51** (1995) 2247.
- 1294 [21] J.-J. Zhu, *Explicit expressions of spin wave functions*, arXiv:hep-ph/9906250.
- 1295 [22] M. Williams, *Numerical Object Oriented Quantum Field Theory Calculations*, Comput.
 1296 Phys. Commun. **180** (2009) 1847, arXiv:0805.2956.
- 1297 [23] LHCb, R. Aaij *et al.*, *Studies of the resonance structure in $D^0 \rightarrow K^\mp\pi^\pm\pi^\pm\pi^\mp$ decays*,
 1298 Eur. Phys. J. **C78** (2018), no. 6 443, arXiv:1712.08609.
- 1299 [24] D. J. Lange, *The EvtGen particle decay simulation package*, Nucl. Instrum. Meth.
 1300 **A462** (2001) 152.
- 1301 [25] M. Karbach and M. Kenzie, *Gammacombo package*,
 1302 http://gammacombo.hepforge.org/web/HTML/index.html, 2014.
- 1303 [26] A. Hoecker *et al.*, *TMVA: Toolkit for Multivariate Data Analysis*, PoS **ACAT** (2007)
 1304 040, arXiv:physics/0703039.
- 1305 [27] N. L. Johnson, *Systems of frequency curves generated by methods of translation*,
 1306 Biometrika **36** (1949), no. 1/2 149.
- 1307 [28] Particle Data Group, K. A. Olive *et al.*, *Review of Particle Physics*, Chin. Phys. **C38**
 1308 (2014) 090001.
- 1309 [29] LHCb collaboration, R. Aaij *et al.*, *LHCb detector performance*, Int. J. Mod. Phys.
 1310 **A30** (2015) 1530022, arXiv:1412.6352.
- 1311 [30] M. Schiller, *Proper time resolution studies in $B_s \rightarrow D_s\pi$* , Tech. Rep. LHCb-INT-
 1312 2011-005. CERN-LHCb-INT-2011-005, CERN, Geneva, Feb, 2011.
- 1313 [31] LHCb collaboration, L. Zhang, *Measurements of CP violation in $B_s^0 \rightarrow J/\psi K^+K^-$*
 1314 *decays in the low K^+K^- mass range with 13 TeV data*, LHCb-ANA-2017-028.
- 1315 [32] LHCb, R. Aaij *et al.*, *Updated measurement of time-dependent CP-violating ob-*
 1316 *servables in $B_s^0 \rightarrow J/\psi K^+K^-$ decays*, Eur. Phys. J. **C79** (2019), no. 8 706,
 1317 arXiv:1906.08356.
- 1318 [33] LHCb collaboration, *Precision measurement of the $B_s - \bar{B}_s$ oscillation frequency with*
 1319 *the decay $B_s \rightarrow D_s\pi$* , LHCb-ANA-2019-XXX.
- 1320 [34] A. Poluektov, *Correction of simulated particle identification response in LHCb using*
 1321 *kernel density estimation*, LHCb-INT-2017-007.

- 1322 [35] Heavy Flavor Averaging Group, Y. Amhis *et al.*, *Averages of b-hadron, c-hadron, and*
 1323 *τ -lepton properties as of summer 2014*, arXiv:1412.7515, updated results and plots
 1324 available at <http://www.slac.stanford.edu/xorg/hfag/>.
- 1325 [36] T. M. Karbach, G. Raven, and M. Schiller, *Decay time integrals in neutral meson*
 1326 *mixing and their efficient evaluation*, arXiv:1407.0748.
- 1327 [37] LHCb collaboration, R. Aaij *et al.*, *Opposite-side flavour tagging of B mesons at the*
 1328 *LHCb experiment*, Eur. Phys. J. **C72** (2012) 2022, arXiv:1202.4979.
- 1329 [38] LHCb, R. Aaij *et al.*, *A new algorithm for identifying the flavour of B_s^0 mesons at*
 1330 *LHCb*, JINST **11** (2016), no. 05 P05010, arXiv:1602.07252.
- 1331 [39] LHCb, R. Aaij *et al.*, *Measurement of B^0 , B_s^0 , B^+ and Λ_b^0 production asymmetries in 7*
 1332 *and 8 TeV proton-proton collisions*, Phys. Lett. **B774** (2017) 139, arXiv:1703.08464.
- 1333 [40] H. Gordon, R. W. Lambert, J. van Tilburg, and M. Vesterinen, *A Measurement of*
 1334 *the $K\pi$ Detection Asymmetry*, Tech. Rep. LHCb-INT-2012-027. CERN-LHCb-INT-
 1335 2012-027, CERN, Geneva, Feb, 2013.
- 1336 [41] A. Davis *et al.*, *Measurement of the instrumental asymmetry for $K^- \pi^+$ -pairs at LHCb*
 1337 *in Run 2*, Tech. Rep. LHCb-PUB-2018-004. CERN-LHCb-PUB-2018-004, CERN,
 1338 Geneva, Mar, 2018.
- 1339 [42] I. I. Y. Bigi and H. Yamamoto, *Interference between Cabibbo allowed and doubly*
 1340 *forbidden transitions in $D \rightarrow K(S)$, $K(L) + \pi$'s decays*, Phys. Lett. **B349** (1995)
 1341 363, arXiv:hep-ph/9502238.
- 1342 [43] M. Pivk and F. R. Le Diberder, *sPlot: A statistical tool to unfold data distributions*,
 1343 Nucl. Instrum. Meth. **A555** (2005) 356, arXiv:physics/0402083.
- 1344 [44] R. Tibshirani, *Regression shrinkage and selection via the Lasso*, Journal of the Royal
 1345 Statistical Society, Series B **58** (1994) 267.
- 1346 [45] B. Guegan, J. Hardin, J. Stevens, and M. Williams, *Model selection for amplitude*
 1347 *analysis*, JINST **10** (2015), no. 09 P09002, arXiv:1505.05133.
- 1348 [46] G. Schwarz, *Estimating the dimension of a model*, Ann. Statist. **6** (1978) 461.
- 1349 [47] CLEO Collaboration, M. Artuso *et al.*, *Amplitude analysis of $D^0 \rightarrow K^+ K^- \pi^+ \pi^-$* ,
 1350 Phys. Rev. **D85** (2012) 122002, arXiv:1201.5716.
- 1351 [48] T. Skwarnicki, *A study of the radiative cascade transitions between the Upsilon-prime*
 1352 *and Upsilon resonances*, PhD thesis, Institute of Nuclear Physics, Krakow, 1986,
 1353 DESY-F31-86-02.
- 1354 [49] D. Hill, M. John, and P. Gandini, *A study of partially reconstructed $B^\pm \rightarrow D^{*0} h^\pm$*
 1355 *decays using the $D^0 \rightarrow K\pi, KK, \pi\pi$ final states*, LHCb-ANA-2017-018.
- 1356 [50] G. H. Golub and C. F. Van Loan, *Matrix Computations (3rd Ed.)*, Johns Hopkins
 1357 University Press, Baltimore, MD, USA, 1996.

- 1358 [51] L. collaboration, *Precision measurement of the B_s oscillation frequency with the decay*
 1359 $B_s \rightarrow D_s\pi$, LHCb-ANA-2012-053.
- 1360 [52] LHCb collaboration, R. Aaij *et al.*, *Precision measurement of the $B_s^0-\bar{B}_s^0$ oscillation frequency in the decay $B_s^0 \rightarrow D_s^-\pi^+$* , New J. Phys. **15** (2013) 053021,
 1361 arXiv:1304.4741.
- 1363 [53] BaBar, P. del Amo Sanchez *et al.*, *Measurement of $D0$ -anti $D0$ mixing parameters using $D0 \rightarrow K(S)0$ pi+ pi- and $D0 \rightarrow K(S)0$ $K+K-$ decays*, Phys. Rev. Lett. **105**
 1364 (2010) 081803, arXiv:1004.5053.
- 1366 [54] LHCb, R. Aaij *et al.*, *Studies of the resonance structure in $D^0 \rightarrow K_S^0 K^\pm \pi^\mp$ decays*,
 1367 Phys. Rev. **D93** (2016), no. 5 052018, arXiv:1509.06628.
- 1368 [55] D. V. Bugg, *The mass of the σ pole*, Journal of Physics G Nuclear Physics **34** (2007)
 1369 151, arXiv:hep-ph/0608081.
- 1370 [56] W. Dunwoodie. Fits to $K\pi$ $I = \frac{1}{2}$ S -wave amplitude and phase data.
- 1371 [57] D. Aston *et al.*, *A Study of $K^-\pi^+$ Scattering in the Reaction $K^-p \rightarrow K^-\pi^+n$ at*
 1372 $11\text{GeV}/c$, Nucl. Phys. **B296** (1988) 493.
- 1373 [58] BaBar, B. Aubert *et al.*, *Dalitz-plot analysis of the decays $B^\pm \rightarrow K^\pm \pi^\mp \pi^\pm$* ,
 1374 Phys. Rev. **D72** (2005) 072003, arXiv:hep-ex/0507004, [Erratum: Phys.
 1375 Rev.D74,099903(2006)].
- 1376 [59] G. J. Gounaris and J. J. Sakurai, *Finite-width corrections to the vector-meson-dominance prediction for $\rho \rightarrow e^+e^-$* , Phys. Rev. Lett. **21** (1968) 244.
- 1378 [60] CMD-2, R. R. Akhmetshin *et al.*, *Measurement of $e^+e^- \rightarrow \pi^+\pi^-$ cross-section with*
 1379 *CMD-2 around rho meson*, Phys. Lett. **B527** (2002) 161, arXiv:hep-ex/0112031.
- 1380 [61] M. S. et al. *Search for CP violation in the $D^0 \rightarrow KK\pi\pi$ decay through a full*
 1381 *amplitude analysis*, LHCb-ANA-2017-064.
- 1382 [62] LHCb Collaboration, R. Aaij, *Search for CP violation through an amplitude analysis*
 1383 *of $D^0 \rightarrow K^+K^-\pi^+\pi^-$ decays*, Tech. Rep. arXiv:1811.08304. LHCb-PAPER-2018-041,
 1384 CERN, Geneva, Nov, 2018. *Temporary entry*.
- 1385 [63] S. M. Flatté, *Coupled-channel analysis of the $\pi\eta$ and KK systems near KK threshold*,
 1386 Physics Letters B **63** (1976), no. 2 224 .
- 1387 [64] BES Collaboration, M. Ablikim *et al.*, *Resonances in $J/\psi \rightarrow \phi\pi^+\pi^-$ and ϕK^+K^-* ,
 1388 Phys. Lett. **B607** (2005) 243, arXiv:hep-ex/0411001.